Study and fabrication of a micro scanner for optical applications

Thèse présentée à la Faculté des Sciences
Institut de Microtechnique
Université de Neuchâtel
Pour l'obtention du grade de *Docteur ès Sciences*

par

Yves Pétremand

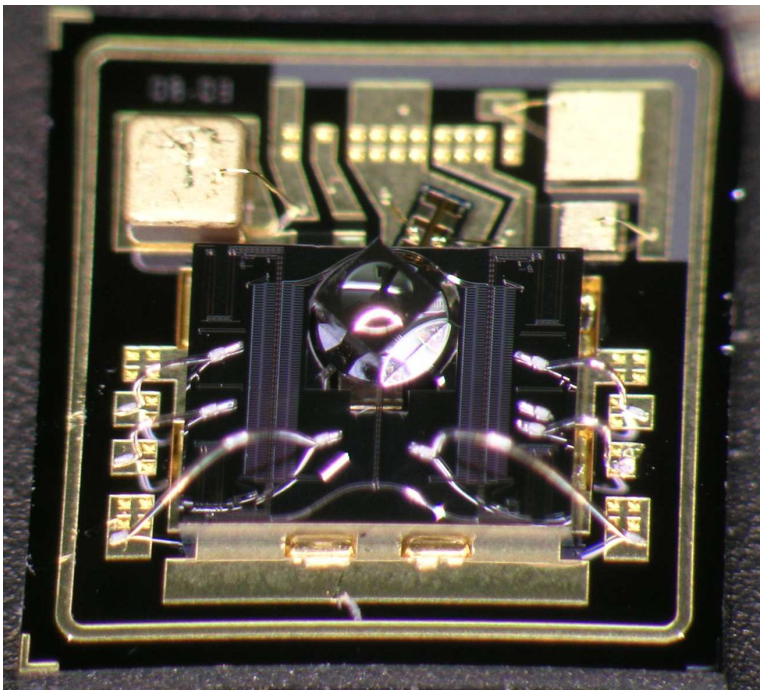

Acceptée sur proposition du jury:
Prof. N.F. de Rooij, directeur de thèse
Prof. H. Shea
Prof. H.P. Herzig
Dr. W. Noell
M. Epitaux

Soutenue le 13 mai 2008

Université de Neuchâtel

FACULTE DES SCIENCES
Secrétariat-Décanat de la faculté
- Rue Emile-Argand 11
- CP 158
- CH-2009 Neuchâtel

IMPRIMATUR POUR LA THESE

Study and fabrication of a micro scanner for optical applications

Yves PETREMAND

UNIVERSITE DE NEUCHATEL

FACULTE DES SCIENCES

La Faculté des sciences de l'Université de Neuchâtel,
sur le rapport des membres du jury

MM. N. de Rooij (directeur de thèse),
H.P. Herzig, W. Noell
H. Shea (EPF Lausanne) et
M. Epitaux (Aprius Inc, Sunnyvale CA)

autorise l'impression de la présente thèse.

Neuchâtel, le 19 août 2008

Le doyen :
F. Kessler

UNIVERSITE DE NEUCHATEL
FACULTE DES SCIENCES
Secrétariat - décanat de la faculté
Rue Emile-Argand 11 - CP 158
CH-2009 Neuchâtel
Félix Kessler

What are the possibilities of small but movable machines?
They may or may not be useful, but they surely would be fun to make.

Richard P. Feynman, Nobel Price winner in Physics 1965
in his talk "There's plenty of room at the bottom"

Abstract

Keywords: Optical scanner, Silicon, Microfabrication, Laser-fiber coupling, MEMS

Being currently performed on highly complex and expensive equipments, active optical alignment of single mode 10 Gb/s transmitters and receivers is proving to be the bottleneck process for high volume manufacturing. In order to alleviate this production burden, new integrated technologies are required to align micro-components like micro-lenses and optical fibers with photonic devices. Although passive alignment using Silicon micro-machined V-grooves seems to be very attractive at first, it has only been successfully implemented for micro-lens which can tolerate up to several microns of misalignment.

To resolve the latter issue, we propose a MEMS XY scanner mounted with a micro-lens to actively perform optical alignment of fiber optics modules by steering a beam. Although similar techniques have been demonstrated, we describe a unique technology using a 2x2.7 mm silicon bulk micro-machining chip characterized by $\pm 30\,\mu$m XY range of motion, electrostatic comb drives actuation and a silicon hybrid lens with alignment locking capability.

This thesis presents the design, fabrication and operation principle of an optical beam steerer for laser fiber coupling based on a MEMS device. The MEMS chip consists on a bi-dimensional movable platform based on uni-dimensional comb drive actuation. An optical lens is assembled onto the mobile platform to focus and steer the light coming from a laser diode and couple it into an optical fiber. Assembly of a complete system and measurements were performed and compared to simulation results. Both the trajectory of the MEMS and resonance frequency measurements agree with the simulated ones.

Résumé

Mots clés: Scanner optique, Silicium, Micro-fabrication, Couplage laser-fibre, MEMS

Etant actuellement exécuté sur de très complexes et coûteux équipements, l'alignement optique d'émetteurs et récepteurs de 10 Gb/s à fibres optiques monomodes se trouve être le talon d'Achille pour la fabrication à gros volumes de tels systèmes. Dans le but de résoudre ces problèmes, de nouvelles technologies doivent être développées pour aligner des micro-composants tels que les micro-lentilles et les fibres optiques avec d'autres modules optiques. Bien que l'alignement passif utilisant des structures de guidage intégrées semble intéressant à premier abord, elles ne peuvent être utilisées efficacement que pour des micro-lentilles pouvant tolérer des erreurs de positionnement de plusieurs micromètres.

Afin de résoudre ce dernier problème, nous proposons un nouveau scanner bidimensionnel MEMS comprenant une micro-lentille afin d'accomplir activement l'alignement optique de modules à fibre optique par déflexion d'un faisceau de lumière. Bien que des techniques similaires aient été démontrées, nous décrivons une technologie unique utilisant une puce en silicium microstructuré de 2x2.7 mm de côtés et caractérisé par un rayon d'action dans le plan XY de l'ordre de $\pm 30\,\mu$m, un actionnement à l'aide de peignes interdigités électrostatiques et une lentille en silicium hybride permettant d'être bloquée en place après positionnement.

Cette thèse présente la conception, la fabrication et le principe d'opération d'un déflecteur de faisceau lumineux basé sur une puce MEMS pour le couplage de la lumière entre une diode laser et une fibre optique. La puce MEMS consiste en un scanner bidimensionnel mobile basé sur un actionnement unidimensionnel à peignes interdigités électrostatiques. Une micro-lentille en silicium est assemblée sur la plateforme mobile afin de focaliser et dévier un rayon laser -provenant d'une diode laser- et de le coupler dans une fibre optique monomode. L'assemblage d'un système complet a été accompli et des mesures ont été effectuées à l'aide de ce module. Les résultats ont été com-

parés à ceux obtenus lors des simulations. Autant la mesure de la trajectoire du MEMS que sa fréquence de résonnance correspondent très bien avec les simulations.

Contents

List of Figures

List of Tables

Chapter 1

Introduction

Due to the limitations of data transmission by electrical connectors and cables, demand for reliable, fast and cheap optical networks increased these last decades. Optical networks components fulfilling complex requirements have to be developed and improved in various domains. A typical optical fiber network contains, but not limited to, at least some of the following components:

- Optical fiber. Can be either monomode or multimode. A monomode fiber allows only one mode to be transmitted into its core while a multimode fiber allows the transmission of several modes.
- Coupling system. This component is used to inject the light coming from a light source into an optical fiber.
- Switching unit. This component allows to switch the information coming from one fiber to another.
- Wavelength demultiplexer. This component performs the separation of the different wavelength traveling into an optical fiber.
- Wavelength multiplexer. This component allows to inject into a single fiber several signals of different wavelengths.
- Optical attenuator. This component can modify the amount of light of a channel. By masking part of the beam, it allows to modify the intensity of the light coming out of the optical fiber.
- Optical detector. This components detects the light signal coming out of the fiber and translates it into an electrical signal usable for the destination computer or server.

In computer networking, a transceiver (sometimes abbreviated to TCVR) is a device that performs, within a common housing, on one enclosure, both transmitting and receiving functions. It is sometimes designed for portable or mobile use, uses common circuit components for both applications, which provides half-duplex operation [6].

Fiber optical modules manufacturing have been recognized as a key challenge in meeting the anticipated demand for high bandwidth telecommunication equipment.

Incoming transceivers technology will enable data flow rate of 40 gigabit [7]. The increasing demand is due to the endless need for high speed data transmission. During these last years, computer users did not want to be limited to watch pictures or listen to music on the Internet (for example), they also want to watch live TV or movies with a high digital quality as HDTV. This is only possible by increasing the transmission rate of data.

Being currently performed on highly complex and expensive equipments [8], active optical alignment of single mode 10 Gb/s transmitters and receivers is proving to be the bottleneck process for high volume manufacturing. Figure 1.1 shows a scheme of a complete system currently built at Intel Corporation. The represented device is packaged in a butterfly housing (Figure 1.2). Among all challenges, submicron optical alignment for single mode fiber remains the predominant difficulty [9]. Performed on complex and expensive stations, optical active alignment is carried out by adjusting the optical elements mounted on metallic clips. First, they are pre-aligned and attached to the substrate. Then, if position correction is required, the metallic clips are deformed by laser hammering in order to reach the optimized position [10]. Other alignment technology can be found based on passive alignment using V-grooves or other techniques [11–15]. But in these cases, the optical setup has to tolerate misalignments of a couple of microns [16]. Another solution is to use large alignments systems based on piezoelectric or step up motor actuation driven by specific algorithms [17–19].

In order to alleviate this production burden, new integrated technologies are required to align micro-components like micro-lenses and optical fibers with photonic devices. Although passive alignment using Silicon micromachined V-grooves seems to be very attractive at first [20], it has only been successfully implemented for micro-lens which can tolerate up to several microns of misalignment [21]. Alternative solutions such as active MEMS alignment techniques have been employed mainly for switching applications. They are based on actuated micro-mirrors, causing incident collimated beams to be reflected onto another mirror or a focusing lens to illuminate a waveguide [22, 23]. A feedback loop mechanism is usually employed to dynamically optimize the coupling. Mostly used to select optical channels, these

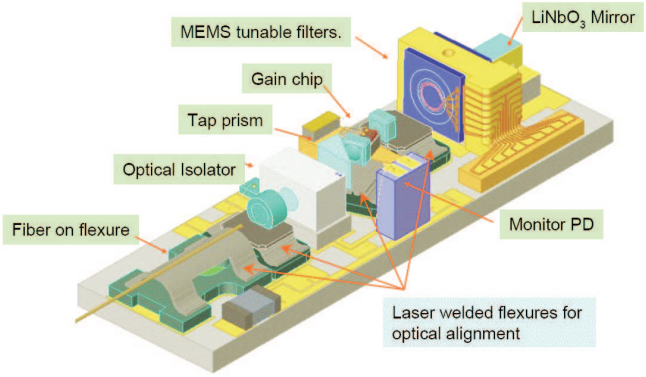

Figure 1.1: *Optical transceiver currently built at Intel (Courtesy Intel Corporation).*

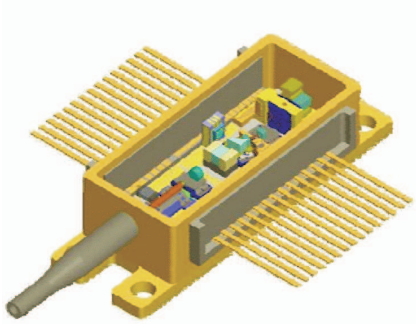

Figure 1.2: *Optical transceiver packaged in a butterfly housing (Courtesy Intel Corporation).*

micro-mirror active alignment methods are subject to the substantial insertion losses generated by the required collimators and pigtailling [24].

To reduce the alignment struggle during the assembly, a XY micro stage has been developed. It consists of a scanning platform with a mounted microlens on top. After a passive alignment of the components and the sealing of the package, a fine tuning of the lens position can be made by actuating the MEMS chip [25]. Once the maximal coupling efficiency is attained with a feed-back loop control, the lens can be locked in the optimal position. A new device had to be developed because the existing lens-based beam steerers, for example the ones described in [26, 27], did not reached all the desired specifications such as displacement range or maximal voltage. For example, the optical lens scanner presented by K. Takahashi [28] could theoretically reach the desired displacement range but the lens is too small and it is not possible to lock it in place once the optimal position reached. In [29], Kim and al. presents a micro XY-stage with a large enough displacement and platform size but the overall footprint of the chip (17x17 mm^2) is too large for the intended application.

Other types of components exist to steer light; some are based on tilting mirrors [30–32], liquid crystals [33–36] and more.

This thesis will describe the development and characterization of the MEMS XY beam steerer. First, the basic concepts used during development, fabrication and characterization will be described (Chapter 2). This chapter explains the fundamentals needed to fully understand the challenges and the choices made during the MOPOS (Micro Optical POsitioning System) project.

In chapter 3, the concept of the project will be developed. From the system configuration to the final design, all major choices and decisions will be explained and simulation results will be shown.

Then, after describing the fabrication process (Chapter 4), the results and characterization of the chip and the fully assembled system will be shown (Chapter 5). In this chapter, measurement results will also be compared with the data obtained during the simulation of the system.

Conclusion of the performed work and obtained results will finally be presented.

Chapter 2

Fundamentals

In this chapter, the basic theory of the concepts used for this thesis work will be presented. First, some principles used in movable MEMS will be discussed. These devices are commonly composed of a mobile structure held by mechanical springs and displaced by actuators. Second, some micro-fabrication steps will be explained. Then, some optical considerations will be exposed. Finally, the Veeco/Wyko NT1100 optical profilometer with dynamic measurements module (DMEMS) and the sticking phenomenon will be described.

2.1 Mechanical springs

In MEMS, when movable structures are used, the latter have to be attached to fixed parts of the device by suspension springs. Depending on the structures and the direction of motion of the mobile parts, different shapes are given to these springs. When comb-driven actuation is performed, the movable comb-drives have to be mobile but only in one direction. It is therefore highly desirable to have a spring very compliant in the targeted direction and stiff in the orthogonal one at the same time. Many different types of spring designs, such as [37] clamped-clamped beams, crab-leg flextures and folded-beam flexture, can be found in comb drive microactuators. In many applications, folded-beams are used. They offer the advantage of much higher stiffness in one direction and a very high compliance in the other one [38].

The value of the mechanical force of a complied beam is given by:

$$F_{\mathrm{M}} = k_{\mathrm{beam}} x \tag{2.1}$$

in the opposite direction than the movable end of the spring displacement x. The value of the elastic spring constant k_{beam} is calculated as follows:

$$k_{\mathrm{beam}} = \frac{12EI}{L^3} \tag{2.2}$$

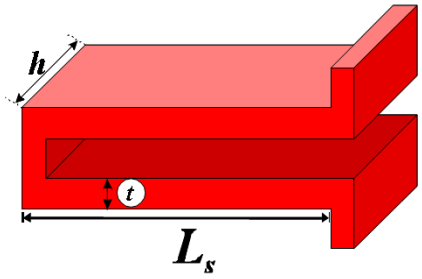

Figure 2.1: *Schematic of a folded beam spring.*

Where L is the length of the beam, E is the Young's modulus. The moment of inertia I of a rectangular beam with a width of t and a height of h, without rotation of the movable part, is given by [39]:

$$I = \int_{y_1}^{y_2} dy \int_{z_1}^{z_2} z^2 dz \tag{2.3}$$

$$I_{\text{rectangular}} = \int_{-h/2}^{h/2} dy \int_{-t}^{t} z^2 dz \tag{2.4}$$

$$= \frac{ht^3}{12} \tag{2.5}$$

The resulting force for a simple beam is then determined by:

$$F_{\text{M}} = \frac{Eht^3}{L^3} x \tag{2.6}$$

If such beam is used, in addition to the desired displacement, a perpendicular movement is also induced. To avoid this undesired motion, a second one can be added symmetrically. In this case, the displacement parallel to the beam axis is replaced by a large stress due to elongation of the beam.

In order to avoid these phenomena, folded-beam flextures [38] are commonly used (Figure 2.1). The principle is to design a "u-shaped" beam with a rigid elbow. In this case, the movement along the perpendicular axis is the same for both beam ends and is absorbed by the elbow end of the structure.

The restoring force for such an element is given by:

$$F_{\text{Mfolded}} = 2k_{\text{beam}} \frac{x}{2} \tag{2.7}$$

$$= \frac{Eht^3}{L^3} x \tag{2.8}$$

2.2 Electrostatic actuators

In MEMS devices, several actuation principles are used [40–42]. For some applications, a layer of piezoelectric material is deposited on the substrate. In other ones, a ferromagnetic component is created on the device, in order to actuate it with an external magnetic field [43, 44]. Other devices use the thermal expansion [45–47] properties of materials to obtain in-plane or out-of-plane displacements. All these methods require the deposition and patterning of one or more additional layers on the silicon wafer surface. It is also possible to displace movable parts by applying a voltage difference between the various parts of the device to create electrostatic actuation [48–50].

2.2.1 Parallel plate actuation

A plan capacitor (C_p) is formed of two parallel plates at an initial distance d_0, charged with an amount of charge q when a voltage U is applied.

The electrical force is defined by [51] :

$$F_\mathrm{E} = -\frac{1}{2}\frac{\partial C_\mathrm{p}}{\partial x}U^2 \tag{2.9}$$

In the case of a 1D displacement perpendicular to the plates, one obtains, starting with an initial distance D between the plates:

$$C_\mathrm{p} = \epsilon_0\epsilon_\mathrm{r}\frac{S}{D} \tag{2.10}$$

$$F_\mathrm{E} = -\frac{\epsilon_0\epsilon_\mathrm{r}}{2}\frac{hw}{(d_0-x)^2}U^2 \tag{2.11}$$

Where $S = hw$ is the surface of the plates and x is the relative displacement of one surface coming closer to the other.

Typically, electrostatic parallel plate actuators (Figure 2.2) are limited to small motion or bistable operation because large motion [52] can lead to the "pull-in" effect in which the actuator snaps closed [53–55]. The relationship between the actuator voltage and gap in equilibrium is plotted in figure 2.3. There is a maximum voltage V_pi for which the equilibrium exists. This pull-in voltage corresponds to a gap $d/d_0 = 2/3$. The maximal controlled displacement is:

$$x_{\mathrm{V_{pi}}} = \frac{1}{3}d_\mathrm{o} \tag{2.12}$$

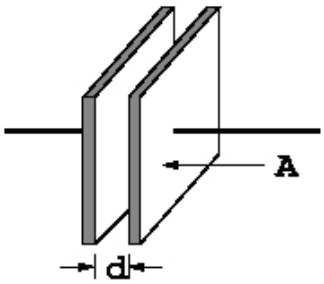

Figure 2.2: *Schematic of a parallel plate capacitor.*

If the voltage is increased slightly above V_{pi}, the snap-in phenomenon occurs. V_{pi} can be determined as follows:

$$V_{\mathrm{pi}} = \sqrt{\frac{8k{d_0}^2}{27C_0}} \tag{2.13}$$

Where k is the spring constant of the system linked to the mobile electrode.

It is possible to drive this kind of actuator by using charge control. For small parasitic capacitance ($C_{\mathrm{p}} < C_0/2$), there is one unique equilibrium gap for every value of charge between zero and q_{d}, the charge required to close the actuator. For larger parasitic capacitance, the snap-in gap is related with the value of this capacitance [56].

In order to increase the displacement range of a parallel plate actuator, lever systems have to be used [57, 58].

2.2.2 Comb-drive actuation

Comb-drives are often used in devices with structures held by mechanical springs. They can be used either for in-plane rotational [59], lateral actuation [29, 60–62] or out-of-plane motion [63].

In the case of comb-drives, we do not have only the force seen previously but also an additional one due to the overlap perpendicular to the displacement.

If h is the height of the device, N_{F} is the number of fingers and g is the gap between the combs, the resulting force is for a voltage U can be approximated as follows [64, 65]:

$$F_{\mathrm{E}} \approx -\epsilon_0\epsilon_{\mathrm{r}}\frac{hN_{\mathrm{F}}}{g}U^2 \tag{2.14}$$

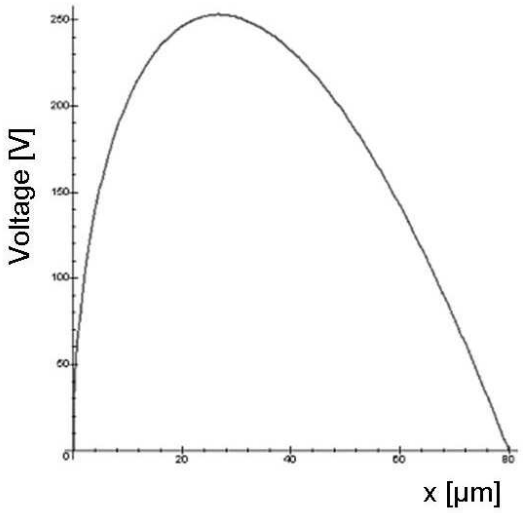

Figure 2.3: *Plot of the voltage versus displacement of a parallel plate capacitor (example). The pull-in occurs at about one third of the maximal displacement.*

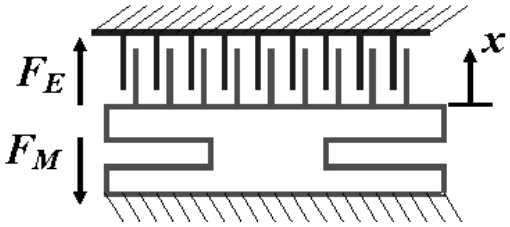

Figure 2.4: *Schema of comb-drives held by springs.*

As the elastic force of a beam is given by equation 2.15 where E is the Young's modulus, L is the length of the spring and t is its width:

$$F_{\mathrm{M}} = \frac{Eht^3}{L^3}x \tag{2.15}$$

The sum of the forces in the situation of figure 2.4 gives the following displacement versus the voltage:

$$x = \frac{1}{2}\frac{\epsilon_0\epsilon_{\mathrm{r}}N_{\mathrm{F}}L^3}{gEt^3}U^2 \tag{2.16}$$

In this case, the displacement varies in function of the square of the voltage.

These equations and especially equation 2.14 are valid only if the movable combs are perfectly centered between the fixed ones. If it is not the case, the

lateral forces of parallel-plate type as seen in section 2.2.1 are not the same on each side, creating an instability in the system. Comb-drives actuation can be described as an instable equilibrium. To avoid any lateral motion of the movable part of the actuator, the mechanical springs have to be correctly designed and optimized.

2.3 Technology

In this section, a brief overview of the microfabrication processes will be shown. Fundamental principles and physical laws relevant for this work will be investigated.

In microtechnology, almost all the fabrication steps are based on chemical reactions either by placing the substrate in a chemical fluid or into a plasma. In order to protect the parts of the wafer that should not react with its environment, a mask with the desired pattern is deposited on the substrate. The technology used for this step is called photolithography.

2.3.1 Photolithography

In photolithography, a layer of photoresist is spun (or sprayed [66]) on the surface of the wafer. Then, after a short prebake, the wafer is exposed to light coming from a UV lamp and passing through a chrome mask. This mask stops the light where the metal is and is optically transparent anywhere else. As the resist spun is photosensitive, it reacts with the incoming light. There are two photoresist families; the positive and the negative ones. Positive resists are rendered soluble in developer when exposed to UV light. Negative resists are rendered insoluble in developer when exposed to UV light.

Once the photoresist is exposed, it is developed in a developer (solution typically made from diluted KOH or NaOH), and postbaked in an oven.

This photoresist mask can then be used as a mask in almost every etching bath or plasma to pattern the underlying layer.

2.3.2 Silicon oxide growth/deposition

Semiconductors can be oxidized by various methods [67]. These include thermal oxidation, electrochemical anodization, and plasma reaction. In this section, a brief overview of thermal oxidation and oxide deposition is shown.

Thermal oxidation

Among the oxidation methods, thermal oxidation is by far the most important for silicon microfabrication. The thermal oxidation setup consists of a fused quartz tube heated at high temperature. The silicon wafers are inserted into the tube with a fused quartz boat.

Thermal oxidation in oxygen or water vapor is describing by the following chemical reactions:

$$Si(\text{solid}) + O_2(\text{gas}) \longrightarrow SiO_2(\text{solid}) \tag{2.17}$$

$$Si(\text{solid}) + 2H_2O(\text{gas}) \longrightarrow SiO_2(\text{solid}) + 2H_2(\text{gas}) \tag{2.18}$$

Equation 2.17 describes the reaction of dry thermal oxidation and equation 2.18 explains the principle of wet oxide formation. For thick layers of oxide, the wet process is used because for a given temperature and time, the oxide film obtained is about 5 to 10 times thicker than that using dry oxidation [67]. Figure 2.5 shows experimental results of wet oxide thickness as a function of the reaction time. Nevertheless, as the oxidation rate decreases with time, it becomes very expensive and time consuming to grow thick layers of oxide. This explains why standard thermal oxide layers are typically limited to $3\,\mu$m or less.

Silicon oxide deposition

Dielectric layers such as - but not limited to - silicon oxide can be commonly deposited by three deposition methods [67]: atmospheric-pressure chemical vapor deposition (CVD), low-pressure chemical vapor deposition (LPCVD), and plasma-enhanced chemical vapor deposition (PECVD) [68]. Table 2.1 summarizes the advantages, disadvantages as well as pressures and temperatures for these three types of CVD deposition [5].

2.3.3 Metalization

In microsystems, chips have to be metalized to connect electrically different parts of the chip and contact the device to the driving electronics. The metal is typically deposited by evaporation, electro- or electroless deposition [69–71]. In some applications, a deposition of gold on the whole chip is made without any patterning step [72, 73]. In other situations, the metal layer has to be patterned. Several technologies can be used to obtain a patterned metalization.

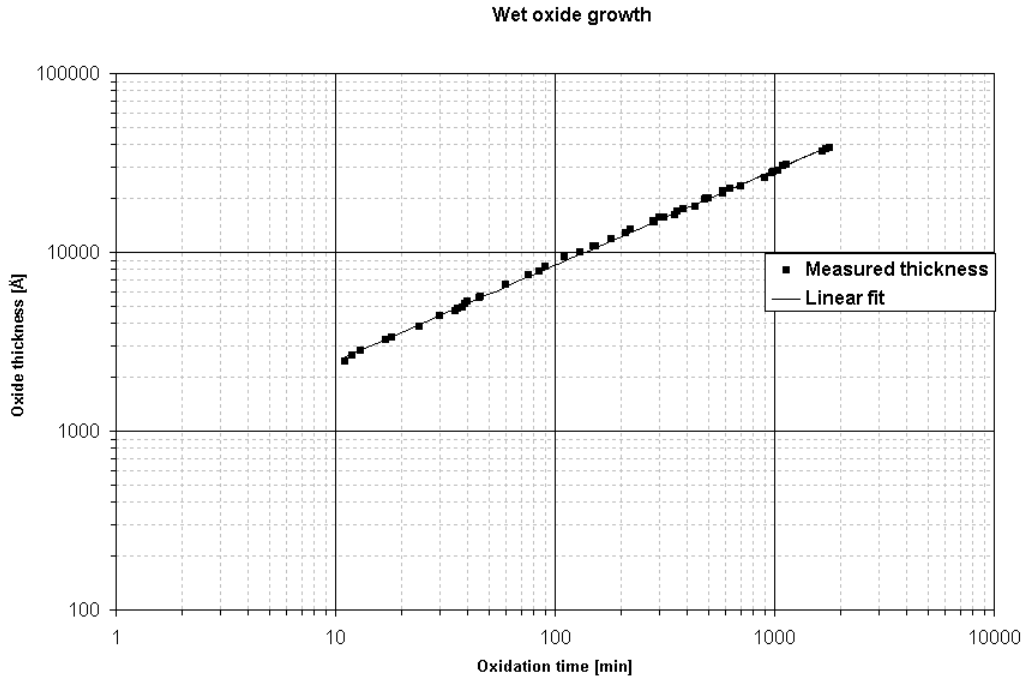

Figure 2.5: *Experimental results obtained in the oxidation oven of our cleanroom of silicon dioxide thickness as a function of reaction time for a temperature of 1100°C.*

Process	Advantages	Disadvantages	Pressure/ Temperature
CVD	Simple, high deposition rate, low temperature	Poor step coverage, particle contamination	100-10 kPa / 350-400 °
LPCVD	Excellent purity and uniformity, conformable step coverage, large wafer capacity	High temperature and low deposition rate	100 Pa / 550-600 °
PECVD	Lower substrate temperatures, fast, good adhesion, good step coverage, low pinhole density	Chemical (e.g. hydrogen) and particulate contamination	200-600 Pa / 300-400 °

Table 2.1: *Review of some of the standard oxide deposition processes [5].*

Metal	Etchant
Nickel	Nitric, sulfuric or phosphoric acids
Titanium	Hydrofluoric, phosphoric or sulfuric acids
Gold	Gold etch (e.g. KI+I_2)
Aluminum	"Alu etch" (H_3PO_4+CH_3COOH+HNO_3+H_2O)
Chrome	"Chrome etch" (e.g. H_2CrO_4+H_2SO_4)

Table 2.2: *List of some metals commonly used in microfabrication and corresponding etchants.*

Chemical etching

Wet chemical etching is a well established standard technique for metal patterning. It exists an etchant for every metal commonly used in microfabrication.

Table 2.2 shows some examples of metals and their etchants. For most of the metals not etched in common acids (i.e. platinum), aqua regia at high temperature can be used. The major disadvantage of this technique is that the etch time can be quite long for thick metal layers. As these etchings are isotropic, underetching can be important. Furthermore, to pattern the metal, a layer of photoresist has to be spun on the wafer and it is almost impossible if deep structures are already opened on the surface of the substrate.

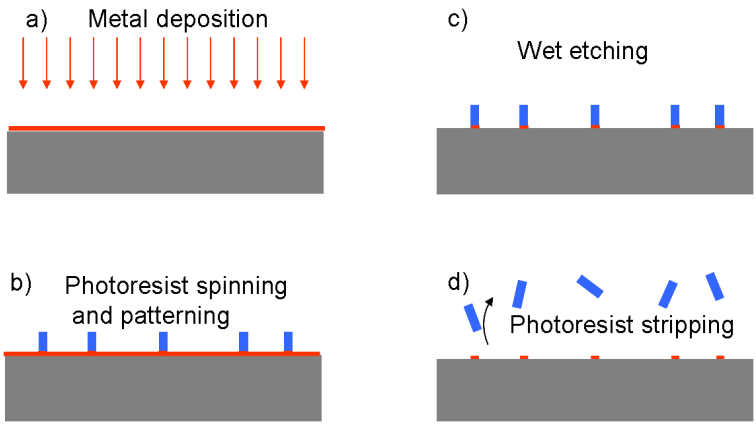

Figure 2.6: *Wet etching process for pattern transfer.*

Finally, this process needs the wafers to be immersed into a liquid solution. Sometimes, any wet processes have to be avoided.

It also exists a dry chemical etching technology. It is based on a plasma etching (similar to silicon dry etching, Section 2.3.4) technology. Depending on the gases forming the plasma, it is possible to vary the etch rates and selectivities on various materials. The disadvantage of this technology is that usually, the plasma etching is feasible only for one wafer at a time while wet etching can be made for several wafers at the same time, it is less expensive and less time consuming. Figure 2.6 shows the wet etching principle.

Lift-off process

In the lift-off technique, a photoresist (typically positive) is used to form the pattern on the substrate (Figure 2.7 a) and 2.7 b)). The film (typically metal) is deposited over the resist and the substrate (Figure 2.7 c)); the thickness of the film must be smaller than that of the resist. Those portions of the film on the resist are removed by selectively dissolving the resist layer in an appropriate liquid etchant so that the overlying film is lifted off and removed (Figure 2.7 d)). The lift-off technique is capable of high resolution and is used extensively for discrete devices. It is the easiest method, because it involves only one mask step and the photolithography is completely standard. However, it is not as widely applicable for very-large-scale integration in which dry etching is the preferred technique [67].

The main disadvantage of this method (for standard positive photoresists) is that film is deposited on the sidewall of the photoresist and will generally continue to adhere to the substrate following resist removal. This sidewall

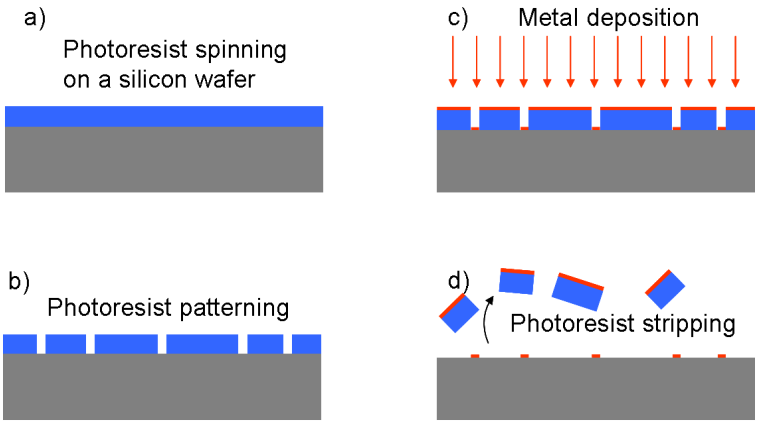

Figure 2.7: *Lift-off process for pattern transfer.*

may peel off in subsequent processing, resulting in particulates and shorts, or it may flop over and interfere with etches or depositions that follow. Depending on how robust the film and substrate are, sidewalls from deposited film can be removed using a gentle swipe of a clean-room swab or a directed stream of acetone from a squeeze bottle [74].

To avoid the deposition on the sidewalls, lift-off resist (LOR) can be used. The LOR is first spun on the wafer and baked, then standard photoresist is spun on and baked. The resist is exposed as usual, and then the substrate is developed. The standard developer will clear the exposed areas, but will also "etch away" the LOR, leading to undercutting of the photoresist. It is this overhang that prevents sidewall deposition of film. The resist can be lifted-off using a specific solvent. Because the overhang profile is caused by undercutting the resist, care must be taken to avoid completely undercutting (and lifting off) very narrow geometries. Metalization using the lift-off process has other advantages. With this technique, the deposited metal is never in contact with the silicon wafer on the areas that should not be metalized. This limits the possible cross-contamination that can cause problems for sensors, for example.

Shadow mask

This technique is based on the lift-off principle but by using another structured wafer instead of patterned photoresist. Photoresist is spun and patterned on a wafer. The latter is then etched through in order to form holes having the same shape than the desired metalization. The wafers are put in contact (Figure 2.8 b)) and the metal is evaporated on its surface (Figure 2.8 c)). Metal particles will also get into the holes and deposit on the

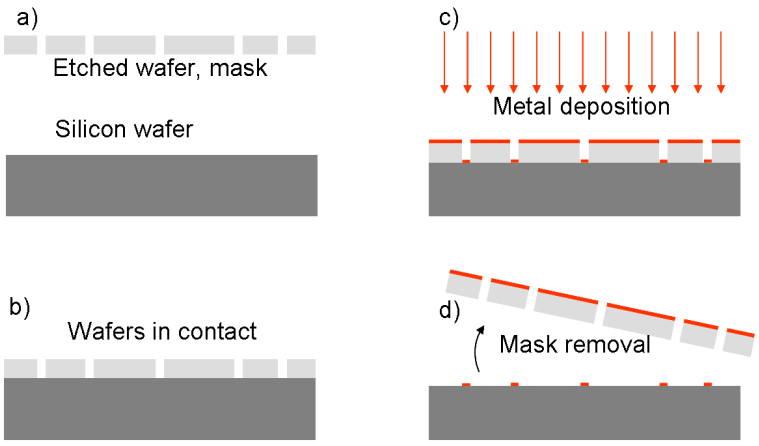

Figure 2.8: *Shadow mask process for pattern transfer.*

silicon wafer to be metalized. Finally, the perforated wafer has to be taken off (Figure 2.8 d)).

The major advantage of this method is that, for thick metal layers, the metal is not deposited on the whole wafer but only on the spots where it has to be in the end of the process. This method has three major inconveniences:

1. It is not possible to create small and very precise structure. As the mask is made of another silicon wafer etched through, DRIE limitations do not permit very thin and small features.

2. The stress of the metal deposition is applied on the mask. As the latter is not bonded to the silicon wafer, a certain bow is created and it results in the formation of a variable gap between the mask and the wafer. This gap produces a deformation of the "shadow" of the mask, returning an inhomogeneity in the deposition of the metal layer.

3. It is very difficult to align the wafers and to hold them together precisely. This method is then preferably used in the beginning of a process.

Nevertheless, this technique can be used and works well for large areas with a low precision required. It is also possible to create smaller structures by patterning them in a silicon nitride membrane and opening large grooves in the silicon by KOH. Although this method allows small and precise structures, their alignment on the wafer with existing structures is very challenging.

2.3.4 Silicon dry etching

In microfabrication, silicon substrates are usually used due to its semiconductor properties and its low price. Silicon is also suitable for bulk micromachining thanks to its single cristal arrangement and its good mechanical properties. It is possible to etch it either in a wet or in a dry way. The wet etching of silicon is made in a potassium hydroxide (KOH) bath and dry etching in a plasma process called RIE (Reactive Ion Etching) [75–78].

In RIE, the substrate is placed inside a reactor in which several gases are introduced. A plasma is created in the gas mixture using an RF power source, breaking the gas molecules into ions. The ions are accelerated and react at the surface of the material to be etched, forming another volatile material. This is known as the chemical part of reactive ion etching. There is also a physical part which is similar in nature to the sputtering deposition process. If the ions have high enough energy, they can knock atoms out of the material to be etched without a chemical reaction. It is a very complex task to develop dry etch processes that balance chemical and physical etching, since there are many parameters to adjust. By changing the balance it is possible to influence the anisotropy of the etching. As the chemical part is isotropic and the physical part highly anisotropic, the combination can form sidewalls that have shapes from rounded to almost vertical.

DRIE Principle

Silicon deep reactive ion etching (DRIE) is a versatile tool for the fabrication of MEMS. It enables bulk micromachining of silicon with aspect ratios (ratio depth to width) up to 30:1 and sidewall angles of $90\,^{\circ}\pm1\,^{\circ}$. Compared to other bulk micromachining methods it is anisotropic and independent of the crystal orientation. Therefore, it allows a high degree of design freedom. Feature sizes in the submicron range can be realized. It can be used for many different applications by combining it with other technique [79–83].

The basic idea of silicon deep reactive ion etching (DRIE) is an alternating etch and surface passivation steps. This process has been developed and patented by Robert Bosch GmbH [84]. The dry etching of silicon according to this principle is also called High Aspect Ratio Silicon Etching (HARSE), Bosch Deep Silicon Etching, or Advanced Silicon Etching (ASE; Trademark of Surface Technology Systems Ltd. [85]).

Depending on the etch depth and the mask layout, the etch rate can be over $10\,\mu$m/min [86], the surface roughness of the sidewall as low as a couple of tens of nanometers, or the homogeneity of the etch depth less than $\pm3\%$ (on a 4" wafer). However, the final etch result is mostly a compromise. With

a high etch rate, the surface roughness increases, with a large etched silicon area the inhomogeneity will increase to above ±10% [87, 88].

For this process, SF_6 and C_4F_8 are the standard gases. It exists also other chemistries combinations with different etch rates and properties. The SF_6 gas supplies fluorine radicals for spontaneous isotropic etching of exposed silicon as shown in equations 2.19 to 2.22 [1].

$$SF_6 + e^- \longrightarrow S_xF_y{}^+ + S_xF_y{}^\bullet + F^\bullet + e^- \quad (2.19)$$

$$Si + F^\bullet \longrightarrow Si - nF \quad (2.20)$$

$$Si - nF \xrightarrow{ion\ energy} Si - F_x(ads.) \quad (2.21)$$

$$Si - F_x(ads.) \longrightarrow Si - F_x(gas) \quad (2.22)$$

The C_4 F_8 plasma deposits a $(C_xF_y)_n$ polymeric passivating layer on all substrate features. The directional ion energy supplied by the capacitively coupled platen electrode during the etch step preferentially removes the passivation from the base of the features hence exposing silicon for spontaneous etching. The balance between etch and passivation determines the final process results and this balance can be controlled through a wide variety of process parameters (etch cycle time, SF_6 flow rate, etch cycle powers and pressures, C_4F_8 flow rate, ...) [1, 89]. A schematic of a typical deep reactive ion etching system is shown in figure 2.9. To achieve reproducible results, any metal contamination has to be avoided in the chamber. If some metal particles (for example) are present during etching, the etching quality can differ at several levels (sidewalls roughness, etching speed, and more).

For the fabrication of movable structures, silicon-on-insulator (SOI) wafers are often used. The oxide beneath the silicon device layer acts as an etch stop. By a subsequently removal of the oxide the structures are released. During the etching of such a wafer, the etching stops on the Si/SiO_2 interface due to the different etch rates of silicon and silicon dioxide. Unfortunately, in these circumstances, the notching problem can appear.

Notching

Notching is a phenomenon that occurs during a DRIE etching [90, 91]. The etch rate is not the same on the whole wafer but depends on the size of the etched structures. In consequence, the oxide layer will be reached earlier in larger opened structures. Once this layer attained, the vertical etch is almost stopped but a lateral etching appears in the interface. This horizontal opening is very thin and is often not a problem. Sometimes, especially for

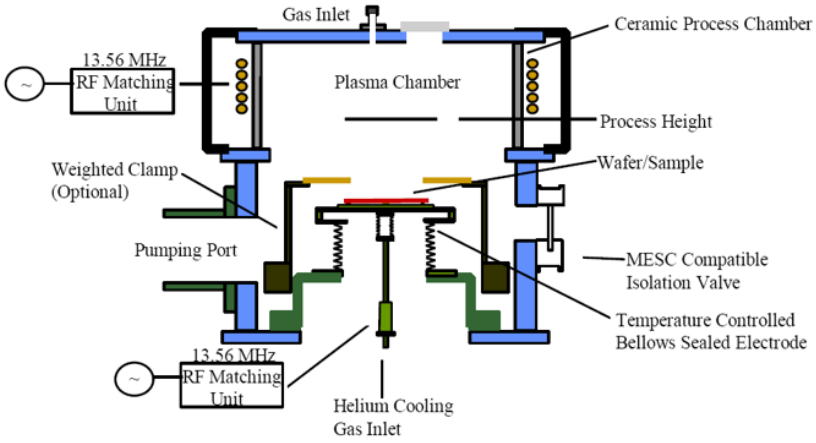

Figure 2.9: *Schematic view of a modern DRIE system [1].*

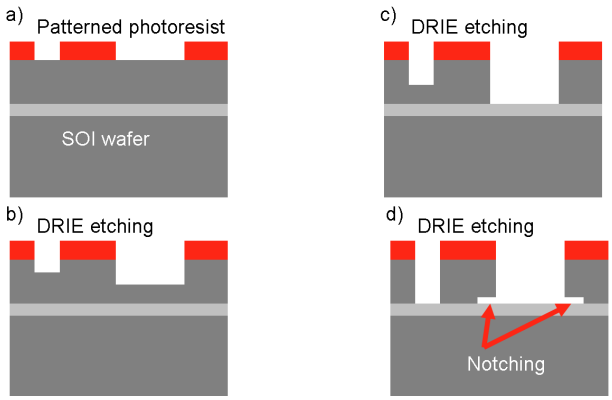

Figure 2.10: *Schematic view of the notching effect.*

small structures, it can cause problems. Figure 2.10 shows a schema of the notching principle.

One solution to avoid this phenomenon is to use standard silicon substrates combined with the SCREAM process [92, 93] but it has some other disadvantages we will not detail here.

2.3.5 Silicon wet etching

As mentioned, wet etching using KOH can be used to pattern silicon structures [94–96]. It dissolves a given cristal plane much faster than other planes. This results in orientation-dependent etching. The different etch rates of

KOH, at about 80 °C, are the following:

- 0.6 μm/min for the (100)-plane
- 0.1 μm/min for the (110)-plane
- 0.006 μm/min (60 Å/min) for the (111)-plane

This orientation dependant etching of <100>-oriented planes through a patterned mask (made of silicon nitride or silicon dioxide) creates precise V-grooves. The obtained structures have an angle of 54.7 ° from the (100)-surface. If <110>-oriented is used, vertical walls with sides of (111)-planes can be etched [67, 97].

2.3.6 Delay mask process

DRIE etching principle, used to etch deep vertical structures into silicon, is explained in section 2.3.4. To create more complex 3D structures it is possible to use this process with different etch times in order to get structures with different etching depths [98]. Figure 2.11 shows the process flow of this technology. As it is not possible to perform a reliable and precise photolithography on a wafer processed with deep trenches, the two masks (for a two step delay mask process) have to be defined before the first DRIE. The basic principle is then to etch first the shape given by the surface mask (Figure 2.11 h)), to remove it and then to etch again with the second mask (Figure 2.11 j)). Of course, the second mask should not be stripped during removing the first mask. For this reason, the first mask can be made of photoresist but the second one has to be made of metal or oxide. As metal masks can cause problems inside the DRIE chamber, an oxide mask is commonly used.

To create this mask, an oxide layer has to be grown on top of of the silicon wafer. The oxide thickness depends on the depth of silicon to be etched. In standard DRIE processes, the selectivity between oxide and silicon is about one to one hundred. It means that if 100 μm have to be etched, an oxide mask of at least 1 μm is needed. That way there is no etch depth limitations but as shown in section 2.3.2, it is not standard to create oxide thicknesses of several micrometers. The etching depth is then limited to about one hundred times the maximal oxide thickness available.

2.3.7 Oxide etching

Oxide can be etched either in a wet, dry or quasi-dry way.

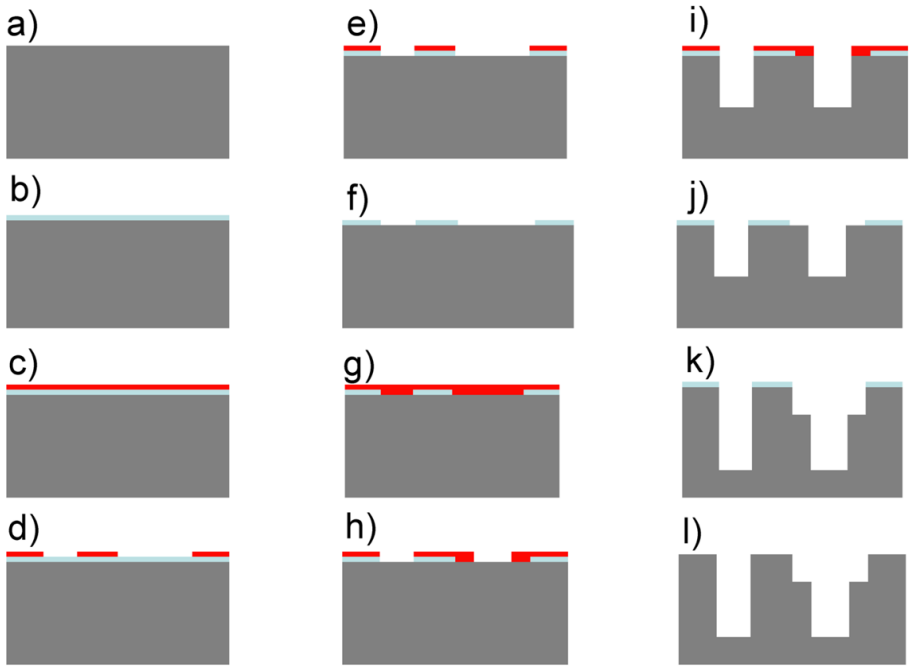

Figure 2.11: *Schematic of the delay mask process. a) Bare wafer. b) Growth of an oxide layer. c), d), e) and f) Patterning of the oxide by photolithography. g) and h) Patterning of the photoresist mask. i) First DRIE. j) Stripping of the photoresist mask. k) Second DRIE. l) Removal of the oxide mask (optional).*

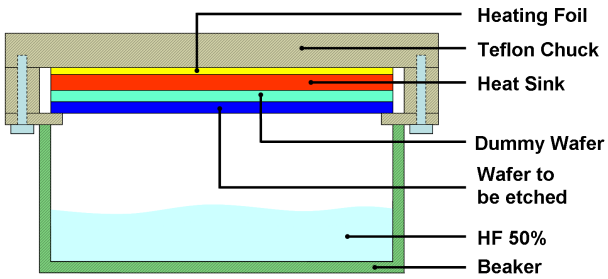

Figure 2.12: *Schematic cross section view of a vapor etcher [2].*

Dry etching of silicon dioxide is based on plasma technology. This process can be done either isotropically or with a certain directionality.

The wet etching of the oxide is performed in a HF or BHF bath.

BHF is a solution of concentrated HF (49%), water, and a buffering salt, NH_4F. This solution is referred to as buffered HF, or BHF. The buffering agent is added to maintain a constant pH, and thus a constant etch rate, as the HF is consumed in its reaction with SiO_2 [99]:

$$SiO_2 + 4HF + 2NH_4F \rightleftharpoons 2NH_4^+ + SiF_6^{2-} + 2H_2O \tag{2.23}$$

HF can be used to etch SiO_2 either in a wet or vapour phase way. For wet HF etching, the substrate is immersed in an HF bath the same way than with BHF. In that case, the chemical reaction is the following [99]:

$$SiO_2 + 6HF \rightleftharpoons 2H^+ + SiF_6^{2-} + 2H_2O \tag{2.24}$$

For some applications, when the wet process has to be avoided and the dry etching is not suitable, it is possible to use the quasi-dry etching process based on vapor phase HF [100].

The arrangement for the HF/H_2O etching is shown in figure 2.12. A teflon vessel containing hydrofluoric acid at a concentration of 50% in H_2O is closed with a cap. On this cap, the wafer is placed on a heater in order to be able to heat the wafer to a precisely controlled temperature. The temperature of the wafer [101] or the difference between the HF solution and the wafer determines the etching rate of the process [102]. Furthermore, the etching time has also an influence on the etch rate. This can be explained by the fact that the HF vapor etch has an incubation period before etching really starts [101, 103].

2.4 Optical components

In Optical MEMS, the most frequently used optical components are [104, 105]:

- Micromirrors
- Microlenses

Some examples will be given about these two research fields.

2.4.1 Micromirrors

MEMS mirrors are commonly used for applications such as but not limited to switches, scanners or displays.

For some applications, the surface of the wafer is used [30, 32]. As the surface of the wafer is polished, it has very good optical properties and very little roughness. For this reason, it is possible to reflect light with very low losses. Depending on the wavelength of the light, the surface has to be metalized to become reflective because silicon is transparent in the infrared region. In optical telecommunications, the light commonly used has wavelengths comprises in the infrared, between 1310 and 1620 nm. As silicon is transparent in this part of the spectrum, a layer of gold (or aluminum) is deposited on the silicon micromirror.

In other applications, the mirror is vertical in the silicon wafer [72, 73, 106–109]. In this case, the surface used is etched into the silicon by DRIE (Section 2.3.4), but it is quite difficult to obtain an optically flat surface with such a process.

It is also possible to create inclined mirrors with KOH etching technology (Section 2.3.5) or vertical ones precisely defined by the silicon crystal planes. Different research groups also carried out experiments to combine both techniques in order to have the design liberty given by DRIE etching and optically flat surfaces defined by the crystal planes of silicon [82, 97].

2.4.2 Microlenses

Microlenses are not very often used in MEMS chips. There are some applications such as scanning, switching or beam steering but most of the systems are made using a micromirror. The reason is that it is much more difficult to integrate a lens into a MEMS device than a mirror. In the next subsections, the light coupling problem will be discussed and the microlens fabrication will be presented.

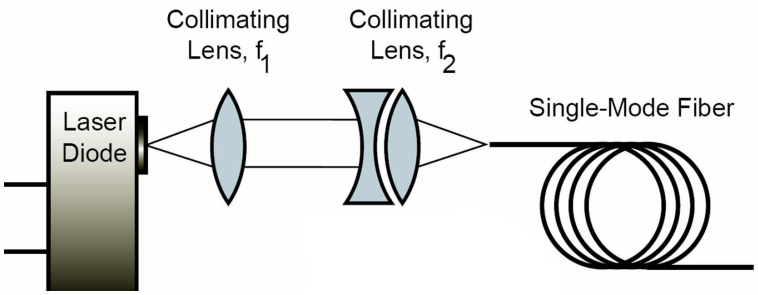

Figure 2.13: *Standard method for the coupling of light between a laser diode and an optical fibre. The light is first collimated and then focused into the core of the optical fiber.*

Light coupling

Light coupling is a bottleneck to a larger use of optical telecommunications. The optimization of the amount of light coming from a laser diode and injected into an optical fiber is still quite expensive and time consuming. It is currently performed by expensive laser-welding stations using technologies such as laser welding and hammering [10] or mechanical deformation of flextures [110] as seen in chapter 1.

Figure 2.13 shows the standard principle of light coupling. The light emitted by the laser diode is collimated by a first lens. It transforms a diverging beam into a well-defined collimated beam. Then, a second lens focus the collimated light beam into the core of the optical fiber. As the core of single mode fibers is typically 5 to 10 μm in diameter [111], the optical system has to be positioned very precisely.

Even if a perfect alignment could be performed, miniaturized light coupling would never reach 100%. This is due to physical constraints such as diffraction (Section 2.4.3) and the angle of aceptance of the optical fibers (Section 2.4.4).

Microlenses fabrication technology

A large variety of fabrication techniques have been applied to the fabrication of refractive micro optical elements [112]. The two main methods used are; surface profile and gradient-index optics [113]. Here, we will only explain one technique used to build silicon based microlenses. This method is based on two basic microfabrication steps explained in section 2.3: photolitography and silicon dry etching. Details about fabrication of diffractive micro optical elements can be found in [114, 115].

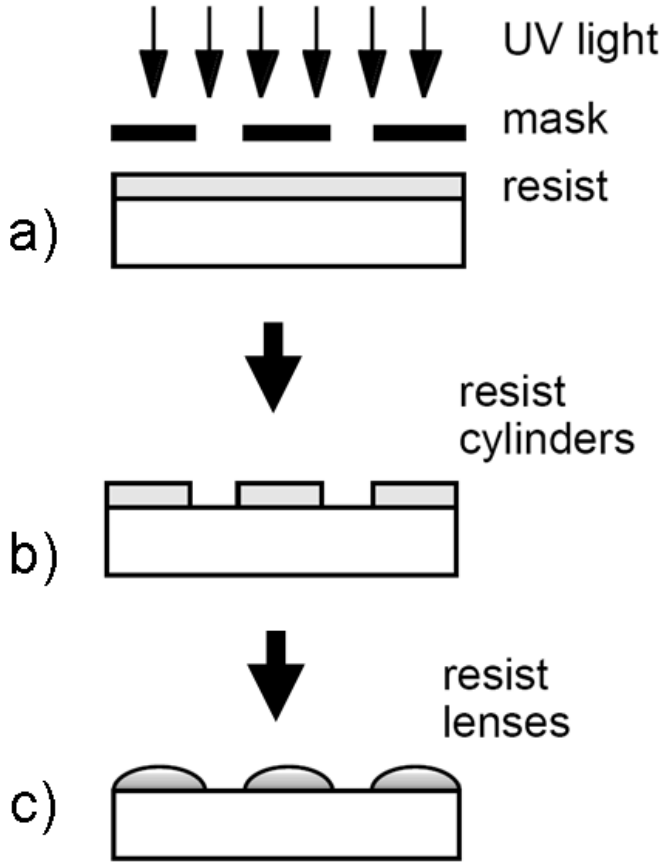

Figure 2.14: *Microlens fabrication technology using photoresist reflow. a) Exposure of photoresist with a cylindrical shape. b) Development of the photoresist to obtain resist cylinders. c) Photoresist reflow to obtain a spherical shape. The shape can then be transferred into the substrate by RIE. [3]*

The way to fabricate refractive microlenses is by melting cylindrical "islands" of photoresist (or similar polymer material) [116]. Figure 2.14 shows the fabrication process [3].

First, a photoresist layer is patterned lithographically to form small cylinders on a substrate. This substrate can be made of silicon, or quartz, depending on the wavelength to be used in the final application of the microlens. For infrared light, silicon is generally used as it is transparent for this wavelength range [117].

Second, the obtained structure is heated to a temperature above the glass temperature of the photoresist (Typ, T ≈160°). At these temperature, the photoresist melts and its surface changes in the way to minimize its surface tension energy [118]. This is usually called the "reflow"process. The shape obtained is approximately spherical and the focal distance of the obtained photoresist lens (down to a certain size, limited by diffraction) can be determined by:

$$f = \frac{r_c}{n-1} \tag{2.25}$$

The radius of curvature can be determined either from the volume of the initial photoresist cylinder of thickness t and diameter D:

$$V_{cyl} = \pi \left(\frac{D}{2}\right)^2 \cdot t \tag{2.26}$$

or after its reflow:

$$V_{cap} = \pi h^2 \frac{3r_c - h}{3} \tag{2.27}$$

where h is the sag of the lens. h is related to the radius of curvature and the diameter of the lens by [113]:

$$r_c = \frac{h^2 + \frac{D^2}{4}}{2h} \tag{2.28}$$

By assuming that the photoresist volume does not change during reflow, there is a relation between the initial photoresist layer thickness and the lens sag:

$$t = \frac{h}{6}\left(3 + 4\frac{h^2}{D^2}\right) \tag{2.29}$$

Starting from equations 2.28 and 2.29 it is possible to determine the required photoresist thickness for a lens with a diameter D and a focal distance f desired. Figure 2.15 shows the relation between these three parameters.

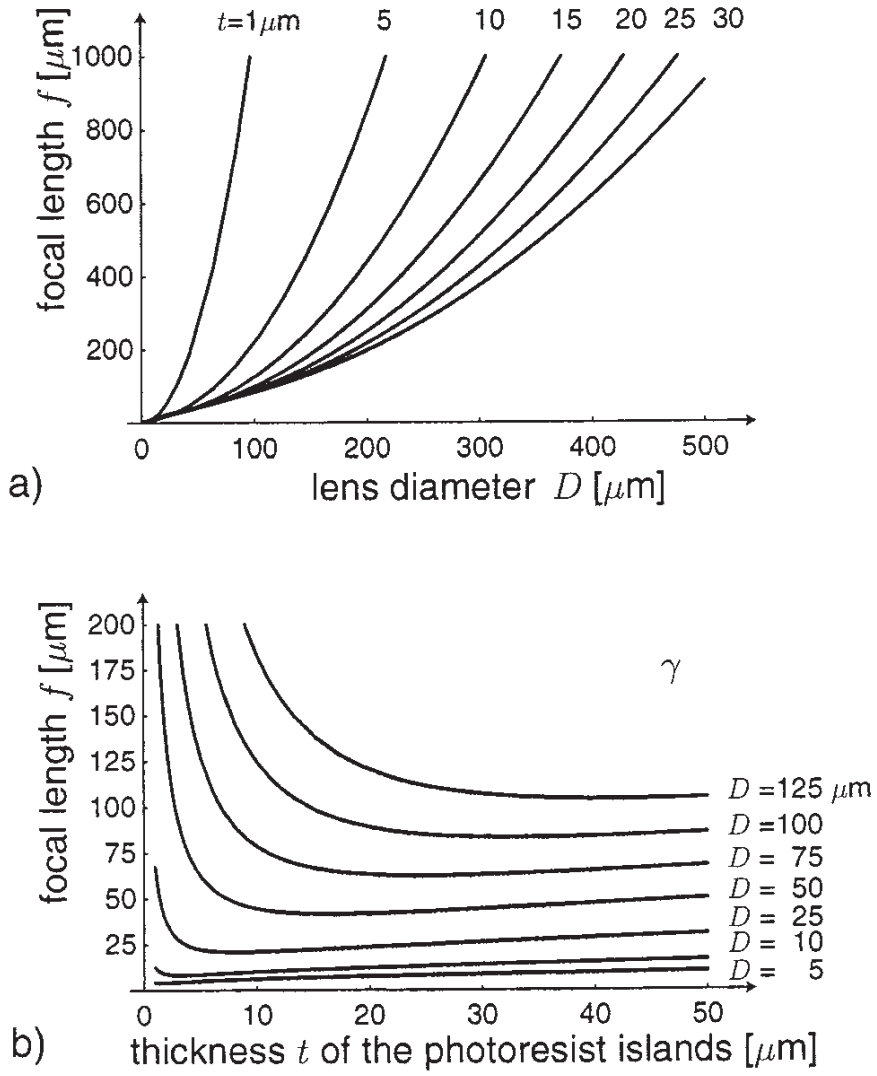

Figure 2.15: *Focal length of a photoresist microlens depending on its diameter and the initial photoresist cylinder thickness.*

Once the photoresist microlens is formed it can be used directly [119]. It is usually the case for CCD and CMOS image sensor. For some applications, "ink jet"lenses are also used. As seen in figure 2.14, it can also be transferred into the substrate [120, 121]. This operation is performed by dry etching, typically RIE (Reactive Ion Etching). During etching, by adapting the parameters of the machine, it is possible either to replicate exactly the shape of the lens or modify it by changing the etch rate of photoresist versus the etch rate of the substrate. This technique is used for example to obtain relatively high microlenses having a large diameter and a high sag. In this case, the photoresists does not melt with creating a spherical shape. Thus, a thinner photoresist lens is patterned and a higher etch rate of the substrate is performed. This creates a lens with the same diameter than the photoresist one but with a higher sag. In this case, the shape of the microlens is not perfectly spherical but has a given deviation from the spherical shape. This deviation from a perfect spherical shape is called the K factor of the lens. In this case, the radius of curvature of the lens is given by:

$$r_c = \frac{h(K+1)}{2} + \frac{(D/2)^2}{2h} \tag{2.30}$$

The lens shape can be deducted from the K factor with the following rules:

K > 0	Ellipsoid
K = 0	Sphere
-1 < K < 0	Ellipsoid
K = -1	Paraboloid
K < -1	Hyperboloid

This process can be used either to create single lenses or arrays of lenses [122].

Some optical microsystems are based on ball lens [123, 124]. The fabrication process of these will not be described here and can be found in [125].

2.4.3 Microlenses performance

The performance of microlenses is limited by two main factors:

- Diffraction
- Aberrations

What is diffraction?

In this subsection, the phenomenon of diffraction of light is discussed. The diffraction limits the efficiency of microoptical components such as microlenses in microoptical systems.

When light passes through a small hole or a thin slit made in an opaque screen, the image that can be seen at a certain distance of the screen is called the diffraction pattern. The shape of this pattern can be very different than the aperture shadow. The resulting image depends on the distance of the observation plane, the wavelength of the light and the dimensions of the aperture. In case of a laser diode, the aperture of the diode can be compared to such a small hole. This is the reason why, the smaller the lens opening, the larger its numerical aperture.

Fraunhofer diffraction theory can be used to determine the shape of a light spot after passing through a small aperture ($p(x, y)$). The Fraunhofer approximation is valid for large propagation distances d [126].

For an incident plane wave of intensity I_i travelling along the z axis:

$$U(x,y) = \sqrt{I_\mathrm{i}} \tag{2.31}$$

$$f(x,y) = \sqrt{I_\mathrm{i}} p(x,y) \tag{2.32}$$

The Fraunhofer approximation gives:

$$g(x,y) \approx \sqrt{I_\mathrm{i}} h_0 P(\frac{x}{\lambda d}, \frac{y}{\lambda d}) \tag{2.33}$$

$$P(x,y) = \int\int_{-\infty}^{\infty} p(x,y) exp\left[\mathrm{j}2\pi(\nu_x x + \nu_y y)\right] dxdy \tag{2.34}$$

Where $P(x, y)$ is the Fourier transform of $p(x, y)$ and $h_0 = (\mathrm{j}/\lambda d) exp(-\mathrm{j}kd)$.

The diffraction pattern is then proportional to the squared magnitude of the Fourier transform of the aperture function:

$$I(x,y) = \frac{I_\mathrm{i}}{(\lambda d)^2} \left| P(\frac{x}{\lambda d}, \frac{y}{\lambda d}) \right|^2 . \tag{2.35}$$

In the case of a circular aperture of diameter D, the diffraction pattern is defined by:

$$I(x,y) = I_0 \left[\frac{2J_1(\pi D\rho/\lambda d)}{\pi D\rho/\lambda d} \right]^2 \tag{2.36}$$

$$\rho(x,y) = \sqrt{x^2 + y^2} \tag{2.37}$$

where $J_1()$ is the Bessel function of order 1 and I_0 is the peak intensity

$$I_0 = \left(\frac{\pi D^2}{4\lambda d}\right)^2 I_\mathrm{i} \tag{2.38}$$

The radius of the central disk of the Airy pattern obtained is:

$$\rho_\mathrm{s} = 1.22\frac{\lambda d}{D} \tag{2.39}$$

If the beam is focus by a microlens of focal distance f, the radius of the spot becomes:

$$\rho_\mathrm{s} = 1.22\frac{\lambda f}{D} \tag{2.40}$$

What are aberrations?

Aberrations are typically more important than diffraction [113]. They come from the deviation of the shape of the lens from the ideal profile. Main aberrations are listed below:

- Spherical aberrations
- Coma
- Astigmatism
- Defocusing
- Tilt and shifts about x- or y-axis
- etc

The consequence of all theses aberrations is a loss of light.

2.4.4 Angle of acceptance of optical fibers

Optical fibers can be of two types:

- Step index fibers
- Graded index fibers

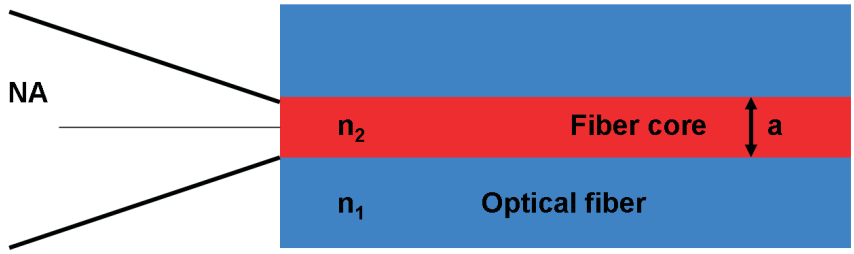

Figure 2.16: *Schematic view of a step index optical fiber and its numerical aperture NA.*

For both types, the working principle is the same. The light is guided into the fiber by internal reflections due to a variation of the refractive index n. In step index fibers, the index variation is localized at a certain radius and the core diameter is precisely delimited. For graded index fibers, the refractive index is maximal along the central axis of the fiber and decreases gradually across the fiber. Its major advantage is that modal dispersion is reduced because the speed of the light increases with the distance to the center of the fiber. Thus, the light that travels on a longer distance goes faster. That way, the travel times are equalized.

A single mode fiber is a standard fiber with a core of reduced dimension. A fiber operates as single mode in the fundamental mode if the V parameter is smaller than:

$$V = 2\pi \frac{a}{\lambda_0} NA < 2.405 \text{ [127]} \tag{2.41}$$

$$NA = \sqrt{n_1^2 - n_2^2} \tag{2.42}$$

where a is the diameter of the fiber core, λ_0 is the wavelength and NA is the numerical aperture of the fiber (Figure 2.16).

2.5 Veeco/Wyko NT1100 optical profiler

The Wyko DMEMS 1100 white light interferometer is a characterization tool allowing to do measurements of vertical steps, displacements and roughness, as well as lateral displacement using a pattern recognition algorithm.

Depending on the device to be characterized, different measurement modes can be used. Their vertical resolutions are shown in table 2.3. The first one, based on monochromatic light, is called the PSI (Phase-Shifting Interferom-

	Vertical Resolution	
Mode	Single Measurement	Multiple Measurements (Averaged)
PSI	3 Å	1 Å
VSI	3 nm	<1 nm

Table 2.3: *Vertical resolution of PSI and VSI modes [4].*

etry) mode. It allows a very high vertical resolution down to the Angstrom scale but cannot determine the height of vertical steps.

The second working mode, called VSI (Vertical Scanning Interferometry), is based on white light interferometry. It allows to measure large displacements and steps up to several millimeters with a theoretical precision of less than two hundredths of the measured height.

The tool looks like a standard microscope with different objectives and fields of views that gives the possibility to observe the sample with various magnifications. Figure 2.17 shows a schematic of the instrument's working principle. The incident light (filtered for the PSI mode) illuminates the sample by passing through the objectives. These have an integrated interferometer. For low magnifications (1.5 to 5 times), the integrated interferometer is of the Fourier type. It is then composed of an incorporated beam splitter and a reference mirror. For higher magnifications (10 times or more), the integrated interferometer is of the Mirau type as shown in figure 2.17.

2.5.1 Phase-Shifting Interferometry (PSI)

In phase-shifting interferometry, a whitelight beam is filtered and passed through an interferometer objective to the test surface. The interferometer beamsplitter reflects half of the incident beam to the reference surface within the interferometer. The beams reflected from the test surface and the reference surface recombine to form interference fringes. These fringes are the alternating light and dark bands you see when the surface is in focus. Figure 2.17 shows a diagram of an interference microscope. During the measurement, a piezoelectric transducer (PZT) linearly moves the reference surface a small, known amount to cause a phase shift between the test and reference beams. The system records the intensity of the resulting interference pattern at many different relative phase shifts, and then converts the intensity to wavefront (phase) data by integrating the intensity data.

The phase data are processed to remove phase ambiguities between adjacent pixels, and the relative surface height can be calculated from the phase

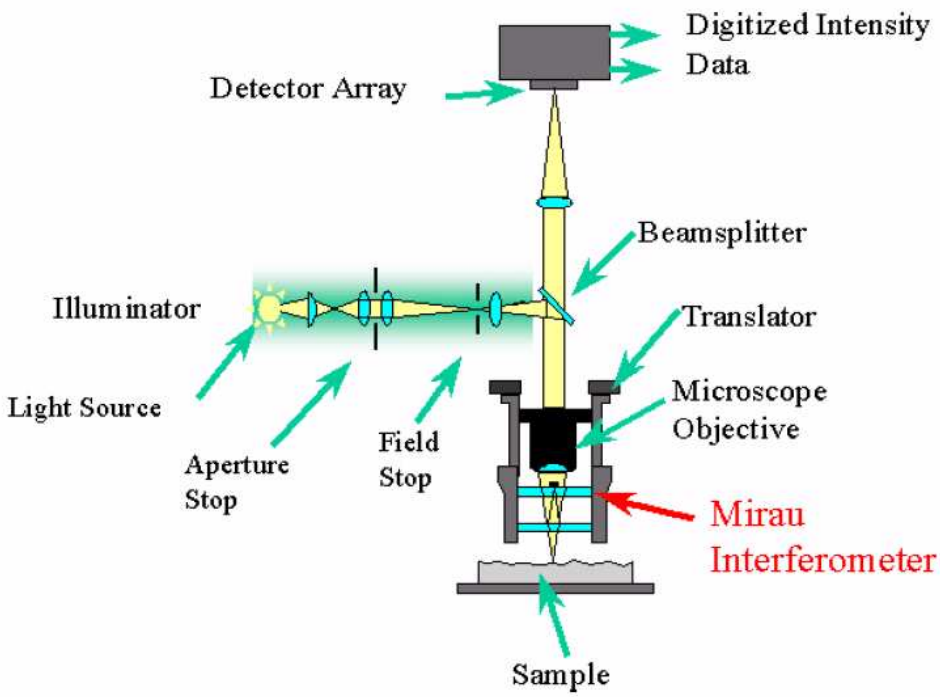

Figure 2.17: *Schematic view of the Wyko 1100 DMEMS [4].*

data as follows:

$$h(x,y) = \frac{\lambda}{4\pi}\phi(x,y) \tag{2.43}$$

where λ is the wavelength of the source beam, and $\phi(x,y)$ is the phase data. This technique for resolving surface heights is reliable when the fringe pattern is sufficiently sampled. When the surface-height difference between adjacent measurement points is greater than $\lambda/4$, height errors in multiples of $\lambda/2$ may be introduced and the wavefront cannot be reliably reconstructed. Thus, conventional phase-shifting interferometry is limited to fairly smooth, continuous surfaces. To resolve rougher surfaces, Wyko surface profilers use vertical-scanning interferometry techniques.

2.5.2 Vertical Scanning Interferometry (VSI)

Wyko developed VSI, a newer technique than PSI. The basic interferometric principles are similar in both techniques: light reflected from a reference mirror combines with light reflected from a sample to produce interference fringes, where the best-contrast fringe occurs at best focus. However, in VSI mode, the white-light source is filtered with a neutral density filter,

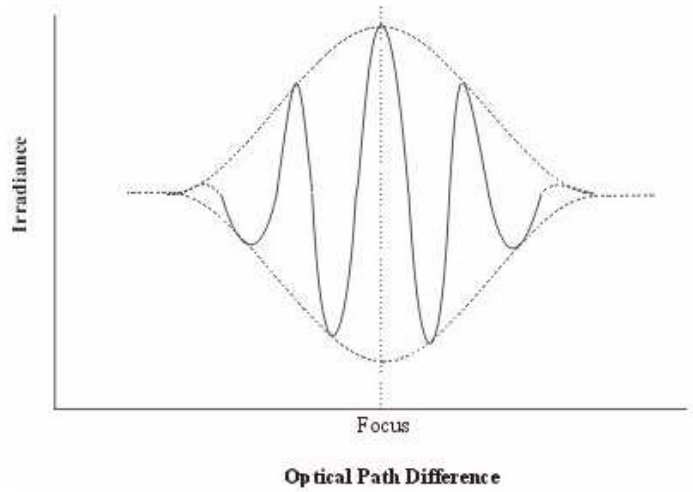

Figure 2.18: *Fringe contrast through focus [4].*

which preserves the short coherence length of the white light, and the system measures the degree of fringe modulation, or coherence, instead of the phase of the interference fringes.

In VSI, the irradiance signal is sampled at fixed intervals as the optical path difference (OPD) is varied by a continuous translation of the vertical axis through focus. By numerical analysis of the obtained signal, the peak of the interferences (Figure 2.18) is located and the vertical position that corresponds to the peak is recorded. To increase the resolution of the measurement beyond the sampling interval, a curve-fitting interpolation technique is used. The interferometric objective moves vertically to scan the surface at varying heights. A motor with feedback from an LVDT (linear variable differential transformer) precisely controls the motion. Because white light has a short coherence length, interference fringes are present only over a very shallow depth for each focus position. Fringe contrast at a single sample point reaches a peak as the sample is translated through focus. As seen in figure 2.18, the fringe contrast, or modulation, increases as the sample is translated into focus, then falls as it is translated past focus.

The system scans through focus (starting above focus) as the camera captures frames of interference data at evenly-spaced intervals. As the system scans downward, an interference signal for each point on the surface is recorded. The system uses a series of advanced computer algorithms to demodulate the envelope of the fringe signal. Finally the vertical position corresponding to the peak of the interference signal is extracted for each pixel

of the image.

The precision of the lateral resolution of these measurements is limited by diffraction of the edges of the structures as detailed in [128, 129].

2.5.3 Pattern recognition

The system includes a pattern recognition module. With this module, it is possible not only to measure vertical steps and displacements but also lateral movements. This is very useful to determine whether a moving device moves only in-plane but also out-of-plane and compare both values. The precision of the position determination depends on several parameters. The most important, the observed area of the sample. The larger the area, the higher is the uncertainty on the obtained results. As the pattern recognition is based on the pixels of the CCD camera, the more pixels are used in the interesting area, the better the measurement. For magnifications of about ten times, for example, the lateral (optical) resolution given is lower than one micron. This resolution also differs in the X and Y direction as the CCD does not has the same pixel size in both axis. By fitting the data, it is possible to obtain a sub-pixel resolution.

The module also allows to mask parts of the image or define interesting areas and store some of their properties in a database. This was used for some of the measurements performed in section 5.2, but was too limited for the full pattern analysis (Section 5.2.6).

2.5.4 DMEMS working mode

To observe the dynamic behavior of a system, the DMEMS (Dynamic MEMS) mode has to be used. In this mode, the illumination is not done by a constant light source but by a stroboscopic illumination. A LED, synchronized with the camera illuminates the moving sample at a frequency corresponding to the actuation signal of the device. As the vertical scan of the machine is not very fast, this stroboscopic illumination allows the system to see only one position of the device. Of course, the movement of the observed sample has to be constant over a large number of cycles. Otherwise, the software cannot determine its position and height.

To analyze the movement of the moving device over a full actuation cycle, the stroboscopic illumination can be performed for each phase shift comprising between 0 and 360°. Then, all these results can be processed to get the dynamic behavior of the observed device over a full cycle. This allows for example to determine the resonance frequency of an actuator by performing

a Fourier transform to the step response signal of the device. This module was used for this purpose in section 5.2.7.

2.6 Stiction

Stiction is a common phenomenon in MEMS devices [130]. It is a combination of one or more "adhesion forces" or "adhesion phenomena" between two objects in contact [131]. In most cases, it is an undesirable effect that limits the performance and the lifetime of MEMS actuators [132].

2.6.1 Adhesion effects in microsystems

This phenomena occurs once two surfaces are brought in contact due to:

- Electrostatic forces;
- Drying process after the HF release of sacrificial layers;
- Shock loading or rapid acceleration that can bring two surfaces together;
- Inadequate stiffness of supporting micro-beams against gravity or normal operation;
- Desired contact by design or actuation.

Once the surfaces are in contact, several stiction phenomena can appear. At the micro-scale, these forces can be comparable or even often greater than other micro-forces.

They are mainly due to the following causes:

- **Meniscus (capillarity) forces effect;** Capillary forces occur when there is a liquid-solid interface. This liquid can be due to condensation of the humidity of the air. The pressure difference between the liquid-air interface is given by the equation:

$$\Delta p_{\mathrm{la}} = \frac{\gamma_{\mathrm{la}}}{r} \tag{2.44}$$

  where Δp_{la} = pressure difference at liquid-air interface, γ_{la} = surface tension of the liquid-air interface and r = radius of curvature of the

meniscus of liquid. The forces between the two plates can then be expressed as:

$$F = -\Delta p_{\mathrm{la}} A = \frac{2A\gamma_{\mathrm{la}} cos(\theta_{\mathrm{c}})}{d} \tag{2.45}$$

where A = area between the two plates, θ_{c} = contact angle between liquid and solid and d = separation distance between plates. In case of two not perfectly flat surfaces, the contact area A and the distance d are a function of the surface roughness. The rougher the surface, the smaller the capillarity force.

- **Hydrogen bridging:** Hydrophilic surfaces, under atmospheric conditions and around room temperature contain adsorbed water layers. These materials adsorb water to a small depth below their surface layer. When two of these hydrated surfaces are brought into close contact, hydrogen bonds may form between oxygen and the hydrogen atoms of the adsorbed water layers in each of the surfaces. This is a chemical bond that will remain as long as the surfaces are hydrated.

- **Electrostatic forces:** In electrostatic driven MEMS, contact between polarized electrodes has to be avoided. When two electrodes with different applied voltages are brought in contact, a current is created at the interface. If this current is not limited enough, the electrodes stay in contact even if the applied voltage is set back to zero due to a modification of the surface at the interface.

- **Van de Waals forces:** They are caused by mutual electric interaction of the induced dipoles in the two surfaces.

Several solutions exists to avoid or minimize stiction. In some case, a thin protective layer is deposited on the surface that have to get in contact [133, 134]. Another solution is to avoid any contact between surfaces. When this is not possible, stoppers are generally used. They are made of a small bump or tip meant to get in contact. In this case, the smaller the contact surface, the smaller the stiction force. For this reason these have usually a very small contact surface [135].

2.6.2 Locking

Stiction effects can also be utilized. It is used for example to perform silicon-silicon direct bonding [136]. It is also possible to use it to create a relatively

tight connection between two initially independently moving parts. Experiments on this phenomenon will be presented in section 5.3. The deliberate stiction between a movable platform and the handle part of a silicon device will be presented.

2.7 Precision and accuracy

In chapter 5, measurements on the displacement of the actuator will be presented. To clarify the exposed results, the terms of "precision" and "accuracy" are explained below.

2.7.1 Precision of the actuator motion

The term precision is principally applied to the measurement of the displacement of the actuator. If a mobile structure moves from a point A to a point B separated by a distance d, the precision of the measurement denotes how the measured distance is determined compared to the effective value.

2.7.2 Accuracy of the actuator motion

The term accuracy shows the repeatability of the displacement of the actuator. By moving the actuator with a certain signal from a point A twice, the actuator will reach a point B the first time and a point B' the second time. The accuracy is determined by the difference between the position of the points B and B'.

Chapter 3

Micro scanner concept (MOPOS project)

3.1 Description of the system

As seen in chapter 1, the goal of the MOPOS project was to develop a micro-scanner to optimize the light coupling between a laser diode and an optical fibre. This section will describe in details the system to be solved.

The initial requirements at the beginning of the project were the following:

- Optical specifications:
  - Laser diode:
    - NA: 0.5
    - Wavelength: 1290 - 1580 nm
    - Reflective feedback: $\leq$60 dB
  - Lens:
    - Magnification: 4-5 times
    - Anti-reflective coating: $<$25 %
    - Coupling efficiency: 60 % ($>$30 %)
    - Outer diameter: 0.6-0.8 mm
  - Fiber:
    - Single mode (SMF28)
- Mechanical specifications:
  - Chip size:
    - In x direction: $<$2500 μm
    - In y direction: $<$2000 μm

  - Lens travel:
    - X range: $\pm 15\,\mu$m
    - Y range: $\pm 30\,\mu$m
    - Resolution: 20 nm
    - Accuracy: 50 nm
    - Locking accuracy: 100 nm

- Electrical specifications:

  - Input signals
    - X position control voltage: ± 10 V
    - Y position control voltage: ± 10 V
    - X and Y locking voltage

- Reliability specifications:

  - MOEMS assembly Telecordia requirements:
    - 500 cycles -40 to 85 °C
    - 5000 hours of aging 75 °C
    - Shock: 1500 G - 0.5 ms (duration)
    - Vibration: 2 to 2000 Hz - 20 G
    - Tracking: 0 °C to 50 °C
    - 2000 hours at high temperature storage 85 °C
    - 2000 hours at low temperature storage -40 °C

- Pass criteria: lens displacement $<0.05\,\mu$m
  or coupling efficiency change $< 10\%$

- Locking of the platform in desired position

Additionally, the technology and the process had to be as simple as possible in order to get a device as cheap as possible (typ. a few dollars or preferably less!).

Based on the calculated optical configuration, a MEMS concept has to be developed. This will be further explained in the following subsections.

3.1.1 Optical configuration

Instead of using passive alignment devices or large and expensive welding stations to precisely align optical components, the principle studied is to roughly align the laser diode, the optical fiber, and in between, a focusing lens mounted on a 2D actuator that can steer the light to optimize the coupling

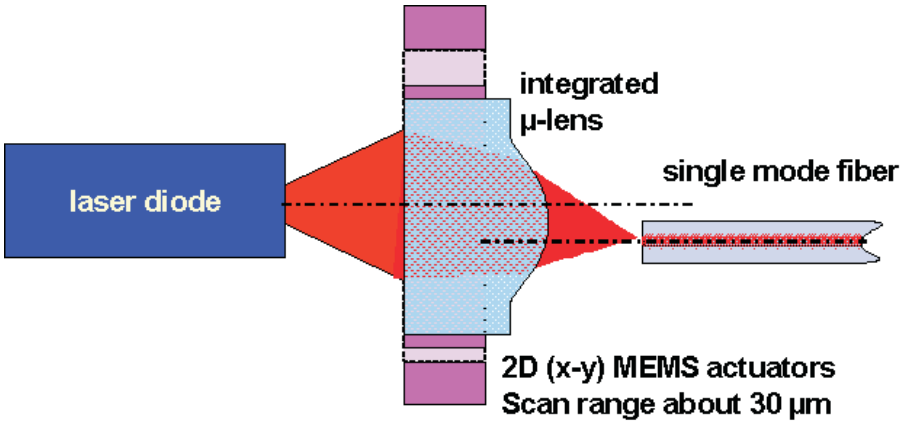

Figure 3.1: *Schematic of the concept of the system: a movable lens compensate the initial misalignment of the roughly aligned optical components.*

once all the components are assembled. Figure 3.1 shows the concept of the system.

Optical simulations were performed to determine the best optical configuration of the system.

Optical simulations

Standard laser-fiber coupling devices use two lenses. The first collimates the light and the second one focuses the light beam into the optical fiber. In this project, the goal was to use only one lens in the optical path between the laser and the fiber. Simulations were performed to find the optimal shape and position of the lens as well as the corresponding distances between the laser and the lens and between the lens and the optical fiber. The optical simulations were performed with the software called "FRED" (from Photon Engineering) and a matlab routine allowed them to be automatized. Figure 3.2 shows the simulated configuration.

After some simulations and economy considerations, it was chosen to use lenses directly available from Süss MicroOptics's web shop. A new lens development was too complicated and time consuming for this project. The lens that reaches the best the requirements has a diameter of 500 μm, a radius of curvature of 900 μm and a K factor of -9. Figure 3.3 shows the coupling efficiency of such a lens in function of the distance between the laser diode to the lens bottom and the distance between the lens top to the fiber end. It shows a maximal coupling efficiency of more than 80%. It would be possible to obtain higher coupling efficiencies with larger lenses. Moreover, the platform, with its 600 μm diameter hole was foreseen to receive a larger

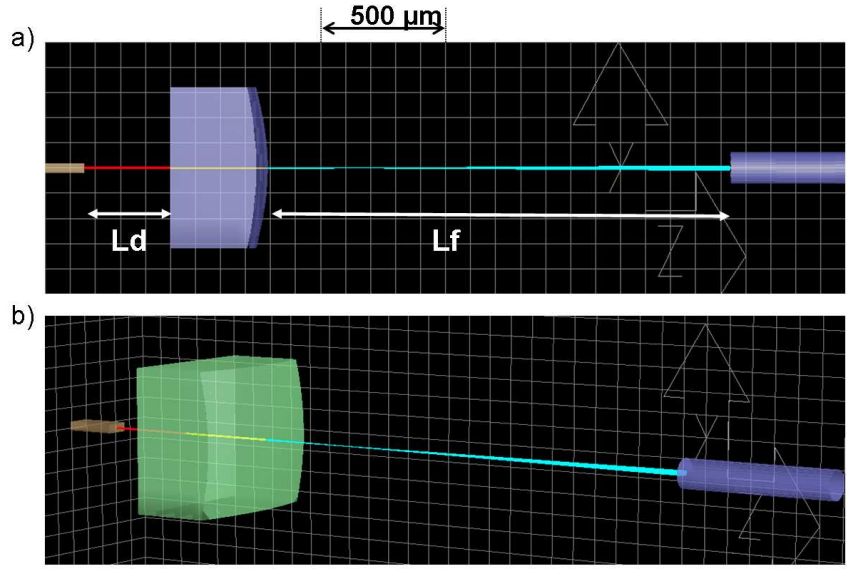

Figure 3.2: *"FRED" images of the simulated system.*

lens but no lens of this size was available.

As the MOPOS device is studied to compensate only the misalignment perpendicular to the optical axis, it is important to set the distances in a region where the coupling losses due to the misalignment of the components along the optical axis can be minimized. The goal is then to find a region where the gradient is minimum or a large region where the coupling is above a certain value. Figures 3.4 and 3.5 show the value of the coupling efficiency up to 40%. This value of 40% was chosen in order to be higher than the minimal value given in the initial specifications and low enough in order to get a large enough area.

With the following data and properties,

- Laser diode
  - Wavelength: $lambda = 1.31\,\mu$m
  - Beam waists: $w_x = 1.806\,\mu$m, $w_y = 0.618\,\mu$m, elliptical beam with $NA_{max} = 0.5$ along Y axis.
  - Source diameter: $d_x = 9\,\mu$m, $d_y = 6\,\mu$m
- Lens
  - Distance: $LD = 355\,\mu$m

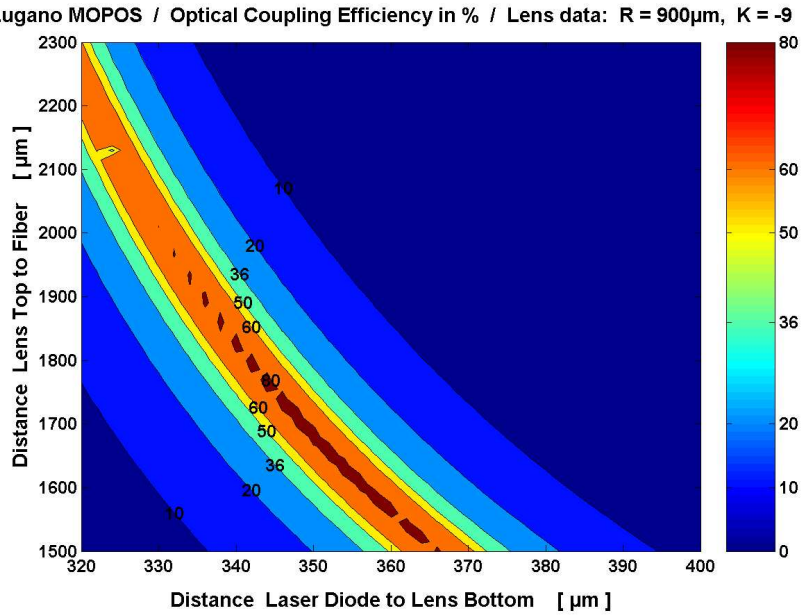

Figure 3.3: *Graph showing the simulated coupling efficiency as a function of the distance between the laser diode to the lens bottom (Ld on figure 3.2(a)) as well as the distance between the lens top to the fiber end (Lf on figure 3.2(a)). The simulated lens has a radius of curvature of 900 µm and a K factor of -9 assuming a perfect perpendicular alignment.*

  - Edge length: $L = 640\,\mu\text{m}$
  - Lens thickness: $T_{\text{lens}} = 500\,\mu\text{m}$
  - First surface: flat
  - Second surface: $R_{\text{curv}} = -900\,\mu\text{m}, K = -9$
  - Material: Silicon, $n_{\text{Si}} = 3.505$[117], at $\lambda = 1.31\,\mu\text{m}$

- Fiber
  - Corning SMF-28 @ $1.31\,\mu\text{m}$
  - Distance from lens second surface: $z_1 = 1850\,\mu\text{m}$
  - Fiber core diameter: $8.2\,\mu\text{m}$
  - Numerical aperture: 0.14

one obtain the beam shape shown in figure 3.6.

As shown in the previous graphs (figure 3.3-3.5), the overall coupling is not very high but, as the goal of the project is to obtain a high coupling

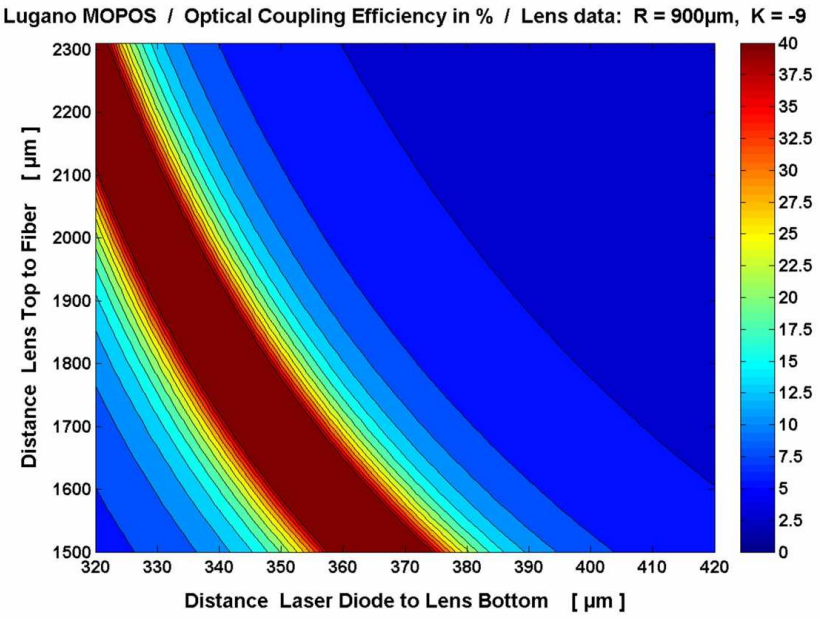

Figure 3.4: *Graph showing the simulated coupling efficiency as a function of the distance between the laser diode to the lens bottom (Ld on figure 3.2(a)) as well as the distance between the lens top to the fiber end (Lf on figure 3.2(a)). The simulated lens has a radius of curvature of 900 µm and a K factor of -9 with a scale limit set to 40%.*

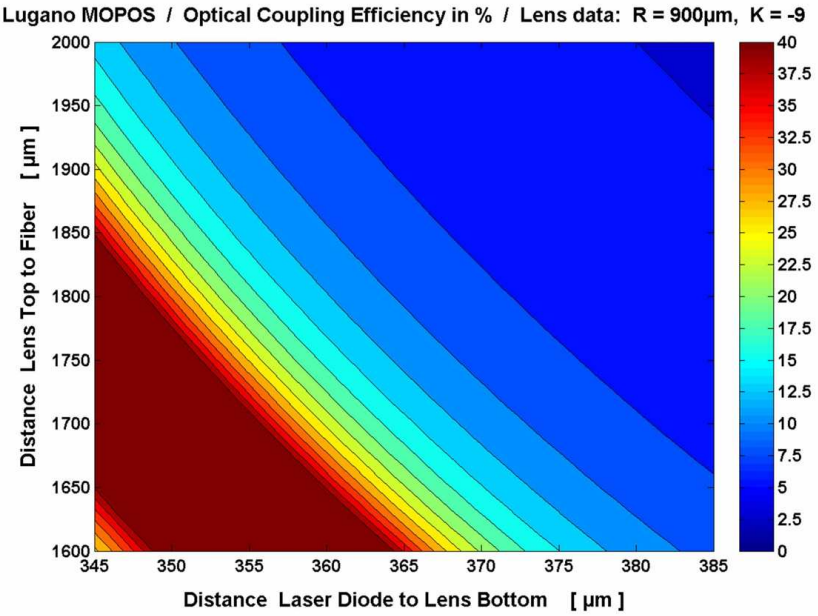

Figure 3.5: *Zoom on the graph of figure 3.4 showing the simulated coupling efficiency as a function of the distance between the laser diode to the lens bottom (Ld on figure 3.2(a)) as well as the distance between the lens top to the fiber end (Lf on figure 3.2(a)). The simulated lens has a radius of curvature of 900 µm and a K factor of -9 with a scale limit set to 40%.*

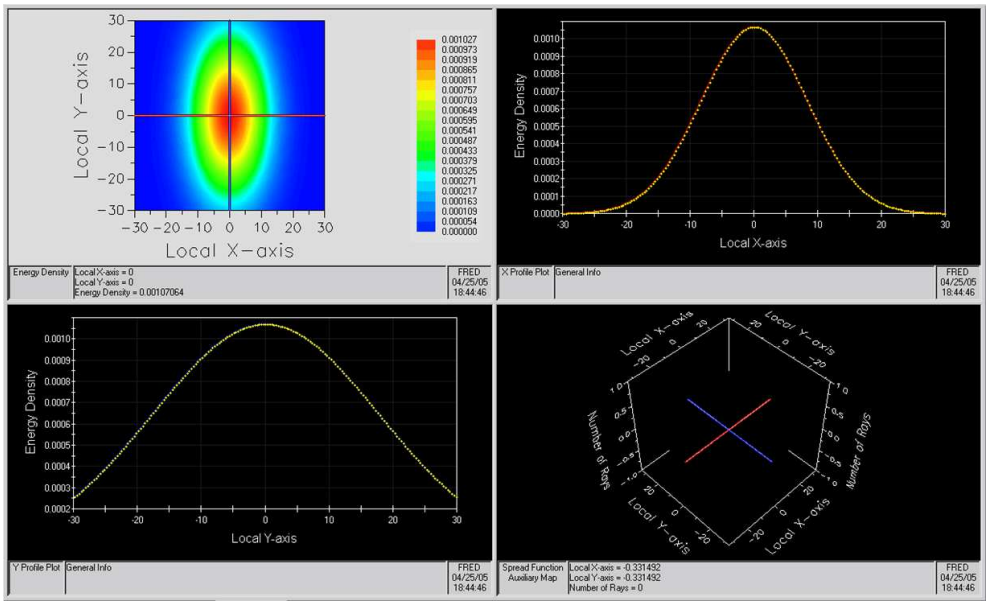

Figure 3.6: *Simulated beam shape in fiber interface.*

efficiency over a position range along the optical axis of several microns, these results are suitable for the intended application.

With these values, the focal distance of the lens can be estimated [113]:

$$f = \frac{R_{\text{curv}}}{n_{\text{Si}} - 1} = 360.36\,\mu\text{m} \tag{3.1}$$

With the focal distance and an initial laser to lens distance of $355\,\mu$m, the effective magnification M of the lens is the following:

$$M = \frac{f}{f - D} = \frac{f}{f - (355 + 500/3.4975)} = 3.71 \tag{3.2}$$

where D is the optical distance between the silicon lens (thin lens) and the laser diode. These calculations were performed with a thin lens approximation.

A factor of about four is the expected result as the numerical aperture of the laser diode is about four times larger than the one of the optical fiber.

From this point, it is possible to calculate the required displacement of the lens for a given misalignment of the laser diode (or the optical fiber).

Considering the system shown in figure 3.7, if the diode is misaligned of a distance h_{d} perpendicular to the optical axis, the required x displacement of the lens is given by:

$$x = \frac{M}{M+1} h_{\text{d}} = \frac{3.71}{4.71} h_{\text{d}} = 0.79 h_{\text{d}} \tag{3.3}$$

This means that to balance the misalignment h_{d} of the diode, the lens has to be displaced of $0.79 h_{\text{d}}$. Thus, for a misalignment of $10\,\mu$m, the required movement of the diode is of about $7.9\,\mu$m.

In the other side, if the optical fiber is misaligned of a distance h_{f}, the required x displacement of the lens is determined by:

$$x = \frac{h_{\text{f}}}{M+1} = \frac{1}{4.71} h_{\text{f}} = 0.21 h_{\text{f}} \tag{3.4}$$

For example, for a misalignment of the fiber of $10\,\mu$m, the required movement of the diode is of about $2.1\,\mu$m.

In the worst case, if both the diode and the fiber are misaligned in the same direction, the required displacement of the lens is of the same amplitude.

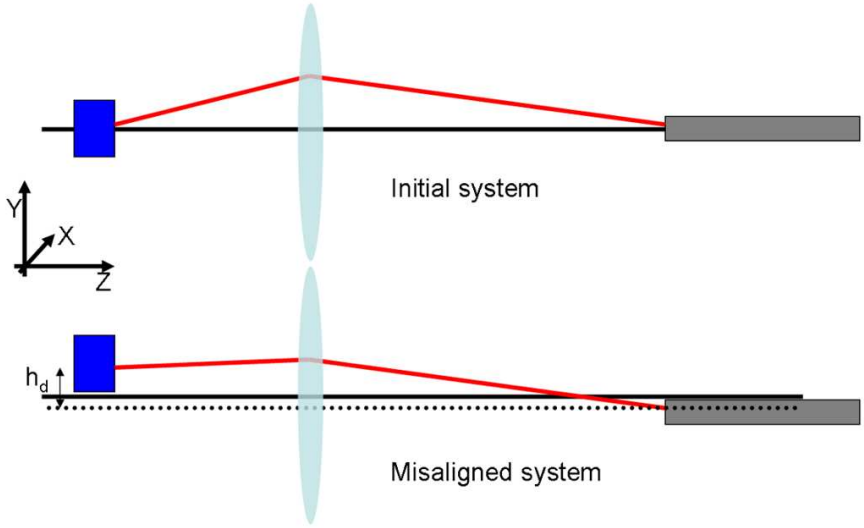

Figure 3.7: *Schematic of the misalignment of the laser diode.*

3.1.2 MEMS Concept

To reach the specifications listed at the beginning of this chapter in terms of displacement, size and voltages, a new MEMS device had to be imagined. The initial question is represented in figure 3.8. The initial constraints being fixed, a system able to move a microlens with any type of actuator and suspensions had to be developed.

Initial simulations and calculations performed to compare different design concepts are summarized in table 3.1.

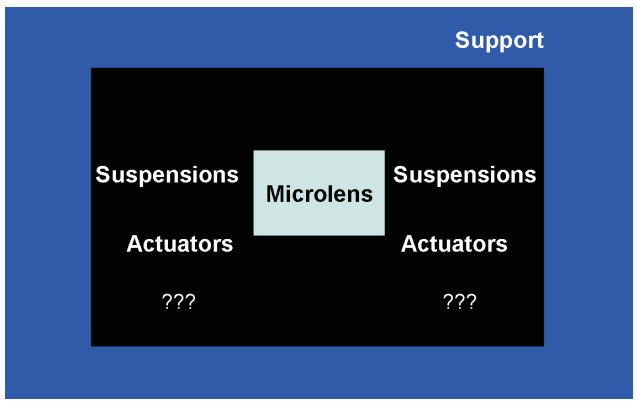

Figure 3.8: *Initial reflexion model. What to put in the black box?*

N°	**Schematic of the imagined system**	**Driving method**	**Relative force over voltage**	**Conclusion**
1.a)	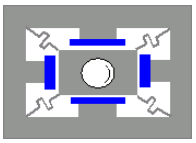	Electrostatic, parallel plates	Low	Not suitable (high voltage, controlled displacement on only 1/3 of initial gap).
1.b)	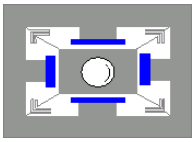	Electrostatic, parallel plates	Low	Not suitable (high voltage, controlled displacement on only 1/3 of initial gap).
1.c)	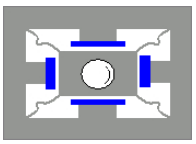	Electrostatic, parallel plates	Low	Not suitable (springs too strong).
1.d)	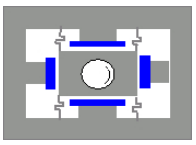	Electrostatic, parallel plates	Low	Not suitable (high voltage, controlled displacement on only 1/3 of initial gap). Good solution for displacement in 1 direction only.
2)		Electrostatic, parallel plates	Low	Not suitable (high voltage, controlled displacement on only 1/3 of initial gap). Good solution for springs perpendicular to displacement direction.

continued on next page

continued from previous page				
3.a)	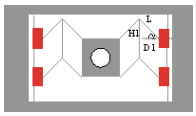	Electrostatic, Comb drives	High	Not suitable (lack of stability, low displacement in Y direction).
3.b)	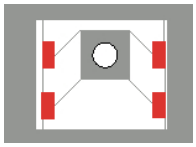	Electrostatic, Comb drives	High	Suitable but compliant beams highly stressed.
3.c)	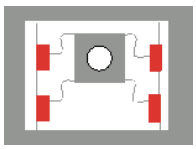	Electrostatic, Comb drives	High	Suitable. Shape of the curved compliant beams to be optimized.

Table 3.1: *Table representing the initial calculated and simulated structures. The central white circle represents the microlens. The blue rectangles represent the electrodes of parallel plate electrodes actuation. The red rectangles represent the electrostatic comb drives actuators.*

Following the results of table 3.1, the design 3.c) consisting of two pairs of linear actuators and curved beam to convert linear actuation into a 2D motion was chosen. It allows a sufficiently large controlled displacement at relatively low voltages in a quite compact design.

The actuator, shown in figure 3.9, consists of 3 major elements.

The first is the scanning platform, designed to hold a lens on its top.

The second is a system of curved compliant suspension beams. The curved shape is designed to convert a unidirectional actuation into a bi-directional displacement.

The third element comprises comb-drive actuators and springs attaching the movable structure to the fixed parts of the chip.

The principle of operation of the MEMS scanner is shown in figure 3.10. The 2D displacement of the hollowed platform of the device is provided by two pairs of electrostatic combdrive actuators (driven by the electrodes A, B, C and D, Figure 3.9) suspended by 4 springs to the chip base [137]. The mobile platform is linked to the actuators by 4 curved compliant suspension

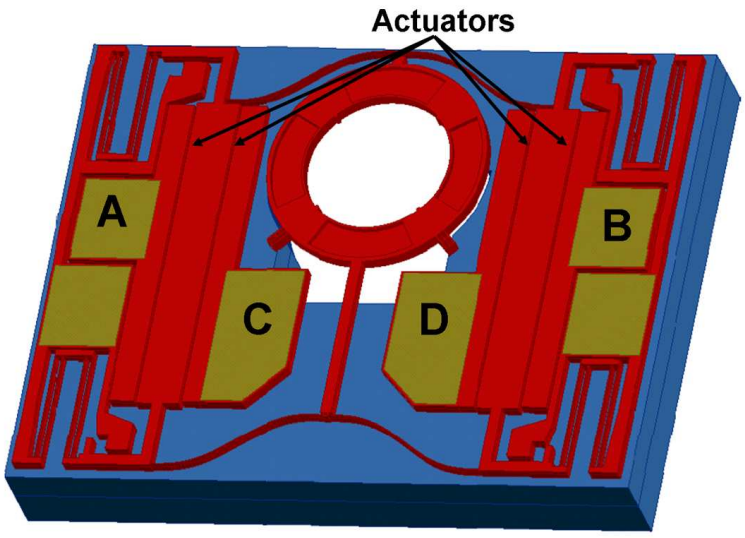

Figure 3.9: *CAD image of the device showing the two pairs of electrostatic combdrive actuators, the compliant suspension springs and the movable platform. To limit the computer resources required, the combdrives actuators pairs are represented by three large rectangles instead of showing all the fingers. The chip footprint size is 2064x2700 μm, slightly larger than in the initial specification requirements but the construction of the last packaging system allows such dimensions.*

Elec A	Elec B	Elec C	Elec D	Platform displacement direction
+V	**0** V	**0** V	**0** V	↙
0 V	+V	**0** V	**0** V	↘
0 V	**0** V	+V	**0** V	↗
0 V	**0** V	**0** V	+V	↖
+V	**0** V	**0** V	+V	←
+V	+V	**0** V	**0** V	↓
0 V	**0** V	+V	+V	↑
0 V	+V	+V	**0** V	→

Table 3.2: *Displacement of the platform depending on the polarized actuators. This table is shown for only one voltage +V applied without any voltage on the other electrodes but is also valid for any signal combination as long as +V is larger than any other voltage applied.*

beams. These flexible s-shaped beams are designed to convert two unidirectional (X) actuations into two dimensional (XY) displacements and as well as to amplify the movement in the direction orthogonal to the actuators by a factor of two (Section 3.4). When the two actuators are moving in the same direction and amount, the platform translates in the same orientation and by the same distance (displacement in X). Additionally when the two actuators are moving in opposite directions by the same amount, the platform translates in the orthogonal direction by either compressing or extending the compliant beams (displacement in Y). Figure 3.10 show the displacements along the two main axes (X) and (Y). With combining these basic displacements by applying different signal amplitudes to combdrive actuators, any off-axis points of the reachable area (Section. 5.2) can be addressed. All these displacements are summarized in table 3.2.

Once the desired position is reached, the movable platform can be locked in place. The initial idea is to perform this locking by applying a voltage between the movable platform and the base of the chip (Figure 3.11).

As the light has to be transmitted through, the backside of the chip includes a through hole under the platform to accommodate the movable lens and transmit light across the MEMS chip.

3.1.3 Packaging Concept

During the project, several assembly schemes have been imagined and studied. Initially, the device was supposed to be assembled into a TO can -a

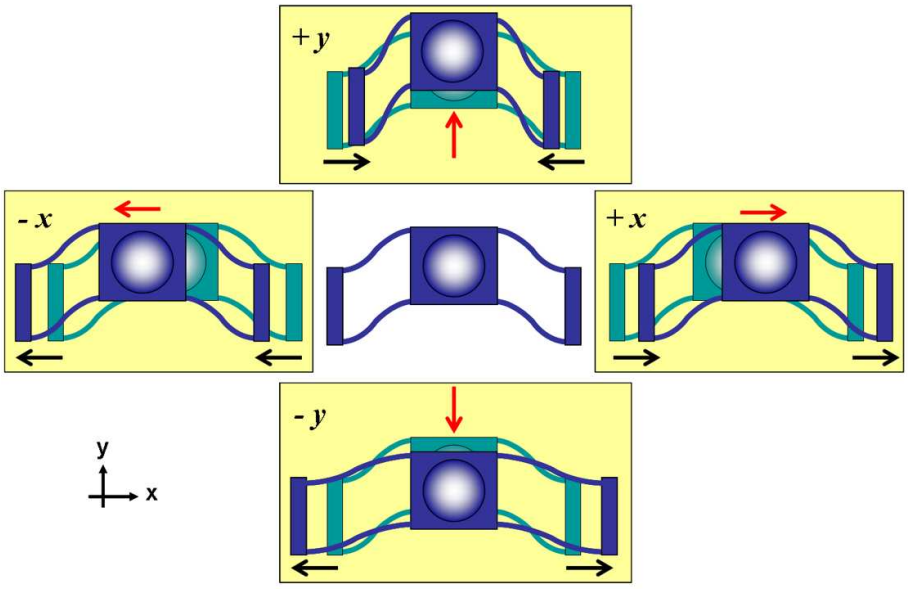

Figure 3.10: *Principle of operation of the MEMS scanner. This figure shows the four fundamentals displacement directions. Starting from these, any displacement within a defined area can be achieved by combining these four displacements.*

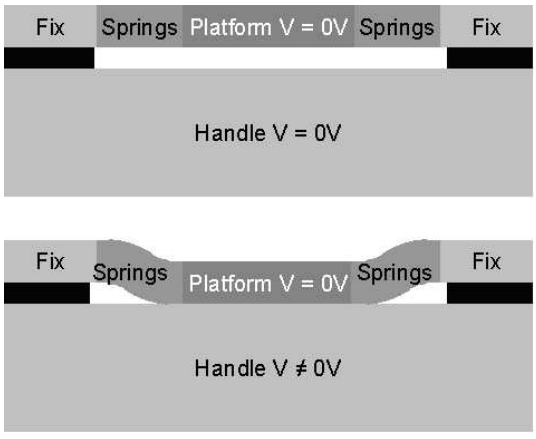

Figure 3.11: *Locking mechanism principle.*

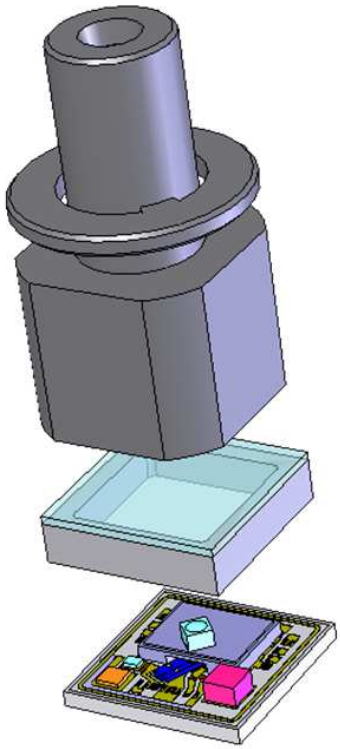

Figure 3.12: *View of the complete system and its components.*

standard packaging solution for this type of devices- but finally, it turned to a vertical silicon packaging [138]. This system is shown in figure 3.12. Figure 3.13 shows a cross section of the complete system. It is composed of a silicon base destined to get all the optical and electrical parts to be connected to. First, the laser diode, the turning mirror and other electronics components (Thermistor, ...) are assembled onto and the MEMS device is glued on top of the turning mirror and the LED and wire bonded on the corresponding metal pads (Figure 3.14).

Once the MEMS device with its assembled lens is connected on the silicon base, a glass lid is sealed to encapsulate all these components. The obtained device is then bonded by flip chip on a flex. The contacts on the flex are shown on figure 3.15. The contact on the bottom of the image are dedicated for connecting the electronic components while the chip is assembled on the top part. Finally, the optical fiber can be connected to the obtained module.

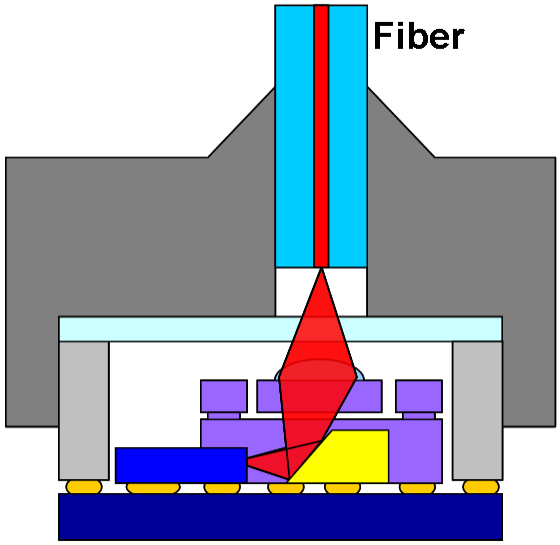

Figure 3.13: *Cross section of the final desired system.*

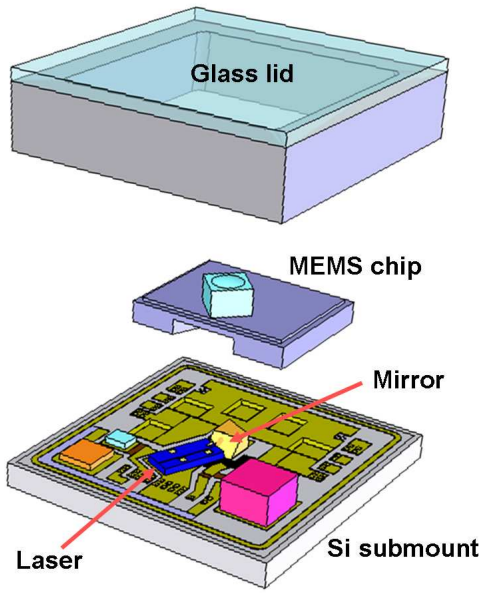

Figure 3.14: *Zoom on the chip assembly concept with its glass lid and the silicon submount containing a laser diode and a turning mirror.*

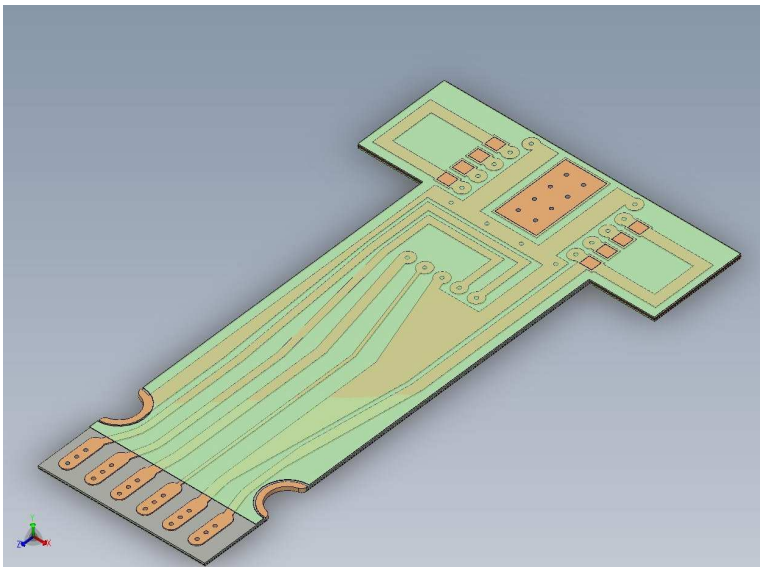

Figure 3.15: *CAD image of the flex. The contacts of the MEMS are located under the silicon device while the contacts for electrical devices are located at its free end.*

3.2 Design of each component

Depending on optical and packaging configurations, the design has to be adapted. In this chapter, the latest design of the MEMS based on the silicon header packaging system developed at Intel (Section 3.1) will be presented.

Several iterations have been made to obtain this design. Figure 3.16 shows a 3D drawing of the chip and figure 3.17 shows cross-sections of the device. Below is a list of the major constrains encountered. They will be explained in a more detailed way in the next subsections:

1. Two etching depths on front- and backside of the chip to obtain complex 3D structures (Section 3.2.1).
2. Metalization on both chip sides (Section 3.2.2).
3. Circular platform with four small alignment structures for lens assembly (Section 3.2.3).
4. Usage of an assembly tool to hold the chip during the lens assembly (Section 3.2.4).
5. Larger backside hole enabling the chip to be held in the assembly tool (Section 3.2.5).

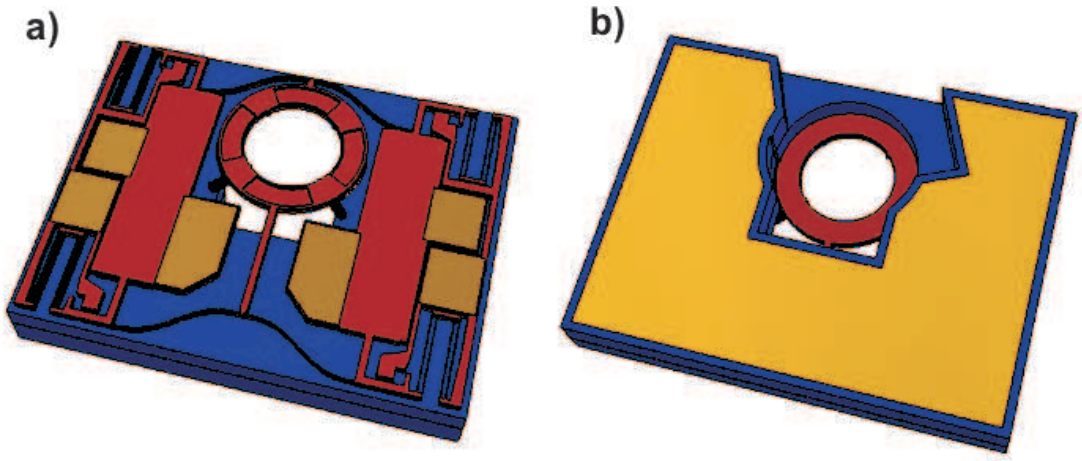

Figure 3.16: *3D CAD image of the chip. a) Topside view. b) Backside view.*

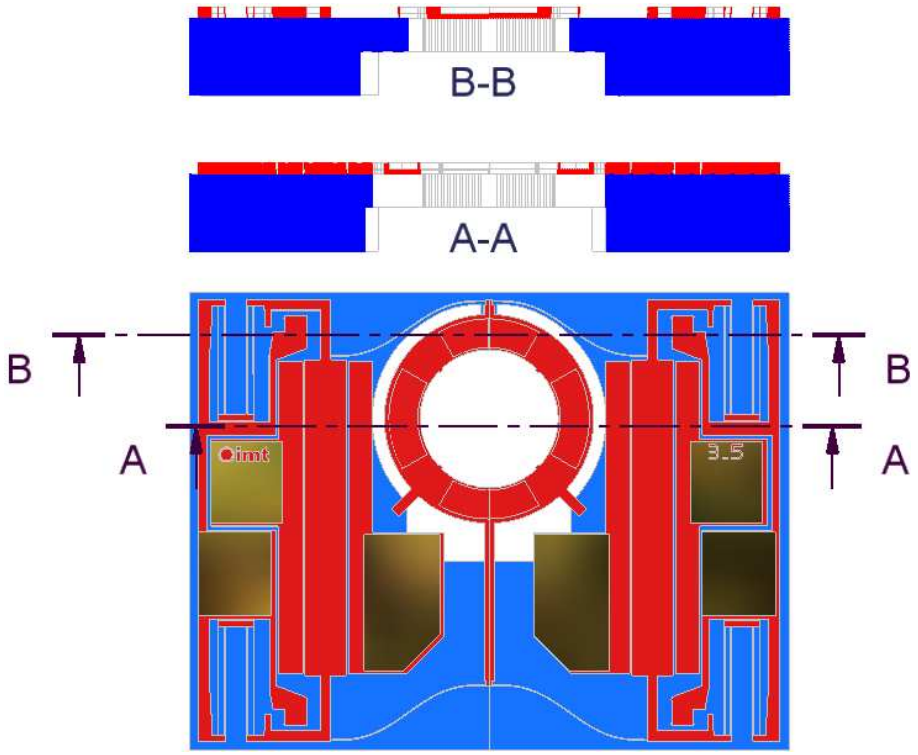

Figure 3.17: *CAD image of the designed chip with cross-sections showing the different etching depths.*

3.2.1 3D etching

Many efforts were been made at the packaging level [138]. This new packaging system includes the chip with an assembled lens as well as a 45° turning mirror and a laser diode placed under the chip in an etched cavity on the backside.

For this reason two masks have been drawn for the frontside etching and two others for backside openings. To define these structures, a process with delay mask etching on both sides was developed. In order to minimize misalignment problems, only the parts to be etched during the second etch step have been defined on the first masks. This method yields an auto-alignment of the masks for the two etching steps.

3.2.2 Front- and backside metalizations

In order to have good electrical contacts and a low resistivity at the interface between the chip and the wire bonds, both sides of the chip must be metalized with gold. This metal is commonly used to provide a good adhesion of the wirebonds on the contacts of the chip. As it is not possible to do the metalization after the DRIE etching, it has to be done at the beginning of the process. Unfortunately, presence of metal -and especially gold- has to be avoided inside the chamber of the DRIE machine and a protective layer has to be deposited on the metal pads. Another masks have been drawn to pattern this metal protection. In order to avoid any contamination risks, the protection pads have been drawn with exactly the same shape than the metal pads but a little bit larger. On topside, the rim defined is 5 μm wide while on the backside of the wafer, the protections were enlarged by 25 μm.

3.2.3 Circular platform

As the lens has a circular shape and in order to save space to be able to place the platform a little bit more off-center on the chip while being closer to the laser diode, the moving frame was designed circular. The size of its inner part has also been enlarged and four small alignment structures have been placed on the four cardinals of the circle. Figure 3.18 shows the platform with its alignment structures and the gluing grooves. The latter are the blue structures shown in figure 3.18, enabling the glue to hold the microlens in place with allowing a zero-gap between the frame of the platform and the lens.

The lens intended to be assembled on the device is processed on both sides. On topside, the lens is etched and on backside, an alignment structure

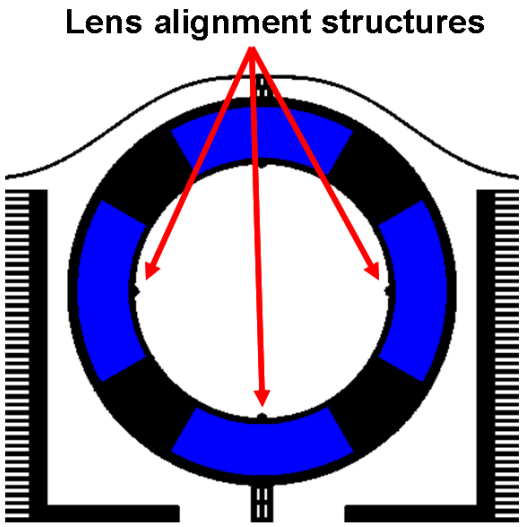

Figure 3.18: *Design of the circular platform with the small lens assembly structures.*

of 25 μm height with inclined sidewalls to about 70° is performed. The latter structure is made in order to facilitate the alignment and assembly of the lens on top of the MEMS platform. Figure 3.19 shows a schematic of the lens to MEMS assembly principle.

3.2.4 Assembly tool

Concerning the assembly of the lens on top of the moving frame, a solution to avoid breakage of the platform had to be studied. The best solution found was either to make a backside hole much smaller than the frame or to use

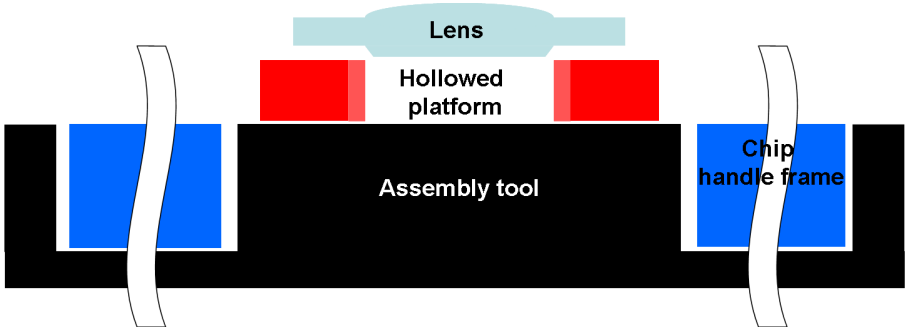

Figure 3.19: *Schematic of the lens to MEMS assembly.*

an external holder to keep the platform in place during glue dispensing. The latter solution was chosen. Figure 3.19 shows the fabricated tool principle. It consists of a large cavity with a central island. As the chip is placed into the cavity, the movable platform gets in contact with the central island of the assembly tool. That way, even if a relatively large force is applied on the frame, there are no constraints on the thin and fragile curved beams of the actuator.

3.2.5 Backside hole

As seen in section 3.2.4, the island of the assembly tool is designed to enter the backside cavity of the chip. Both were designed with related dimensions. Figure 3.16 shows that the backside cavity is much larger than the central hole of the platform. If the only problem was optical transmission of the light, it would have been enough to etch through the backside a hole with dimensions a little bit larger than the platform opening. As the assembly tool cavity is slightly deeper than the backside chip height, the hole has been enlarged in order to allow the assembly tools' central island to come in contact with a fixed part of the device layer of the chip. For this reason the etched hole comes under the fixed central pads of the actuator. That way, once the chip is placed into the assembly tool, it does not lay at the bottom of the cavity but is stopped by the central electrodes on top of the central island of the assembly tool.

3.3 Theoretical model of the system

In this section, a physical model of the device is built in order to predict the position of the platform and the two linear actuators as a function of the electrostatic force applied to the combs. The device can be represented as a system of three springs which are connected to the combdrives as shown in figure 3.20. In this model, only the horizontal component of the spring constant vector is taken in consideration. The reason of this simplification is that the displacement of the platform in the two dimensions depends only on the compliance of the springs along the x axis. Springs S_1 and S_2 correspond to the suspension of the combdrives to the fixed parts of the device while the spring S_3 correspond to the S-shaped beams connecting the combdrives to the movable platform. As no force is applied on the platform (except the gravity, which can be neglected), the two pairs of curved springs can be approximated as one spring.

As the spring constant of S_1 and S_2 are the same, their spring constant is

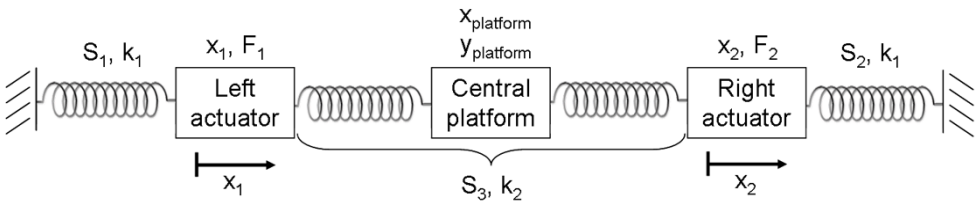

Figure 3.20: *Schematic of the theoretical model of the springs system.*

represented with the unique value k_1. The spring constant of the compliant beams in the x direction is given by k_2. Equations 3.5 and 3.6 establish the relations between the spring constants k_1 and k_2, the forces F_1 and F_2 provided by the actuators and their positions x_1 and x_2.

In equilibrium:

$$F_1 - k_1 x_1 + k_2(x_2 - x_1) = 0 \tag{3.5}$$

$$F_2 - k_1 x_2 + k_2(x_2 - x_1) = 0 \tag{3.6}$$

gives the actuator's displacements:

$$x_1 = F_1\left(\frac{k_1 + k_2}{k_1^2 + 2k_1k_2}\right) + F_2\left(\frac{k_2}{k_1^2 + 2k_1k_2}\right) \tag{3.7}$$

$$x_2 = F_1\left(\frac{k_2}{k_1^2 + 2k_1k_2}\right) + F_2\left(\frac{k_1 + k_2}{k_1^2 + 2k_1k_2}\right) \tag{3.8}$$

The position of the combdrives is a linear combination of the electrostatic forces. This relation will help to determine the spring constants on the device and to predict the position of the movable structure as a function of the voltage applied on the combdrives.

The displacement of the platform held by the curved beams can be determined in relation to the position of the actuators. As the platform stays in the middle of the two actuators, its position in the x direction x_{platform} is simply

$$x_{\text{platform}} = \frac{x_1 + x_2}{2} \tag{3.9}$$

The position in the y direction y_{platform} is a function of $(x_2 - x_1)$ in a way determined by the geometry of the curved beams. This function can not easily be expressed analytically. It can be defined by:

$$y_{\text{platform}} = \psi(x_2 - x_1) \tag{3.10}$$

The function ψ can be evaluated numerically using measurement or simulations results.

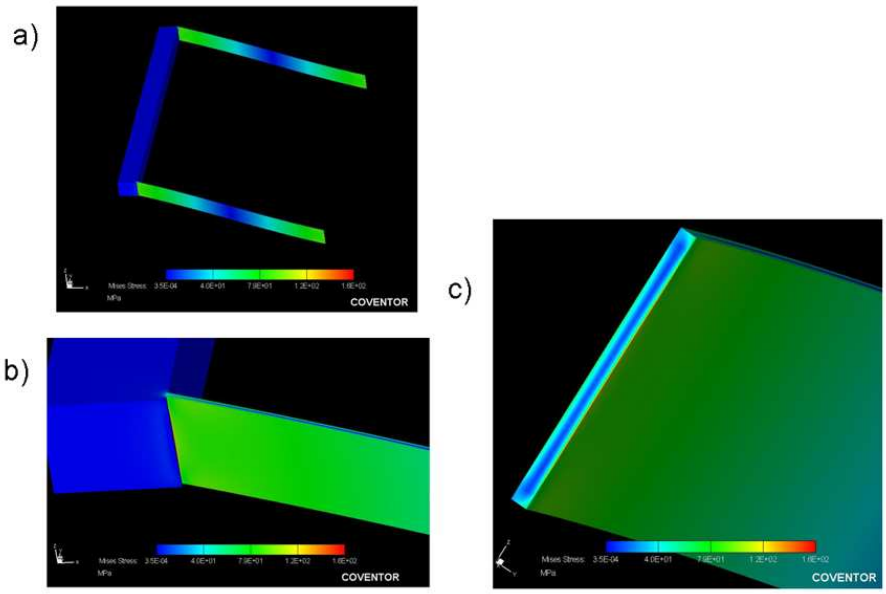

Figure 3.21: *Coventor simulation of the stress in a straight beam as one end is moved in respect to another. A maximal stress of 160* MPa *can be shown.*

3.4 Simulations

Mechanical simulations have been performed to determine the static, quasi-static and dynamic behavior of the device and optimize its components and properties. Then, the results of some of the simulations can be compared to the functions of the theoretical model of the springs system built in section 3.3.

3.4.1 Mechanical simulations

Simulations were done to optimize the size and the shape of the compliant beams. Initial simulations with straight beams showed that the stress at both ends of the beams are very important. It can be seen in figure 3.21 that the stress at beam ends is more important than on curved beams showed in figure 3.22. It can be seen on these figures that for a given deformation, the maximal stress occurs in the same region of the beam but its value is different. In case of a straight beam, a maximal stress of 160 MPa was obtained while the maximal stress of the curved beam was 110 MPa. The curved beam shape allows a reduction of the maximal stress of more than 30%, which is very positive as the stress can be the cause of breakage of the device.

In order to achieve a large enough scanning range in the Y direction

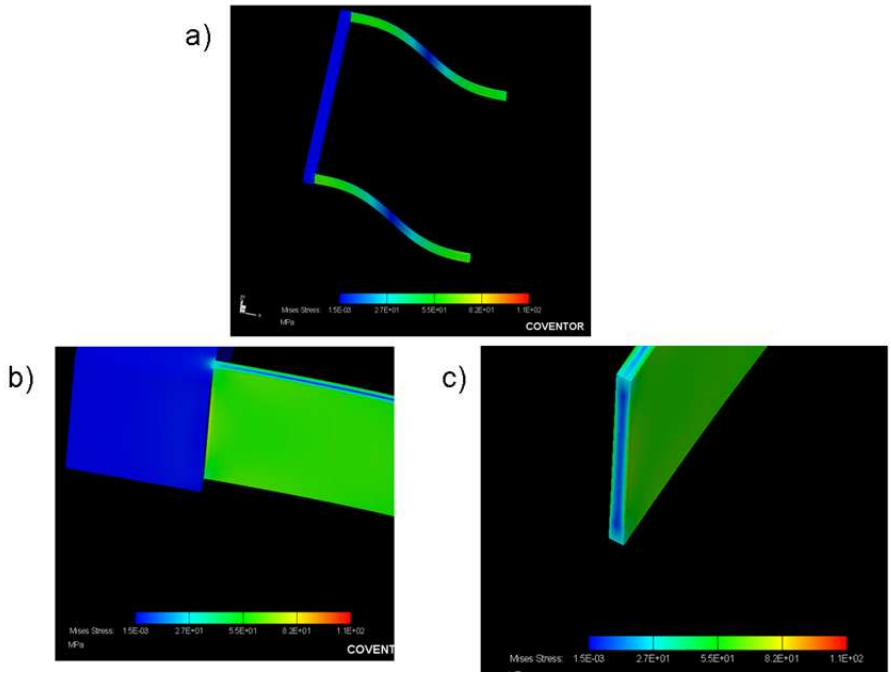

Figure 3.22: *Coventor simulation of the stress in a curved beam as one end is moved in respect to another. A maximal stress of 110*MPa *can be shown.*

even if the system is moved in the X direction, as the total displacement of the combdrives is limited, the shape of the curved springs was optimized to amplify the Y displacement with a factor of two. That way, if both actuators are displaced of a distance d in opposite directions, the corresponding perpendicular motion y of the platform is the following:

$$y \cong 2d \tag{3.11}$$

This result was obtained with a beam given by the following equation [139]:

$$y(x) = \frac{\sqrt{2}}{4}x - \frac{\sqrt{2}L}{8\pi}sin\left(\frac{2\pi}{L}x\right) \tag{3.12}$$

The optimization of the shape of the beam was performed by determining the best value of H (Figure 3.23) parameter for a determined value of L given by the total size of the chip.

Figure 3.23 shows a schematic of the movement of the beam as force is applied on the movable end. Architect (Coventorware simulation software) simulations results are shown in figure 3.24. For these simulations, a beam slightly simplified was used. In Architect, a model exists for the simulation

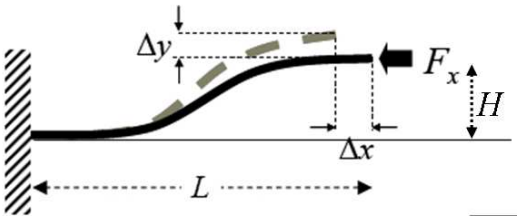

Figure 3.23: *Schematic view of the movement of the free end of the compliant curved beam as a force is applied to.*

of "freeform beams". These can be defined either by a polynomial equation or by points. The approximation of the shape described in equation 3.12 was performed with a set of 13 coordinates. Figure 3.24 shows that as expected, the ratio between the displacement of one end of the beam in the X and the Y directions is of about two. In the highlighted values, for a given deformation with a force of about 40 μN, the displacement of the end of the beam is of about 21 μm in X direction and about 45 μm in Y direction.

Simulations of the complete system were performed in order to get some information about the quasi-static and dynamic behavior of the device. For these simulations, the library-based software Architect was used.

Quasi-static simulations

These simulations were performed to understand how the platform will move as a relatively slow voltage ramp is applied on one or two actuators. The displacement versus voltage can be seen in figures 3.25 and 3.26. In figure 3.25 the simulated signal is applied to only one electrode -electrode B (Figure 3.9)- while figure 3.26 shows the results of a signal applied on both electrodes A and B. These simulations shows that the desired displacement in both directions can be reached. Of course, only part of the reachable area is shown on these graphs, but additional simulations shows the same behavior in the other directions. It can also be seen that a small z displacement of a couple of picometers appears but is negligible. It is so small that it could be due to numerical noise. Anyway, this should not be a problem for the good operation of the device.

Dynamic simulations

Once the static behavior was satisfying, the dynamics of the device had to be studied.

First simulations with small signals were performed in order to determine

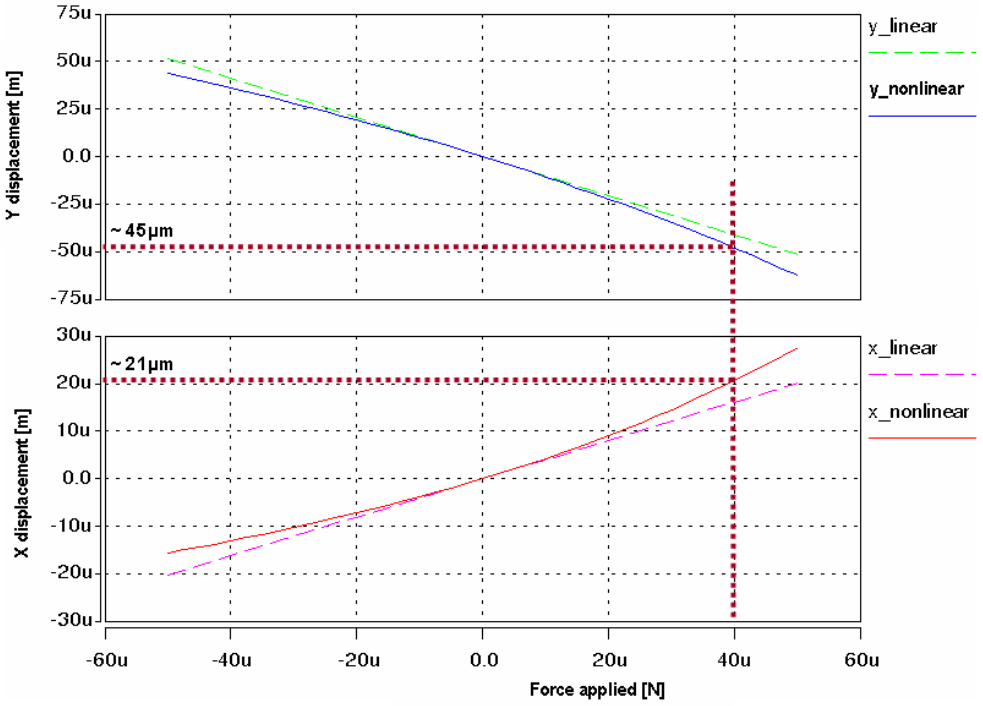

Figure 3.24: *Architect simulations of the curved beam by applying a force* F_x *as shown in figure 3.23. The applied force range is of* $\pm 50\,\mu$N*. In each graph, the linear and non-linear simulation modes are represented. The top image represents the displacement along the Y axis* (Δy*, Figure 3.23) and the bottom one represents the displacement along the X axis* (Δx*, Figure 3.23).*

its intrinsic resonance frequencies. Figure 3.27 shows the results of this simulation. The first visible mode is in the Z direction (Z curve, perpendicular to the surface of the device) at a frequency of 805 Hz. This vertical movement is coupled with out-of-plane rotations of the platform, symbolized by the small peaks showed in RX and RY curves. At the same frequency range, wide peaks can also be seen in the X and Y directions. Figure 3.28 shows a zoom-in of the small signal simulation between 300 Hz and 1200 Hz. They can be slightly more clearly seen in the phase diagram but in both case, as the Q factor is very low they are not very well defined. It is then not easy to determine their exact peak value with this simulation method. The second mode, in the Z direction (with RX and RY rotations) is situated at 2979 Hz and the third is situated at 4712 Hz in the same direction.

The same simulation was performed to determine the intrinsic resonance frequencies of the actuators while they are coupled to the platform. Fig-

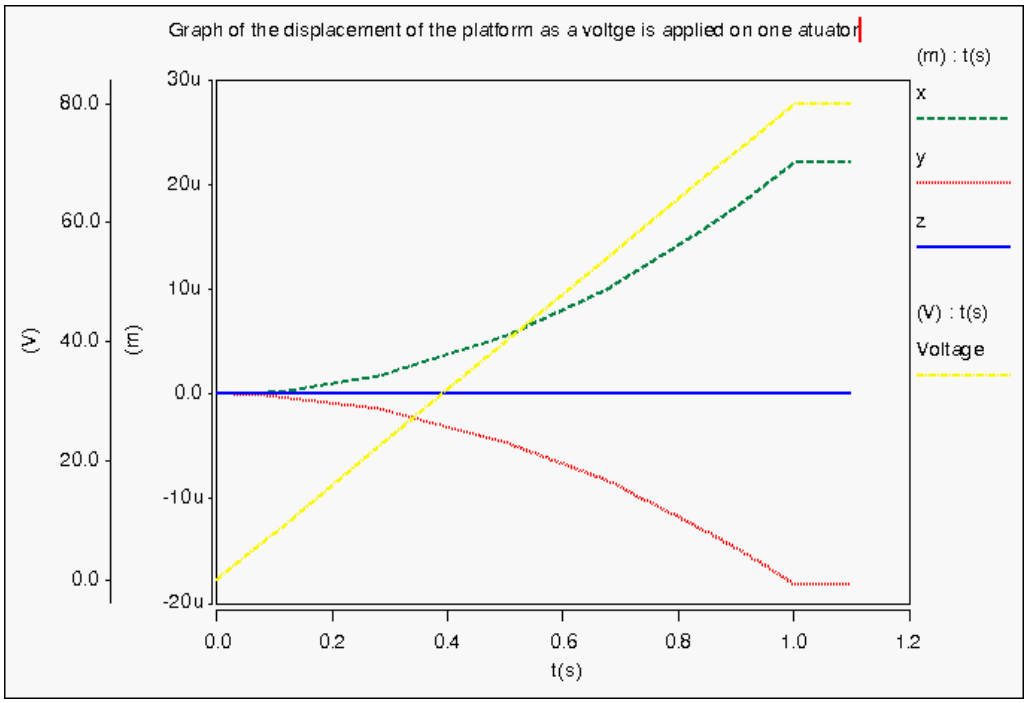

Figure 3.25: *Simulated X, Y and Z displacement of the platform as a voltage ramp is applied on electrode B (Figure 3.9).*

ure 3.29 shows this results for the right actuator. In this case, the main resonance frequencies are exactly the same than previously. The difference comes from the additional modes situated between these main peaks in Z, RX and RX directions. It can also be seen that for this actuator, the resonance in Y is linked to its resonance in RZ as the two curves are perfectly parallel. By symmetry, the left actuator has the same behavior.

Then, step response of the system was studied. By simulating this, a more comparable resonance frequency in the XY-plane can be determined in the interesting directions as the software simulates exactly the same situation than the measured one in section 5.2. In this case, a voltage is applied to the same electrode than previously, but in this case, it is a step of 40 V. Figure 3.30 shows the resulting displacements of the platform in the Y axis (Figure 3.10) as the step signal is applied to the two external electrodes. To obtain the value of the resonance frequency, the signal obtained graph has first to be interpolated in order to get points equidistant along the time axis. Then, the Fourier transform analysis is applied to the resulting graph to obtain the value of the resonance frequency. The result for the Y axis is 695.03 Hz.

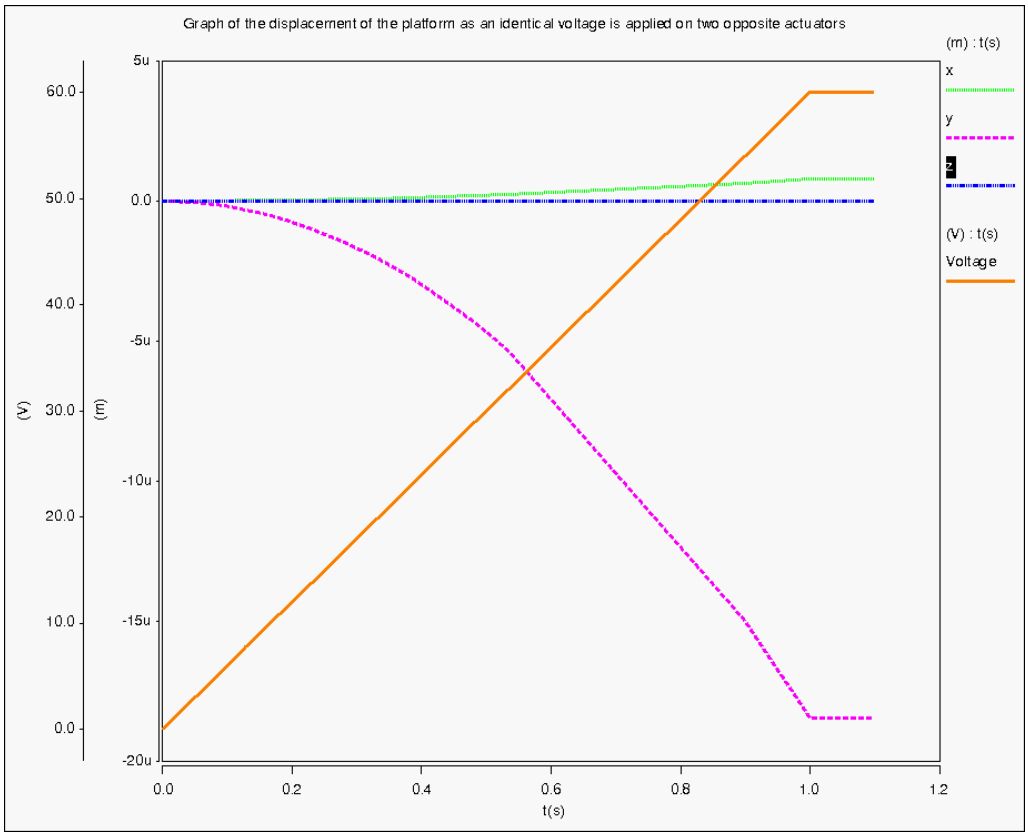

Figure 3.26: *Simulated X, Y and Z displacement of the platform as a voltage ramp is applied on electrodes A and B (Figure 3.9).*

The same analysis can be performed with the step response obtained for the X (Figure 3.31) and XY (Figure 3.32) directions. The corresponding resonance frequencies are the following:

- Resonance frequency along the X axis for an excitation in the X direction: 782.74 Hz
- Resonance frequency along the Y axis for an excitation in the Y direction: 695.03 Hz
- Resonance frequency along the X axis for an excitation in the XY direction: 817.06 Hz
- Resonance frequency along the Y axis for an excitation in the XY direction: 817.6 Hz

Frequency	Axis
695 Hz	Y
783 Hz	X
805 Hz	Z
817 Hz	XY, with an angle of about 37°
2979 Hz	Z
4712 Hz	Z

Table 3.3: *Summary of the simulated resonance frequencies.*

These simulations show that the resonance frequencies varies, especially along the Y axis when the different springs are "loaded" compared to their rest positions. Finally the simulated resonance frequency are summarized in table 3.3.

3.4.2 Application of the simulations to the theoretical model

The simulations of the free beam depicted in figure 3.24 show that there is a factor of two between the horizontal displacement (X) of one end of the beam and the vertical one (Y). Thus, by applying the same displacement ($\pm d$) to both actuators in inverse directions, the platform attached to these will move with an amplitude of $2d$. This has to be confirmed by the measurements (chapter 5.2.2).

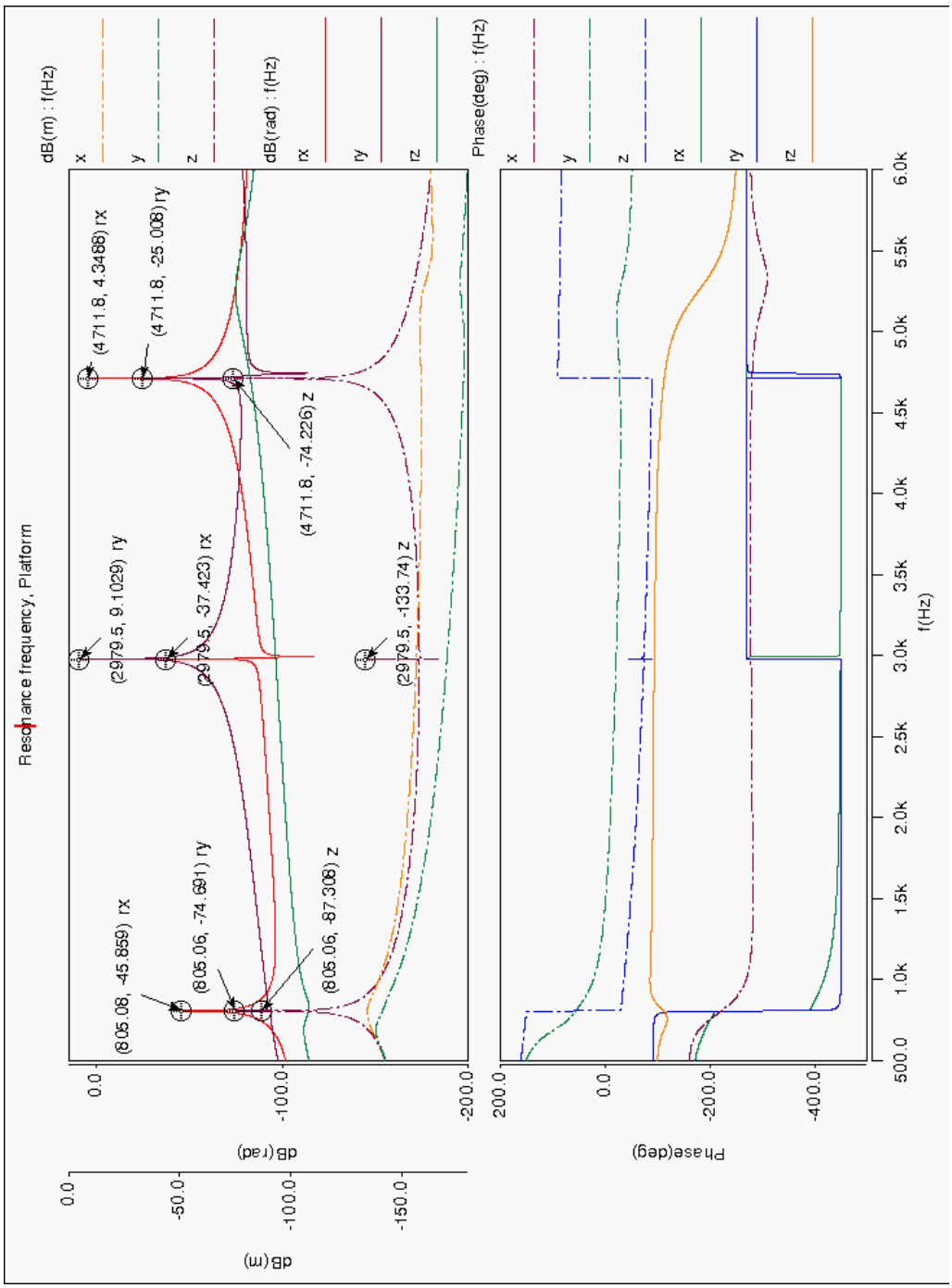

Figure 3.27: *Architect small signal simulation of the platform.*

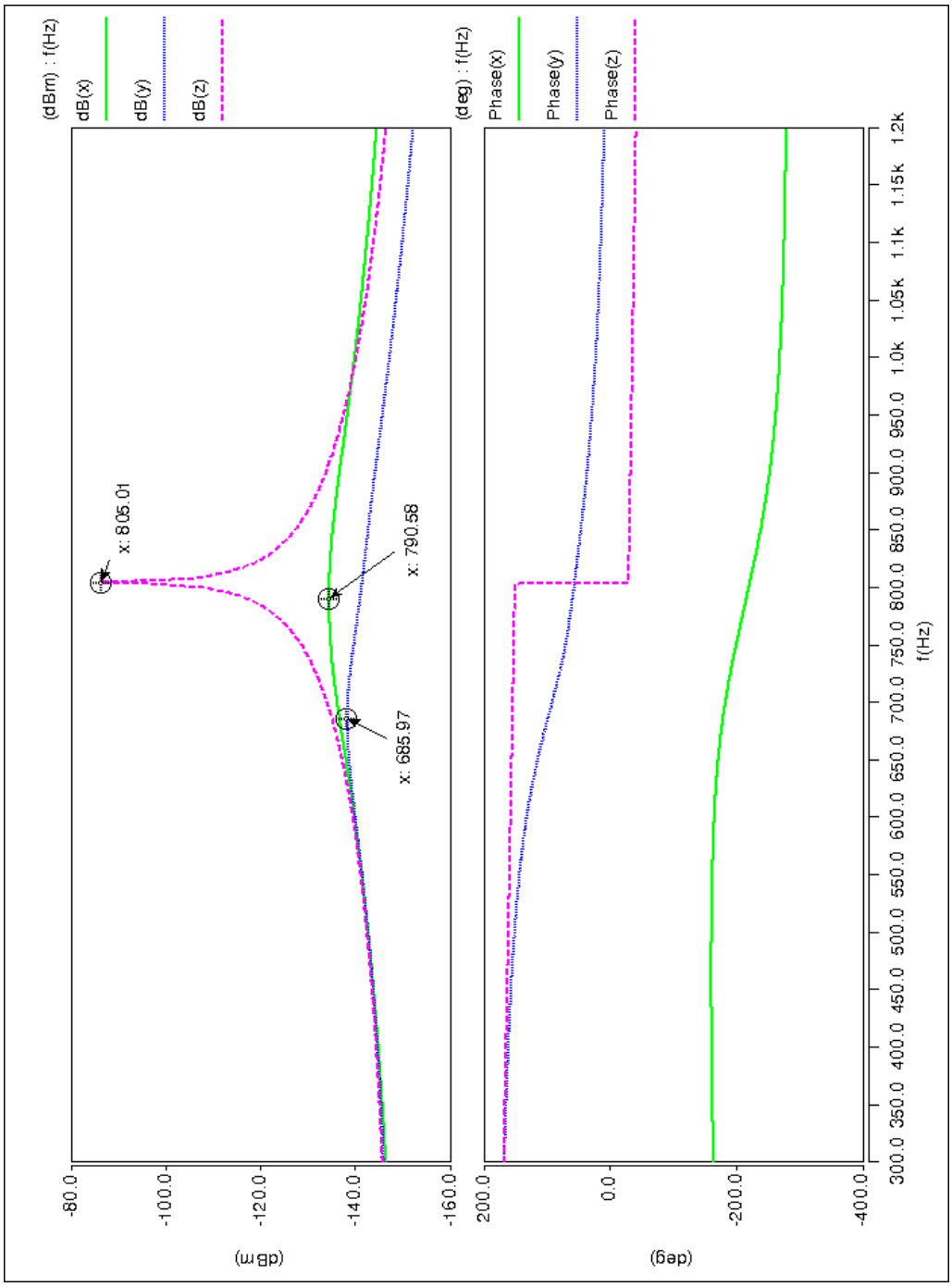

Figure 3.28: *Zoom on the first resonance frequencies of the small signal simulation of the platform.*

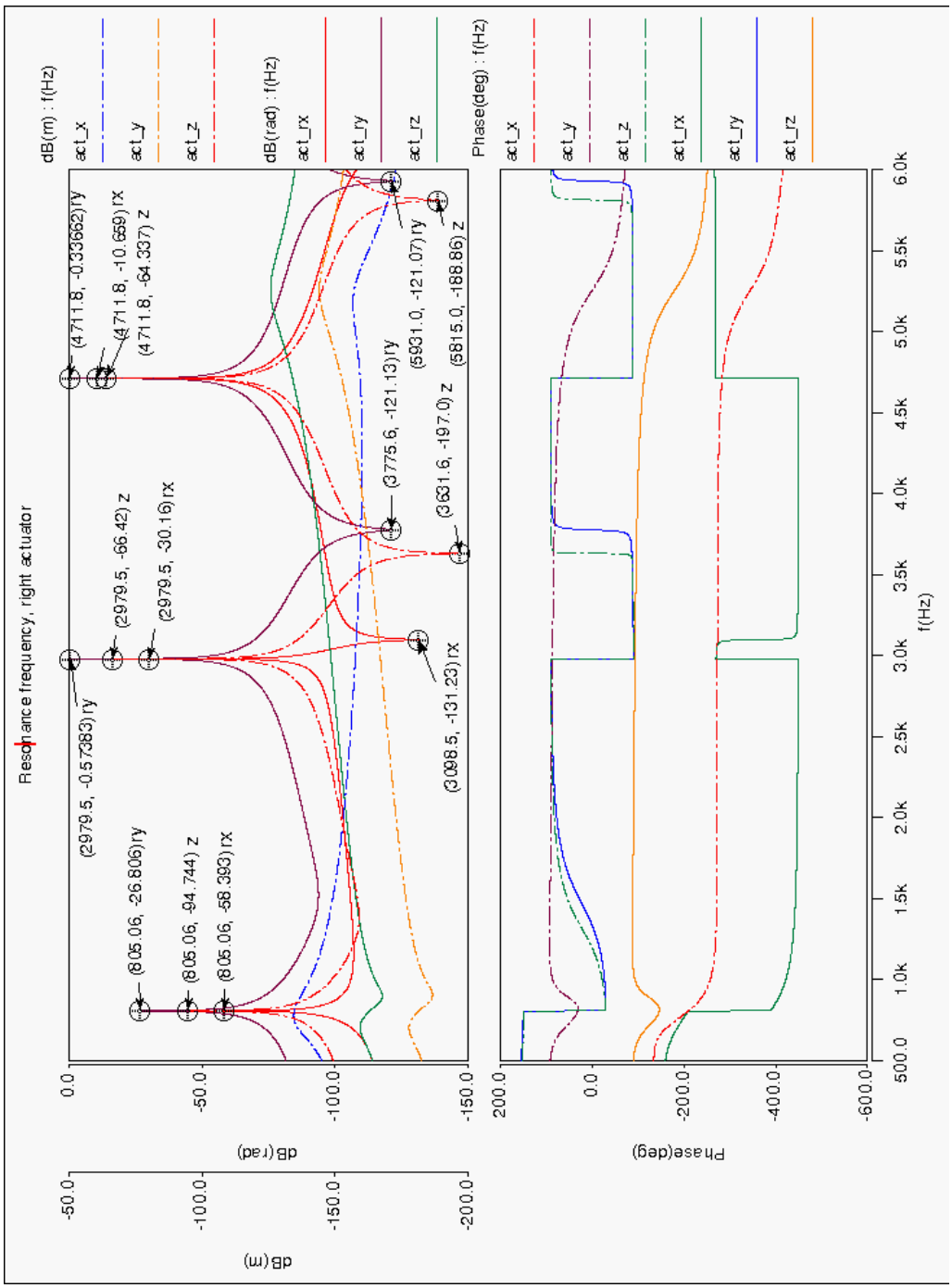

Figure 3.29: *Architect small signal simulation of the right actuator.*

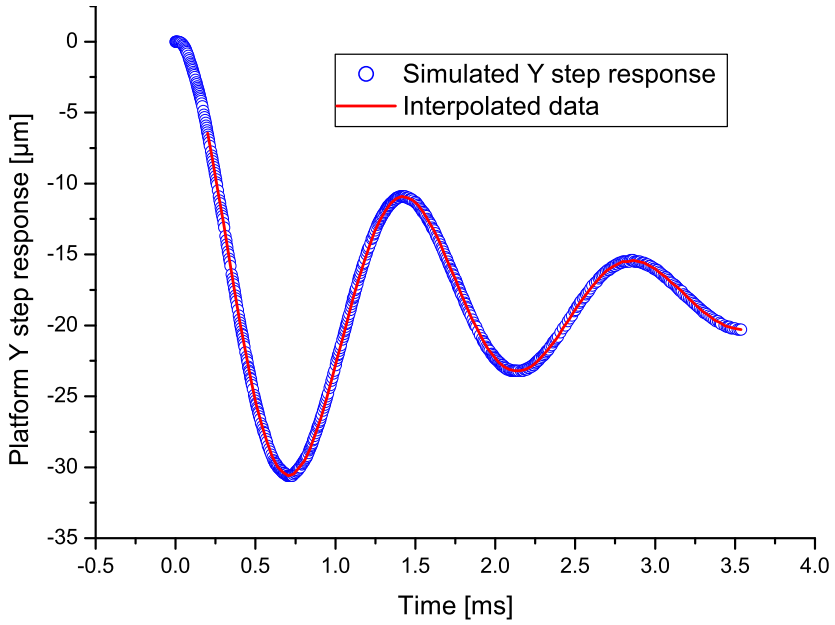

Figure 3.30: *Simulation of the step response of the actuator in "-Y" direction (Figure 3.10). The Fourier transform shows a frequency of 695.03* Hz.

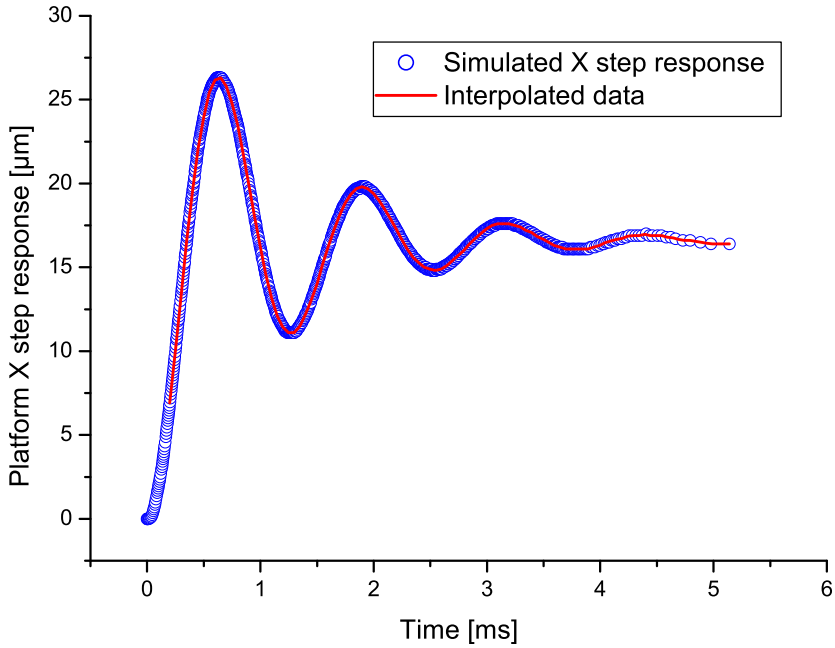

Figure 3.31: *Simulation of the step response of the actuator in "X" direction (Figure 3.10). The Fourier transform shows a frequency of 782.74* Hz.

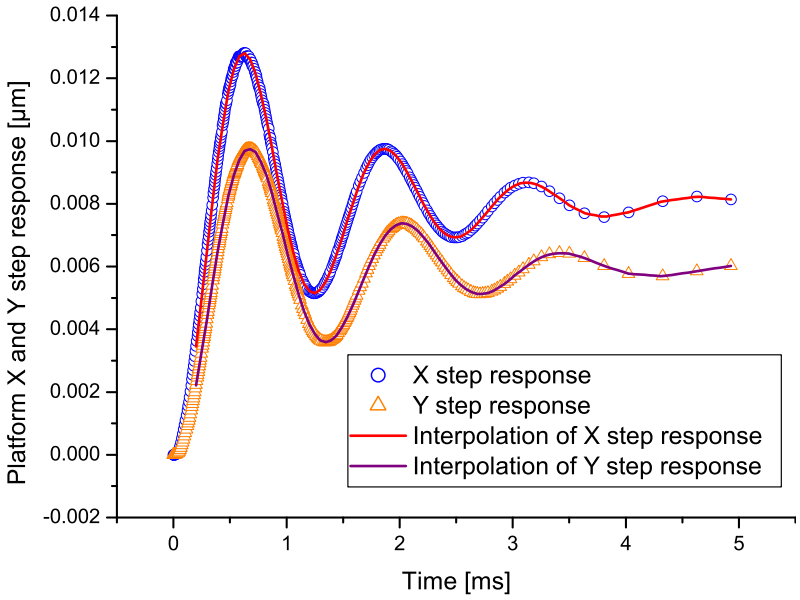

Figure 3.32: *Simulation of the step response of the actuator in "XY" direction. In this case, the platform moves with an angle of about 37° with the "X" axis. The Fourier transform gives frequencies of 817.06* Hz *in X and 817.6* Hz *in Y direction.*

Chapter 4

Fabrication of the device

For the fabrication four main process steps are performed: oxidation (Section 2.3.2), metalization, DRIE with a delay mask process (Section 2.3.6) and etching of the sacrificial oxide layer. In between, to pattern the different layers, photolithographic steps have to be completed. Section 4.2 will describe the complete process flow of the fabrication of the chips.

4.1 Main process steps

In this section, the main process steps, their challenges and limitations will be described.

4.1.1 Oxidation

After a standard cleaning procedure, the wafers are oxidized by thermal oxidation. In standard SOI technology, this layer is used as an additional mask layer. In case of a delay mask process, this oxide layer will be used as mask for the second step of DRIE. Thermal oxidation was chosen here for its homogeneity and the good quality of the layer. Furthermore, thermal oxide growth on both sides at the same time and, as the same layer thickness is obtained on both faces, the bow induced by the stress is quite small.

4.1.2 Metalization

As seen in [140], metalization can be performed by different methods. For this project, lift-off principle has been chosen for two main reasons:

- With this technique, metal does not come in contact with the areas to be etched later. This is an important point to avoid any presence of

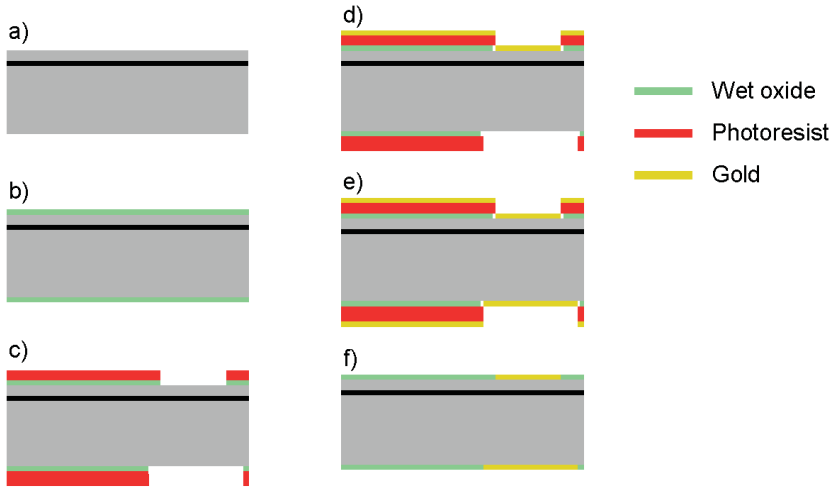

Figure 4.1: *Fabrication steps from the beginning of the process until metalization. a) Bare SOI wafer. b) Wet oxidation of the wafer (2.7 µm). c) Photoresist patterning and oxide etching. d) Topside gold deposition. e) Backside gold deposition. f) Lift-off by dissolving remaining photoresist in acetone.*

metal into the DRIE chamber.

- As the wafer is covered with an oxide layer, the latter has to be etched before the metal deposition. It is then possible to use the same photoresist mask for the lift-off step.

In order to obtain well-defined metal pads, the oxide is slightly overetched. This allows us to have a metal layer as good as if a special lift-off resist layer was used. Figure 4.1 shows the first fabrication steps up to the metalization of the contact pads.

Once the metal is deposited on the wafer, contacts between the gold surface and any machine chamber has to be avoided except some deposition equipments. A method to bury the gold pads during silicon etching had to be studied. The best solution found was to deposit a thick layer of silicon dioxide on both sides of the metalized wafer. As CVD oxide induces a large stress and an unacceptable bow on the wafer, PECVD oxide has been preferred. This deposition method creates a layer of oxide denser and less stressed than what would have been obtained with a standard CVD deposition. A thick layer of 2 µm of this oxide is deposited on the wafer in order to bury the metal contacts and protect the environment and other equipments of any gold contamination.

4.1.3 Delay mask process

After this step, all the unmetalized areas of the wafer are covered by 2.7 μm of thermal oxide and 2 μm of PECVD oxide. As the PECVD layer acts as a protective layer for the metal pads, it is removed from the non-metalized parts of the wafer. On the topside, the second step of the delay mask process requires only a very thin oxide mask. If the 2.7 μm thick oxide was used, a lot of the oxide would be mainly overetched during the RIE patterning due to the angle of about 35° of the etching. As the structures on the topside are very thin and have to be defined very precisely, a timed oxide etch step is performed on the topside to thin out the oxide layer up to a layer thickness of about 500 nm.

After this wafer preparation, the delay mask process can be performed as seen in section 2.3.6.

For the backside cavity, as a laser diode and a tilted mirror have to be placed in the chip cavity, the latter has to be as deep as possible. On the other hand, the remaining silicon membrane must have a certain thickness in order not to be too fragile. Another limitation comes from the thickness possible to etch with the oxide mask. As seen in section 2.3.2, the etching depth is limited by the oxide thickness. It was then decided to perform etching depths of max. 100 μm for the first etch step and at least 250 μm for the second. Figure 4.2 shows the backside of the chip after the DRIE delay mask etching process step. On this picture, the large central circular structure is sacrificial. It was designed in order not to get large silicon dioxide membranes during the process. Later, during the HF vapor phase etching process, this structure is released and drops off the device.

On the device layer, first devices have been built with topside cavities of 25 μm into the platform. Primary assembly tests showed that a shallower etching would be better. The second etching step was then set to a depth of 3 μm as seen in figure 4.3.

4.1.4 Oxide etching

As seen in [140], HF vapor phase etching of the buried oxide is used. Several reasons explain the choice of this etching technique compared to standard wet etching.

- The first reason is to avoid sticking during the release of the movable parts of the chip. The HF vapor phase etching being a quasi-dry process, there is no presence of liquid and capillary forces between the movable structures that could cause sticking.

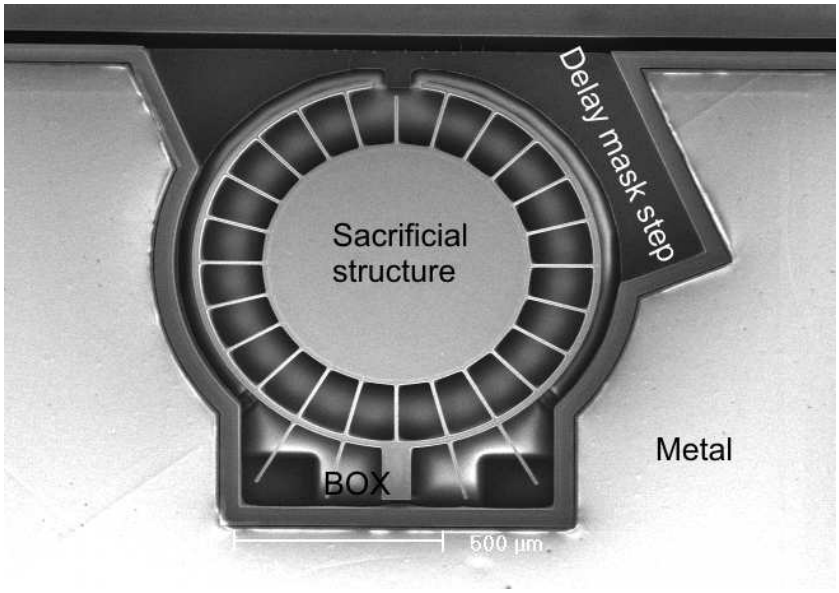

Figure 4.2: *SEM image of the backside of the chip after the delay mask etching showing the large backside metal contact protected by the PECVD oxide layer, the buried oxide of the wafer around the sacrificial layer and the delay mask process step on the upper part of the image.*

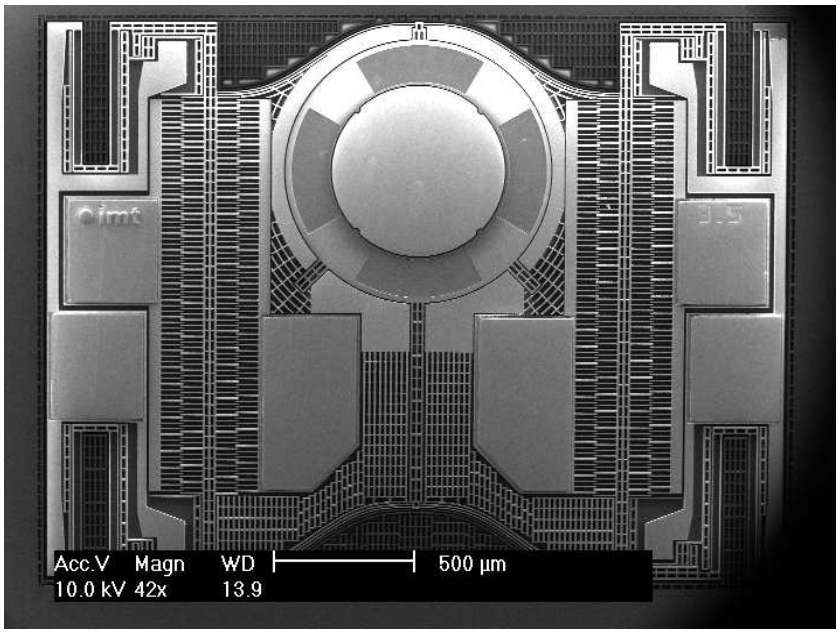

Figure 4.3: *SEM image of the topside of the chip after the delay mask etching. In addition to the functional structures, this image also shows the sacrificial structures added to the mask to make the process feasible.*

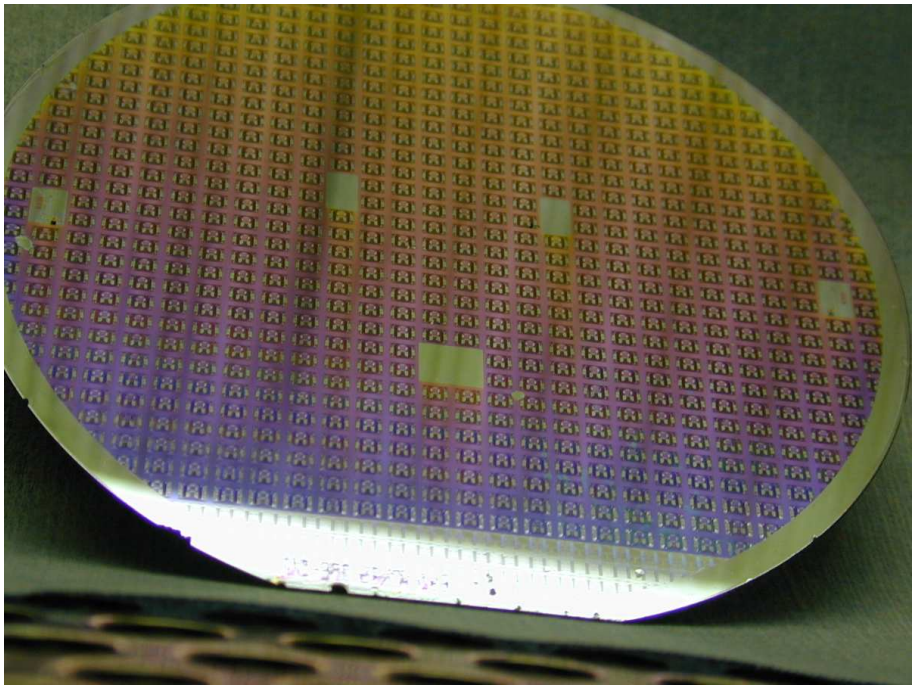

Figure 4.4: *Image of the wafer before the release step.*

- The second reason is the possibility to singulate the chips out of the wafer frame during the release process to avoid the need to dice the chips and perform another wet processes after the release step.

- The third reason is that the wet etching is simply impossible due to the through holes across the wafer. In a BHF bath for example, liquid flow would have created important out of wafer plane deformations of the released structures and the yield on the wafer would have been very low or nil.

As an oxide layer has been deposited on the electrical contacts on both wafer sides, vapor phase etching has to be performed on both sides of the wafer. A first etching step is performed on the backside of the wafer and the latter is then turned such as the device layer will face the reactive vapor.

After this final etching step, chips are released and separated from the wafer frame. Figure 4.4 shows the processed wafer before this last step and figure 4.5 depicts the remaining wafer frame after the release and the separation of the chips.

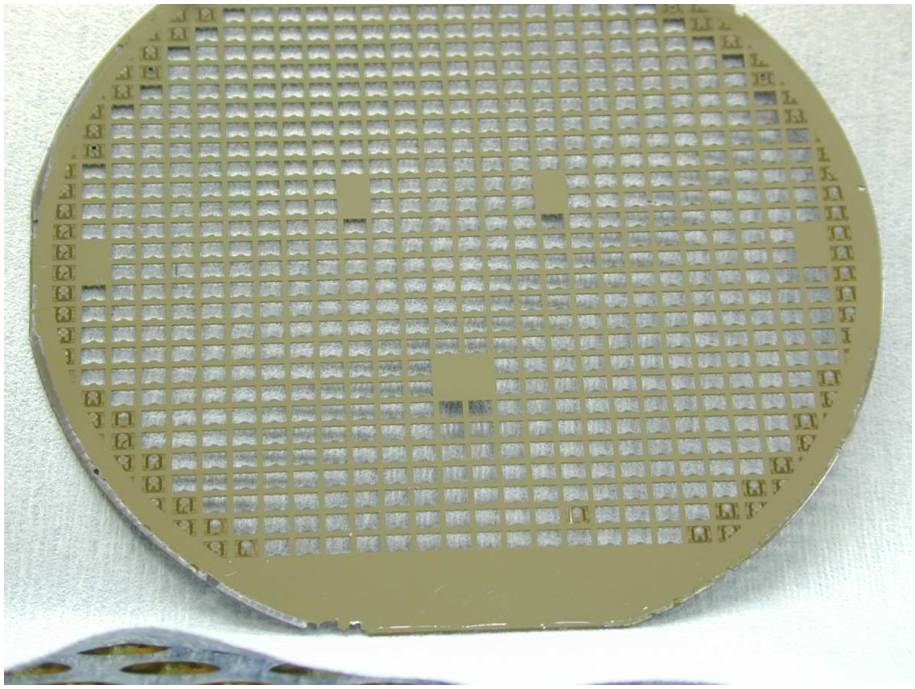

Figure 4.5: *Wafer frame after the release step.*

4.2 Complete process flow

Figure 4.6 shows a schematic of the whole process flow with the following steps:

a) Bare wafer.

b) Wet oxidation.

c) Photolithography and patterning of the oxide.

d) Gold evaporation (topside).

e) Gold evaporation (backside).

f) Lift-off in acetone using oxide and photoresist masks.

g) PECVD deposition of oxide.

h) Patterning of the PECVD oxide by photolithography and wet BHF etching.

i) Thinning down of the topside wet oxide in BHF.

j) Photolithography to define the second DRIE etching step.

k) BHF etch of the oxide.

l) Photoresist stripping in oxygen plasma.

m) Photolithography to define the first DRIE etching step.

n) RIE etching of the wet oxide.

o) First DRIE steps on top- and backside.

p) Photoresist stripping.

q) Second DRIE steps on top- and backside.

r) Vapor phase HF etching of the buried oxide to etch the remaining PECVD oxide, release the movable structures and singulate the chips.

4.3 Assembly tool fabrication

In parallel with the device, the assembly tool presented in section 3.2.4 was fabricated. For this, another SOI wafer was used in order to get a very precise etching depth. Some tests were made previously with a bulk wafer but these were not conclusive because of the inhomogeneity of the DRIE etching depth. The final process used is based on a single photolithography process and one DRIE etching step. To obtain the correct depth, an SOI wafer with a handle wafer of 360 μm and a device of 100 μm is used. The patterning of the opening was defined on the backside and DRIE etched. The obtained structure is shown in figure 4.7.

4.4 Assembly of the final device

The assembly of the submount was performed at Hymite GmbH (Figure 4.8). They provided six silicon submounts with electronics components assembled and wirebonded onto and the rest of the assembly was performed by using a simple assembly setup. It is composed of a planar micrometric table with three degrees of freedom (X, Y displacements and rotation) and a vacuum gripper placed above and controlled with a micrometric screw. The alignment is performed manually under an optical binocular with a magnification of 50x. Although this setup is quite simple, it is easily adaptable to any situation.

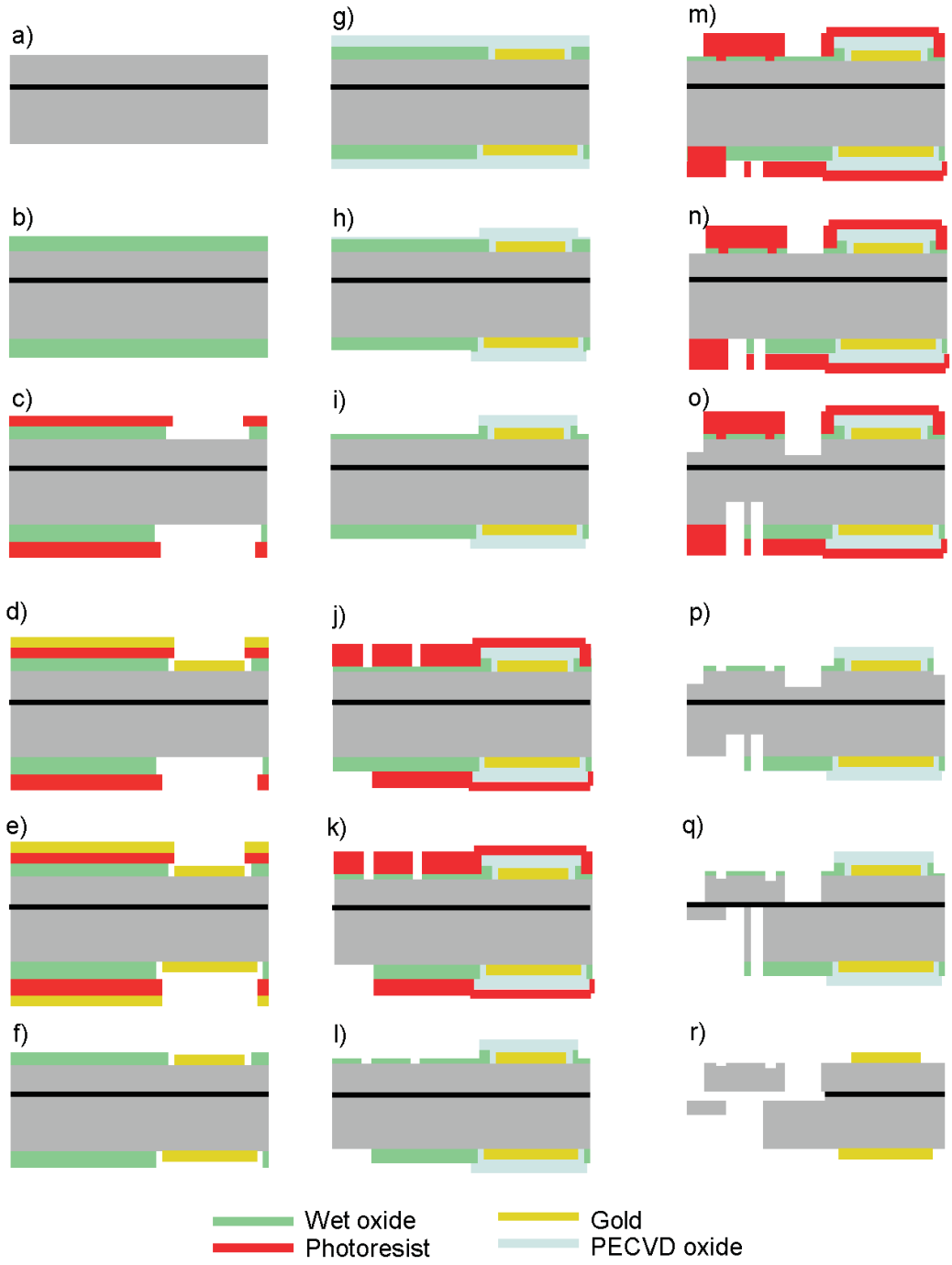

Figure 4.6: *Complete process flow of the fabrication of metalised MOPOS devices.*

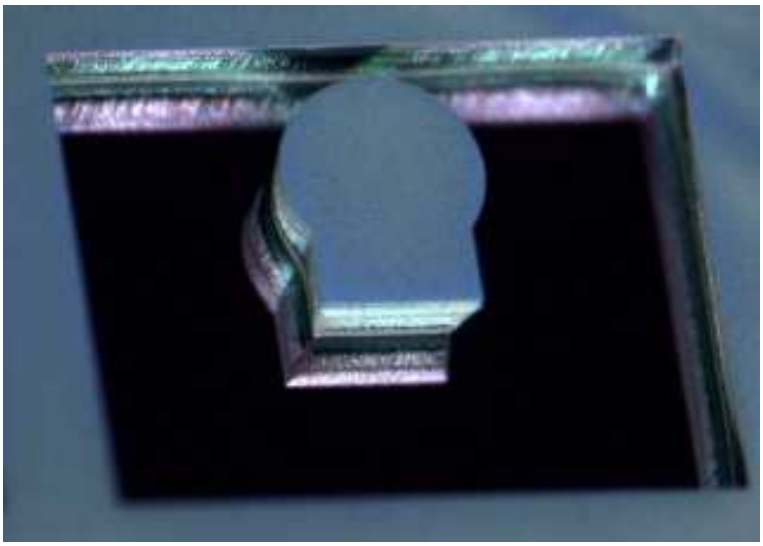

Figure 4.7: *Picture of one of the assembly tool (courtesy of Hymite GmbH). One can clearly see the cavity etched to place the chip into and the central island supporting the movable platform for the assembly of the lens.*

It is also possible to position quite precisely the different components to be assembled as the stages can be displaced using micrometer screws. The precision is then more limited by the optical performance of the optics used to observe the system than by the assembly setup. As the binocular used has a limited depth of focus, it was not possible to focus at the same time on both chips to be assembled, limiting the precision of the alignment.

A complete assembly process flow had to be developed to assemble the different components of the system. Figure 4.9 shows this procedure.

The first assembly step was to glue the lens on top of the platform on a tested -and perfectly working- MEMS device. This was done by using the assembly tool described in section 3.2 and shown in figure 4.7. Once the chip was placed in the cavity of the assembly tool, small droplets of glue are dispensed in the cavities of the platform (Figure 4.10). The size of these drops have to be well controlled to get -as intended- a zero-gap assembly between the MEMS platform and the assembled lens. The glue used is a two components epoxy (Hysol Re2039 and Hd6652) with a low viscosity.

The lens is then assembled on the platform using a vacuum tool. Even if the passive alignment structures are not visible, it can be clearly seen that they are functional. By approaching the roughly aligned lens vertically, one can see the platform moving in order to allow the passive alignment structures of the lens to fit into the hole of the platform. By removing the

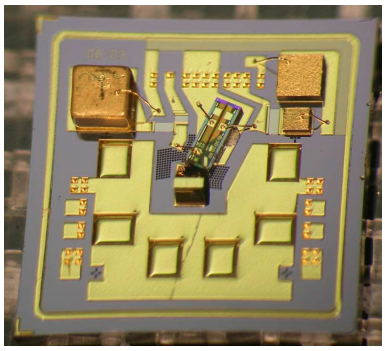

Figure 4.8: *Picture of the silicon submount assembled at Hymite. On the lower part of the image, one can see the two small alignment structures (crosses) for the positioning of the MEMS chip.*

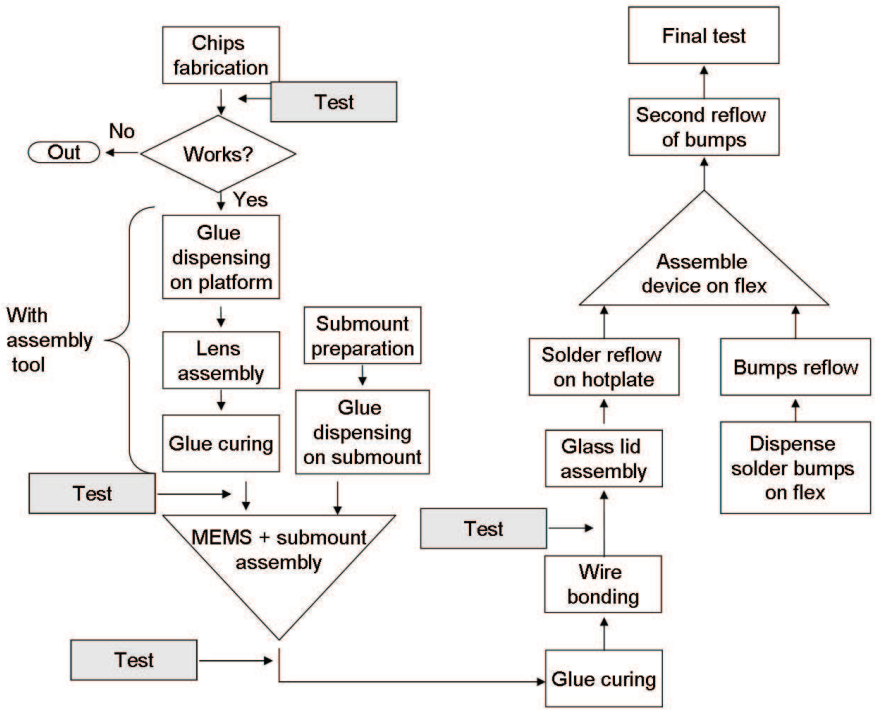

Figure 4.9: *Flowchart of the assembly process.*

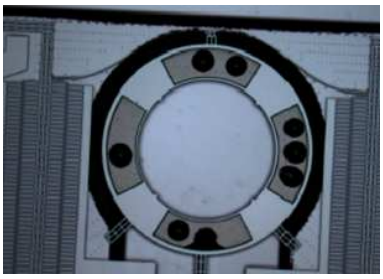

Figure 4.10: *Picture showing the droplets of glue in the cavities of the platform of a chip placed into an assembly tool. Tests were performed with one, two or three droplets of glue per cavity.*

vacuum and applying a small force on the lens, the lens comes in contact with the platform on its whole surface. The chip obtained is then put into an oven to cure the glue at 80°C during 2 hours.

Once the epoxy is cured, the chip is assembled to the silicon submount. In this step another epoxy glue (more viscous) and conductive glue are used to attach the MEMS on the submount. The conductive glue is used to get a good electrical connection between the handle part of the chip and its corresponding electrode while the epoxy glue is used to get a strong adhesion of the chip on the submount without using an important quantity of glue. The adhesion has to be strong enough to withstand the force applied during the wire bonding of the chip. Once drops of glue are dispensed in the cavities of the submount, the chip is assembled using the vacuum tool and precisely aligned on the silicon base. As there is no passive alignment structures, it is much more complicated to perform the alignment of these devices. Furthermore, as the chip to align is quite large compared to the field of view of the binocular at high magnification, it is not possible to align both sides of the chip at the same time. Nevertheless, the assembly was achieved with a precision of a couple of microns. At that stage of the assembly, it is possible to see how important is the depth of the cavity on the backside of the chip. Figure 4.11 shows the position of the laser diode and its wirebonding into the cavity. Prior to wire bond the MEMS chip, the glue is cured in an oven during 2 hours. Figure 4.12(a) shows the chip assembled and wire bonded on a silicon submount.

After the components are assembled and connected on the submount, they are proctected by a glass lid. As the solder paste present on the ring of the glass lid had to be heated up to 300°C, its alignment was performed on a hot plate. That way, the device could be directly heated in place after the lid was aligned on the submount.

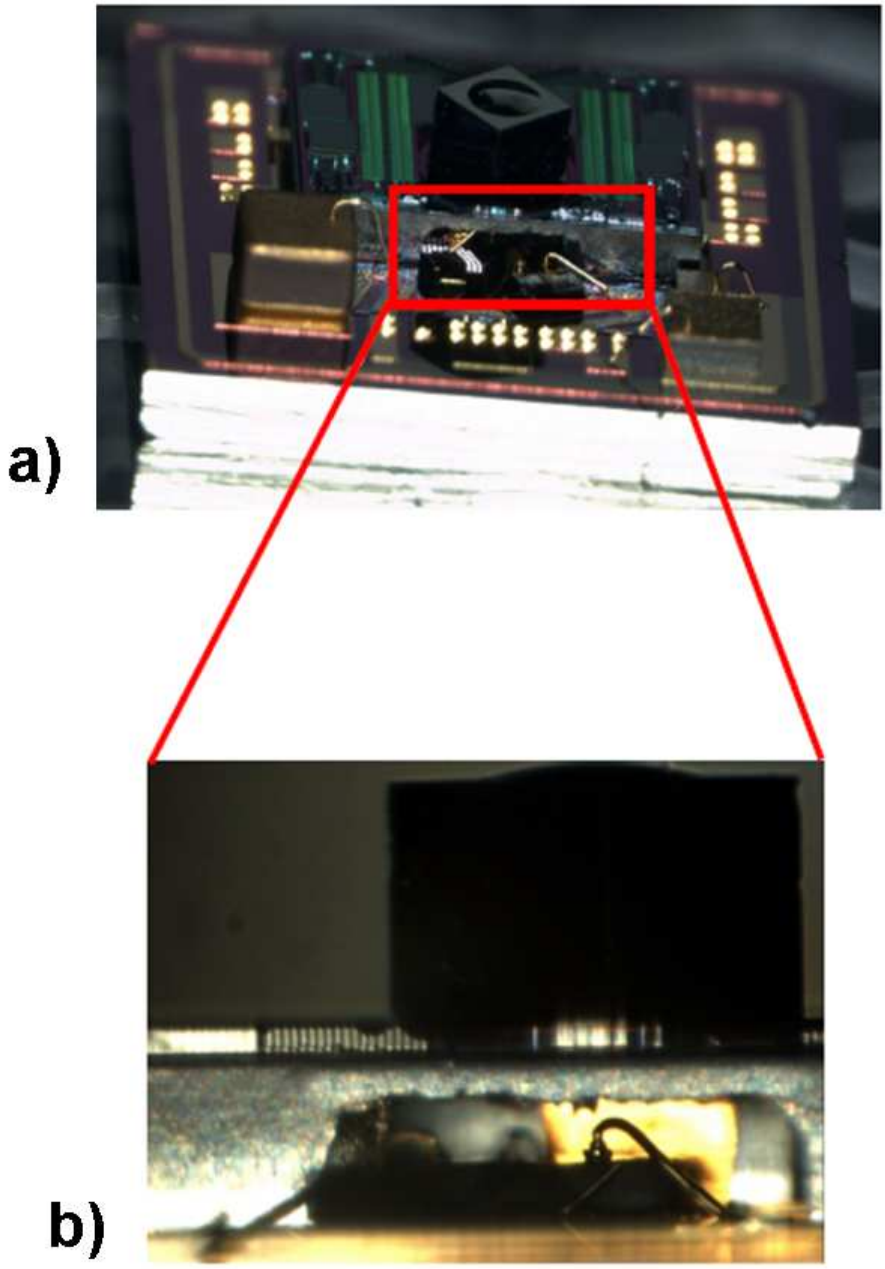

Figure 4.11: *a) Picture of the chip assembled on the submount. b) The close-up view shows the position of the laser in the cavity created on the backside of the chip and the microlens glued on top of the platform.*

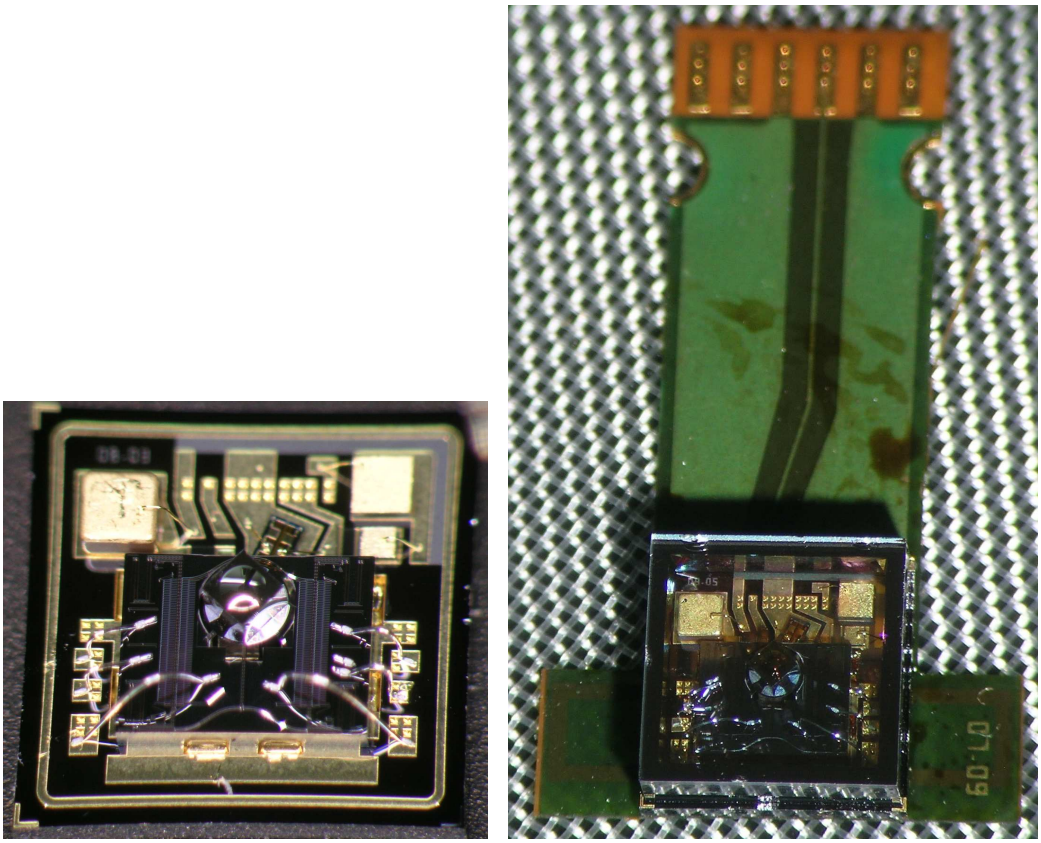

(a) (b)

Figure 4.12: *Pictures of the MEMS assembly. a) Device assembled and wire bonded on a silicon submount. b) Final assembled system containing the MEMS, the lens, the submount, the glass lid and the flex.*

The last assembly step was then the flip chip bonding [141, 142]. As it was not possible to perform this operation in-house, it was carried out at Microbonding SA. First, solder bumps were placed on the electrodes of the flex and reflowed. Then, the encapsulated device was aligned on the flex and a second reflow step was performed to bond both chips together. The final result of the assembly is shown in figure 4.12(b).

Chapter 5

Characterization of the actuator

In the following chapter, the results of the fabrication will be shown. After presenting images of the device, details will be given about the different unexpected phenomenon that appeared during the process. Then, the displacement and locking behaviour will be exposed. Finally, the assembly of the complete system will be presented and the optical measurements results will be shown and compared with the expected values.

5.1 Fabrication results

The silicon device has been built following the process shown in figure 4.6. Figure 5.1 and 5.2 shows SEM images of the fabricated device.

5.1.1 Small dots

With a close up view on the surface of the handle wafer on the device side, small dots can be seen. Figure 5.3 show these small structures. The periodic placement of the dots is the same than the one of the sacrificial structures etched on the device layer. Following this observation, the question is : where do these come from?

Obviously, it somehow comes from the process and is related to the HF vapor phase etching.

One possibility is that these dots could come from an accumulation of the doping ions present in the oxide of the SOI wafer. Boron highly doped wafers were used for the fabrication of the chips. When boron doping is used, a relatively high concentrations of these ions are also present in the oxide. Figure 5.4 shows the concentration of boron ions in the silicon and in the oxide. It clearly shows that the concentration in the oxide is about the same

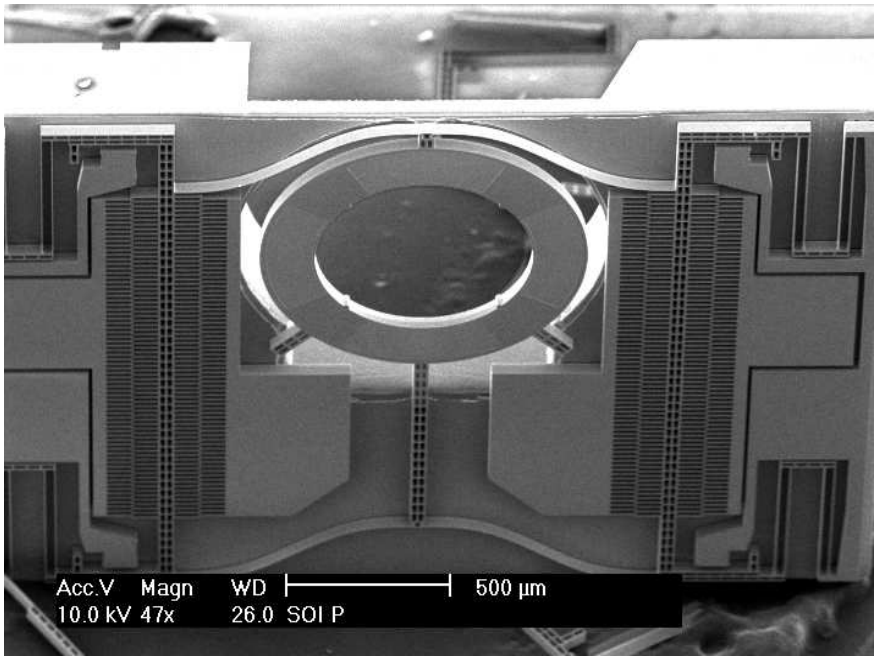

Figure 5.1: *Sem image of the device layer side of the fabricated chip.*

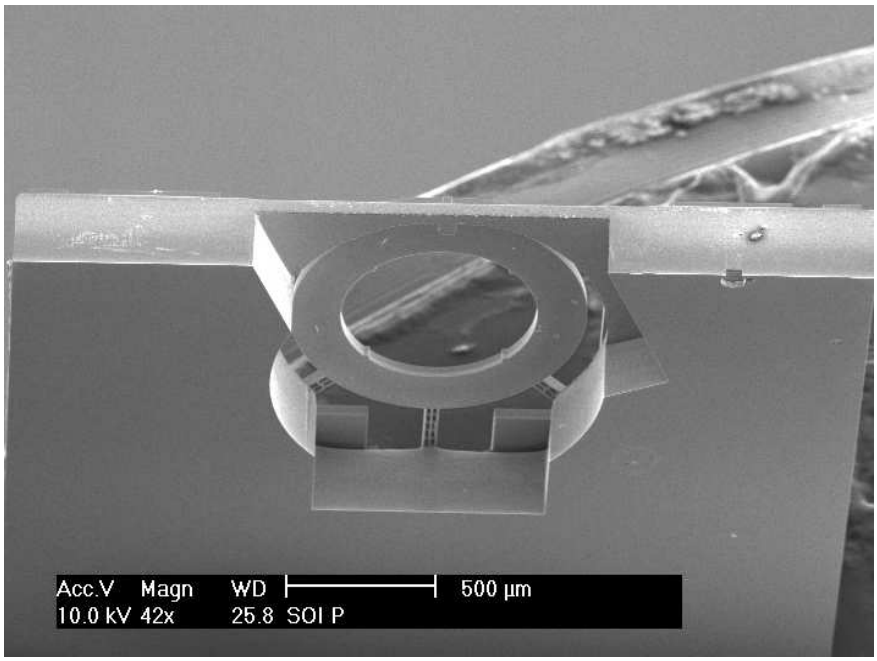

Figure 5.2: *Sem image of the backside of the fabricated chip.*

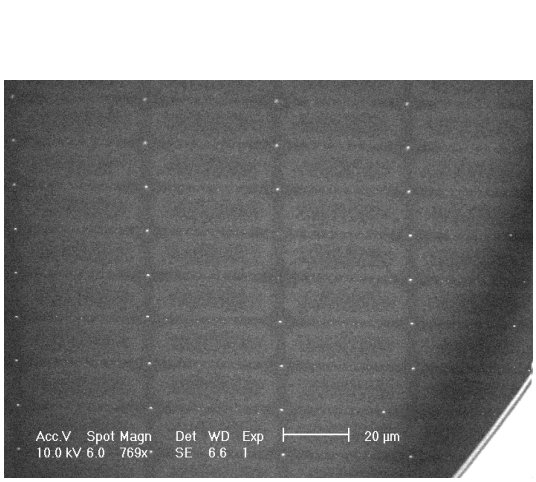

(a)

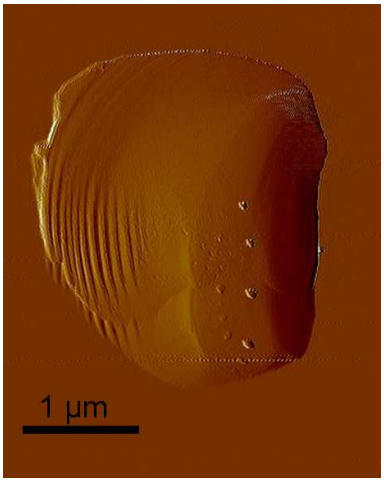

(b)

Figure 5.3: *Images of the small dots present on the handle wafer surface. a) SEM image. b) AFM image. The size of these are about 1-2* μm *in diameter and 50* nm *in height.*

than in silicon. For silicon bulk resistivity of 0.01 Ωcm, the doping concentration in the oxide is about $5 \times 10^{19}\,\mathrm{cm}^{-3}$. During oxide etching, silicon dioxide disappears but the ions of boron stay where the reaction droplets is forming. Figure 5.5 shows the possible scheme of formation and concentration of the atoms at the points where the oxide is etched at last. It also depicts an other possible scheme of formation of these dots coming from residues present at the oxide surface.

To determine if this theory is plausible, we can compare the size of the dots with the volume of boron contained in the oxide.

The boron atoms are concentrated at the points situated below the grid of the sacrificial structures. This corresponds to an area of $37 \times 19 = 703\,\mu\mathrm{m}^2$. With an oxide thickness of $2\,\mu$m, the volume is $V_{\mathrm{SiO_2}} = 703 \times 2 = 1406\,\mu\mathrm{m}^3$.

The total number of boron atoms contained in this volume is then:

$$N_{\mathrm{boron}} = \mathit{Boron\ concentration} \times \mathit{Volume\ of\ SiO_2}$$

$$N_{\mathrm{boron}} = 5 \times 10^{19} \times 1.406 \times 10^{-9} = 7.03 \times 10^{10} \tag{5.1}$$

The mass (in grams) of an atom of boron is:

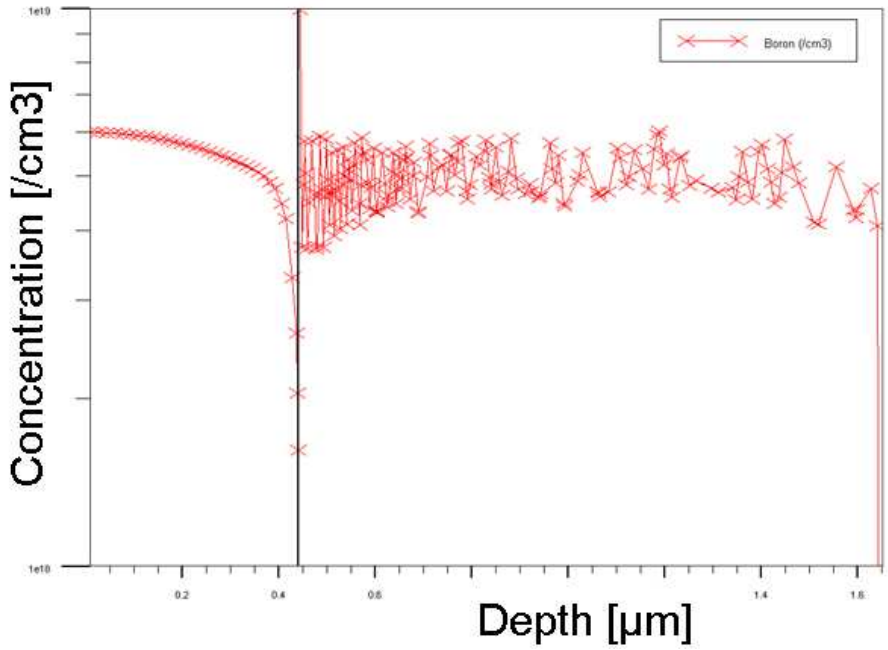

Figure 5.4: *ATHENA simulation of the boron concentration at the interface between doped silicon and growth oxide.*

$$\begin{aligned} M_{\text{boron}}^{\text{grams}} &= \frac{Atomic\ weight\,\text{amu}}{N_{\text{Avogadro}}\,\text{mol}^{-1}} = \frac{10.811}{6.022\times10^{23}} \\ M_{\text{boron}}^{\text{grams}} &= 1.7952\times10^{-23}\,\text{g} \end{aligned} \tag{5.2}$$

The volume of boron can then be determined by:

$$\begin{aligned} V_{\text{boron}} &= \frac{Mass\ of\ boron}{Density\ of\ boron} = \frac{M_{\text{boron}}^{\text{grams}}\times N_{\text{boron}}}{Density\ of\ boron} \\ V_{\text{boron}} &= 5\times10^{-13}\ cm^3 = 0.513\,\mu\text{m}^3 \end{aligned} \tag{5.3}$$

Where the density of boron is $Density\ of\ boron = 2.46\,\text{g/cm}^3$.

The comparison of this value with the size of the dot shown in figure 5.3 shows that the volume is in the same order of magnitude. This explanation can then be verified by other techniques such as EDX (Energy-Dispersive X-ray spectroscopy) analyze or TEM (Transmission Electron Microscope) imaging prepared with a FIB (Focused Ion Beam).

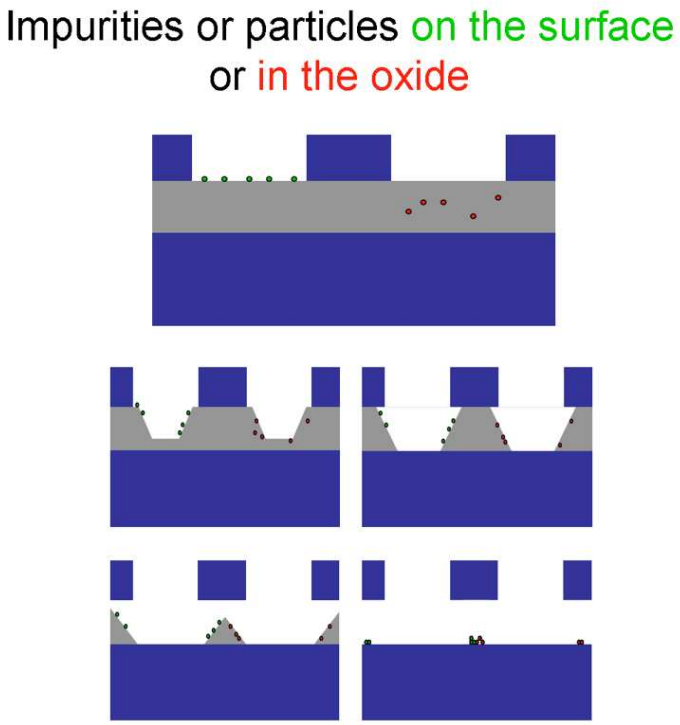

Figure 5.5: *Possible scheme of formation of the small dots. These could come from the two phenomenon shown. On the left side, particles or impurities present on the surface of the oxide are finally deposited under the released structures. On the right side, the same possible phenomenon with impurities or particles present inside the oxide is depicted.*

Unfortunately, boron cannot be detected by EDX or TEM analysis. To determine if these structures come from the dopants presents in the oxide, the same process was performed with Arsenic doped wafers. After vapor HF release of the sacrificial structures, the same dots could be observed. By analyzing the composition of these, information about the ones created on p-doped wafers can be deducted. If Arsenic is found on n-doped wafers, it would mean that in the case of p-doped wafers, the studied structures should be made of boron.

A first EDX analysis was made on structures formed on n-doped wafers but as their sizes being very small, nothing else than silicon was found. It was then decided to analyze them by TEM. For this analysis, as TEM can be performed only on very thin samples, a FIB (Focused Ion Beam) was used to cut a very small piece of silicon to be analyzed. A first gold protective layer was sputtered on the device. Then, a metal mask was deposed on the small bump and the slice was cut into the silicon using FIB. Figure 5.6 shows the TEM image and its analysis. In the area corresponding to the studied dot, nothing else than silicon and a very little bit of oxygen was found. This analysis does not confirm any of the possible explanations exposed before. This should mean that either these dots are remaining silicon dioxide that is not etched, pure silicon that is initially present into the silicon dioxide or silicon "dusts" coming from DRIE etching of the silicon.

5.1.2 Silicon hairs

After fabrication of the devices, small silicon hairs were observed on the side of the steps etched in the backside. Figure 5.7 shows these small silicon needles. Even if these were not a problem from a mechanical point of view, a solution had to be found to remove them because of electrical issues. As seen in chapter 4.4, as a laser diode has to be assembled and wire bonded under the chip, any electrical short circuit has to be avoided between the wires of the diode and the MEMS chip. Additionally, the presence of any small silicon particle has also to be avoided between the electrodes and the combs of the actuator to prevent shortcuts that will burn the actuator and thus returning the chip disfunctional.

To remove these needles, an additional isotropic SF_6 etching flash had been added at the end of the etching process after the oxygen plasma. With this etching, the shape of the sidewalls are slightly modified by thinning the silicon structures. These modifications are quite small (about half a micrometer) and do not prevent a correct behavior of the device. Fortunately, this additional step is not required on the device layer side of the wafer because in this case, it would have modified the width of the thin beams and

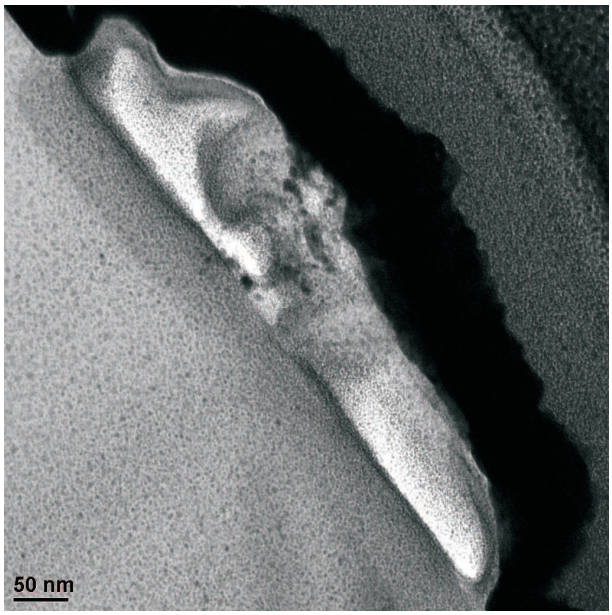

Figure 5.6: *TEM image of the slice cut by FIB. The different layers can be seen in the following order: platinum (first layer on the right side of the image), gold (black layer on the image), analyzed dot, silicon (gray material on the bottom-left of the picture).*

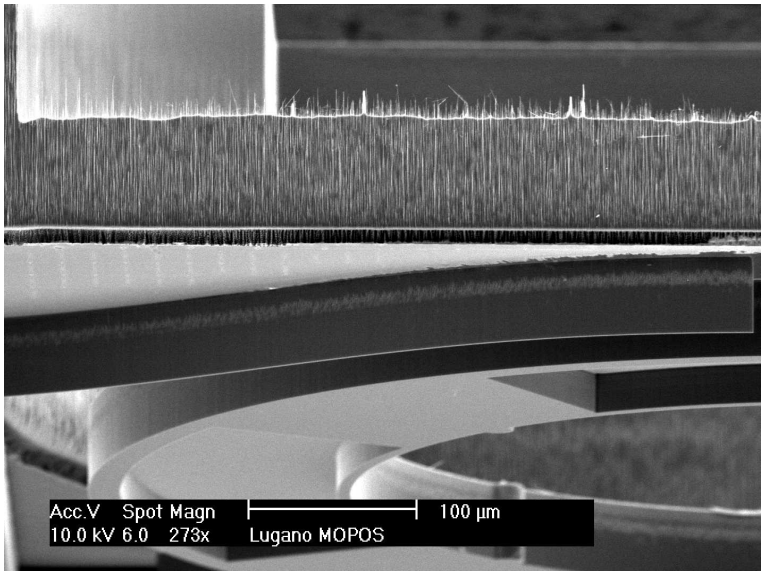

Figure 5.7: *SEM picture of the unwanted silicon hairs on the backside step.*

change the characteristics of the chip.

5.2 Displacement characterization

To characterize the displacement of the actuator, the best way is to divide its movement into three main axis. The X axis and the Y axis by applying the same voltage on two actuators and the XY direction by applying a voltage to only one combdrive pair.

Most of these measurements are performed using a Veeco Wyko 1100 DMEMS white light interferometer to measure at the same time the planar displacement and the vertical position of the platform. They were achieved on a MEMS device before any assembly (i.e. without lens) to allow to be compared to the simulated values. To measure the precise position of each element of the chip, the pattern recognition toolbox of Matlab was used. Figure 5.8 shows the processed image with the different anayzed structures position.

5.2.1 Movement parallel to the X axis

By applying the same signal to both actuators in order that they move in the same direction and of the same amount, the platform moves the same way along the X axis. Figure 5.9 shows the resulting displacements in X, Y and Z

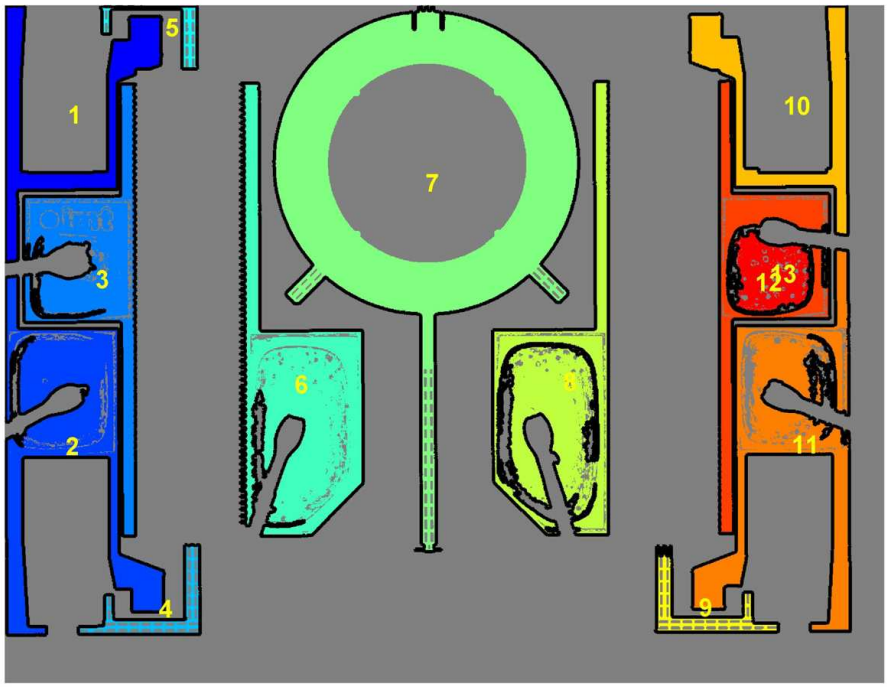

Figure 5.8: *Processed image used for the pattern recognition toolbox of Matlab.*

as such a signal is applied. The X displacement shows a quadratic behavior as expected. The green curve also shows that the platform is lifted slightly during the displacement. This should be due to the non symmetry of the electric field lines in the combdrives (due to the presence of the handle under the polarized electrode). A small Y displacement can also be seen. This can be due to two major reasons:

- The displacement of both actuators are not exactly the same.
- The sample was slightly tilted under the microscope.

To determine which of these two reasons is valid, the displacement difference between the two actuators was plotted. Figure 5.10 shows these values. A maximum of about half a micron is shown. This difference being within the error bars, it is not possible to conclude that there is a displacement difference between the two actuators. Thus, the small Y displacement shown in figure 5.9 should certainly be due to a bad alignment of the sample under the microscope. This is probable because a precise in-plane alignment is not easily done as it has to be carried out manually.

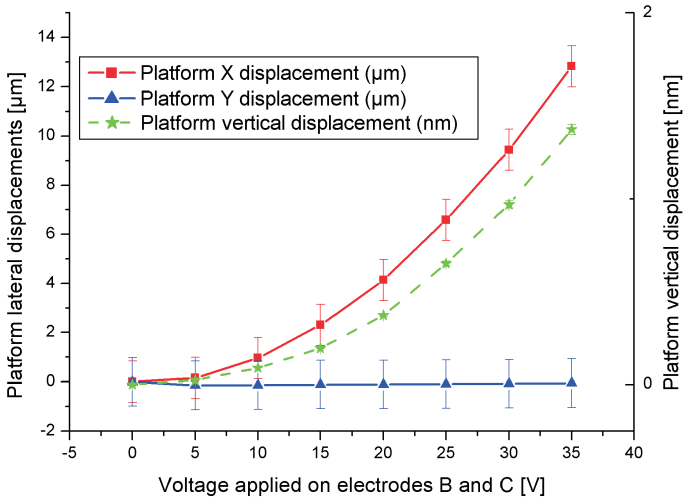

Figure 5.9: *Graph showing the measured displacement while the same voltage is applied on both actuators to move the platform in the X direction.*

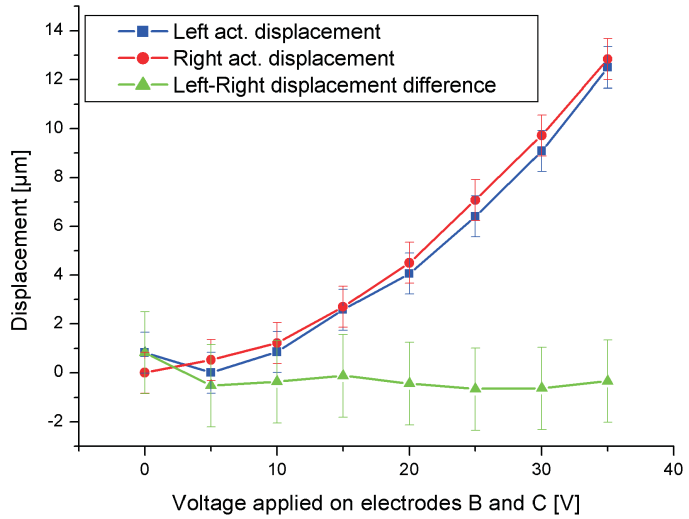

Figure 5.10: *Graph of the "X" displacement of both actuators and their displacement difference. The maximum difference shown is in the order of half a micrometer.*

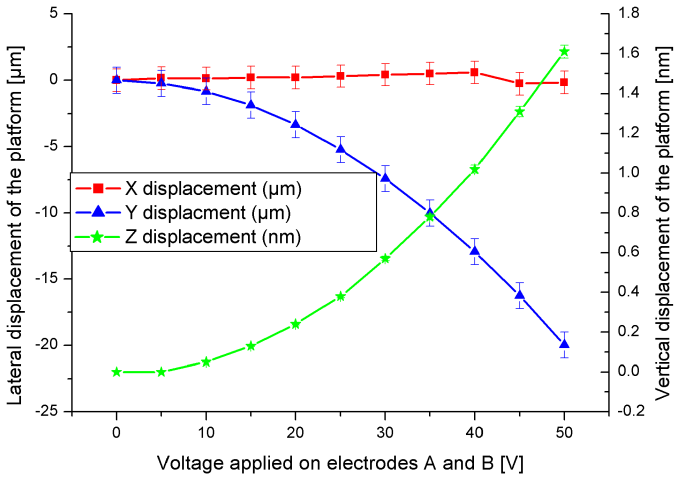

Figure 5.11: *Graph showing the measured displacement of the platform and one actuator while the same voltage is applied on both actuators A and B (Figure 3.9) to move the platform in the "-Y" direction.*

5.2.2 Movement parallel to the Y axis

The same type of measurement was performed by applying the same voltage on two actuators to move them in opposite directions. By pulling them apart, as seen in section 3.1.2, the platform moves along the Y axis as shown in figure 5.11.

As seen in section 3.3, the Y displacement of the platform is related to the variation of distance between the two actuators. Figure 5.12 shows the Y displacement of the platform as a function of the differential position of the side actuators. To determine the value of the ψ function obtained in section 3.3, a curve fit can be applied to the resulting points. This figure shows the results for two types of fit; a linear one and polynomial of second degree. Both fits are very close and even if the shape of the polynomial seems to be more precise than the linear one, both are comprising into the error bars.

Following this fit, the ψ function can be determined as following:

$$\psi(a) = -0.00455 \times *(a)^2 + 0.98261 \times (a) - 0.40438 \tag{5.4}$$

and as seen in section 3.3:

$$y_{\text{platform}} = \psi(x_2 - x_1) \tag{5.5}$$

$$y_{\text{platform}} \cong -0.004 \times (x_2 - x_1)^2 + 0.98 \times (x_2 - x_1) - 0.40 \tag{5.6}$$

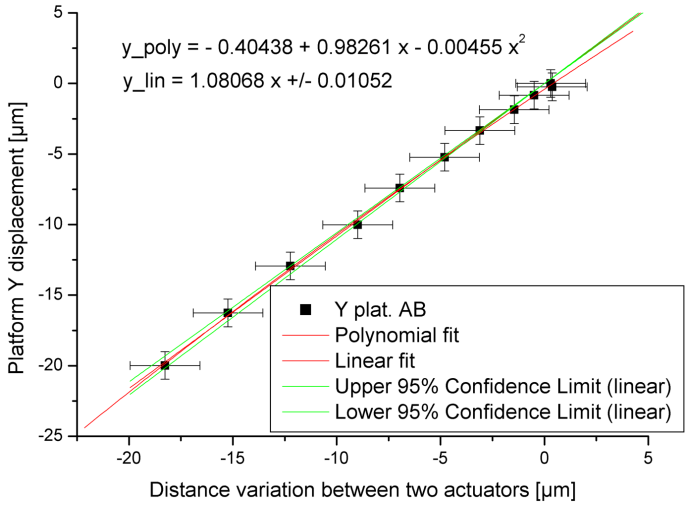

Figure 5.12: *Graph of the "Y" displacement of the platform as a function of the distance variation between the two actuators. The obtained results are fitted linearly and with a polygonal function of second order. In this graph the distance variation is calculated by subtracting the position of one actuator to the position of the second one.*

This result shows that the fitted function is almost linear with a slope of 1. This is confirmed by the linear fit of the data in figure 5.12, that gives a linear function with a slope of about 1. These results are in a very good agreement with the simulated ones. In the simulations, the relation in equation 3.11 shows that for one spring of the device, the displacement of the platform in the axis perpendicular to the actuator displacement is doubled. In the real case, to obtain a displacement in this vertical direction, both actuators have to move in opposite direction to create the reaction force implicitly created during the simulation. This means that if one actuator moves of a distance d, the other one has to perform the same displacement d to deform the beams and allow the platform to move in the orthogonal direction. Thus, the distance variation between the actuators will be $2d$, which corresponds to the distance $y = 2d$ traveled by the platform. It is then correct to get a measured linear relation with a factor of about 1.

5.2.3 Movement in the other directions

By combining different voltages on both sides, any XY displacement within the displacement area can be obtained. To show this, a displacement obtained with a variable voltage applied on one side and a nil signal applied

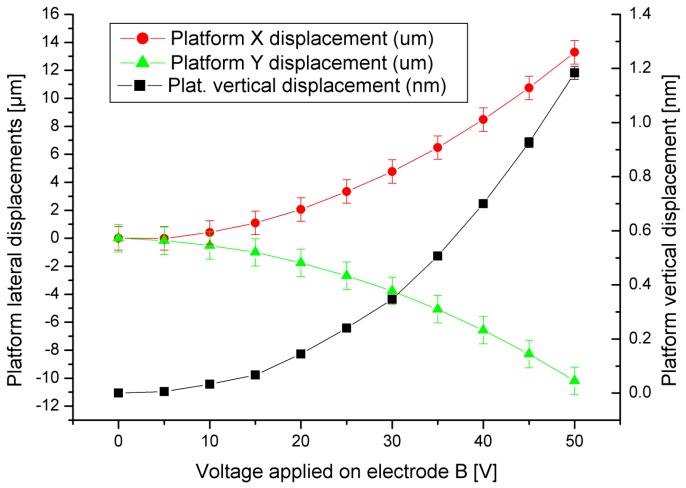

Figure 5.13: *Graph showing the measured displacement of the platform while a voltage is applied to only one electrode. In this case, electrode B (Figure 3.9).*

on the other electrode is shown in figure 5.13. It is then possible to compare these displacements with the functions and hypotheses set out in section 3.3. In figure 5.14, the Y displacement is plotted versus the position difference between the actuators. In this case, the displacement of the platform is the predicted one. In figure 5.15, the X position is plotted and compared to the mean value of the displacement of both actuators. It can also be seen that this corresponds with the expected behavior. In these graphs, one can clearly see that the displacement of the platform is:

- In X direction: the same than the mean position of the actuators.
- In Y direction: the same than the position variation between the actuators.

5.2.4 Maximal displacements

Maximal displacements analysis was performed. The platform is not stable enough to allow the combdrives to move with its full possible displacement range. This is depicted in figure 5.16. Due to the torsion forces created by the bending of the compliant suspension beams, after a certain motion range, the stabilisation springs are not strong enough to avoid the rotation of the structure supporting the combdrives. This results to a low rotation of the structure, creating a dissymetry of the electrostatic force in the combdrives and a side pull of these [143]. This phenomenon could be reduced by modifying the strength of the supporting springs but it was decided not to do it

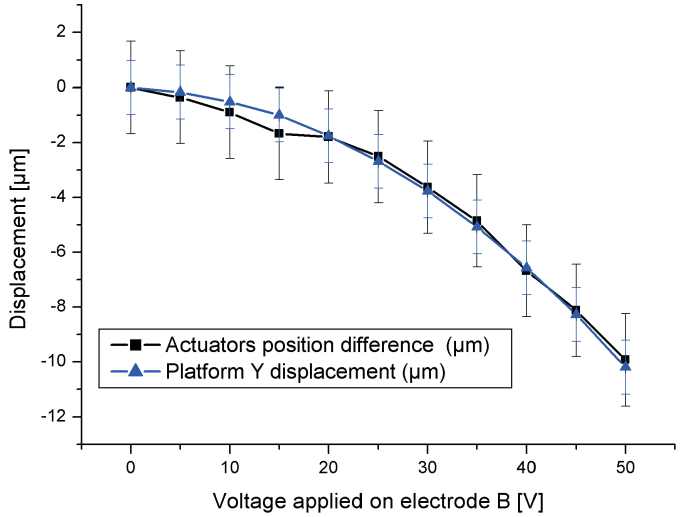

Figure 5.14: *Graph showing the "Y" displacement of the platform and the position difference between the left and right actuators versus the applied voltage. For this set of measurements, the signal is applied on electrode B (Figure 3.9).*

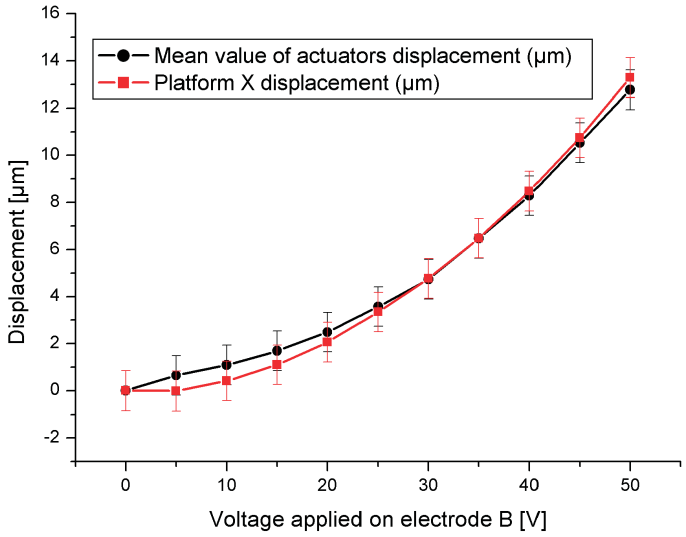

Figure 5.15: *Graph showing the "X" displacement of the platform and the mean position of the actuators versus the applied voltage on electrode B (Figure 3.9).*

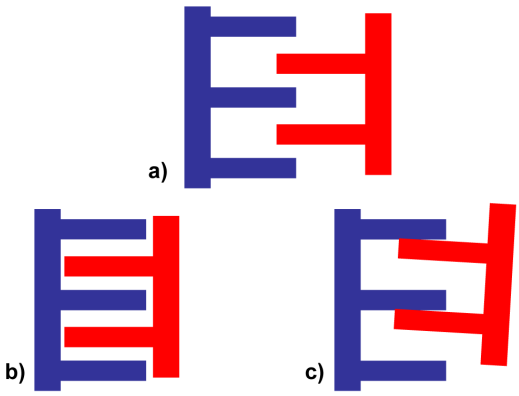

Figure 5.16: *Principle of side-pull of the combdrives actuator. a) Actuators at rest. b) Actuator moved to its full displacement range. c) Side-pull phenomenon occuring in the middle of the displacement range.*

because the displacement range was already large enough and, by increasing the springs stability, higher voltages actuation would have been needed.

The maximal displacements measurements were carried out by slowly increasing the voltage on each actuator independently. This is important to avoid the large overshoot of the platform displacement (visible in figure 5.19(a)). The position of the central platform was captured on a video file. Once the side-pull voltage reached, the position of the platform before the large and unpredictable displacement of the platform due to the side-pull was measured on the screen by overlaying a scale based on the pixel of the CCD camera. By using a large enough magnification objective, the precision of this measurement is in the micron range. Figure 5.17 shows the maximal displacements achieved with a device with springs and compliant beams width designed at 3.5 μm. Depending on the width of the springs, the displacements obtained are the same but corresponds to excitations with different amplitudes. It can be observed that the maximal displacement in the Y direction is much larger than in the X direction (about double). As the spring shape was chosen to obtain a displacement ratio of a factor of two between these two directions (Section 3.4.1), this larger Y displacement was predicted.

In the specifications, the required range of motion was 10 μm in one direction and 15 μm in the other. This graph (Figure 5.17) shows that the possible displacement is much larger than the required one.

It can also be seen that the Y displacement is not the same in the two directions. This was confirmed by further simulations performed on the springs. These showed that the spring design was more stable in compression (while

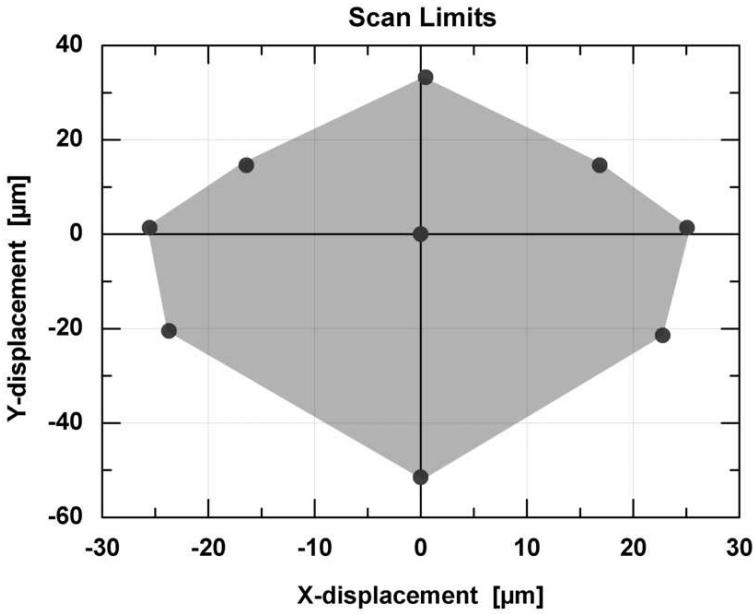

Figure 5.17: *Maximal displacements achieved with the scanning platform. This range of motion is much larger than the one required by the initial specs.*

moving the stage in the -Y direction) than in extension (corresponding to a displacement of the platform in the +Y direction). This can explain why the -Y displacement is larger than the +Y one.

5.2.5 Repeatability of the displacement

Figure 5.18 shows the displacement of the platform with the same voltage applied hundred times. Most of the measurements are within a range of less than half a micron. The other measures out of this range are due to pattern recognition software problems. This set of measurements was not performed with the last Matlab based developed algorithm and there was some bug due to very small variations on the intensity of light coming on the device. In case of a "bad" value, one can see on the data table obtained from the measurements that sometimes, the software does not recognize the right shape to be measured, what creates either a missing or a "wrong" value.

5.2.6 Full characterization of the platform's behavior

Automatized measurements were performed to receive information about the displacement of the actuator for each possible voltage pair. This was made

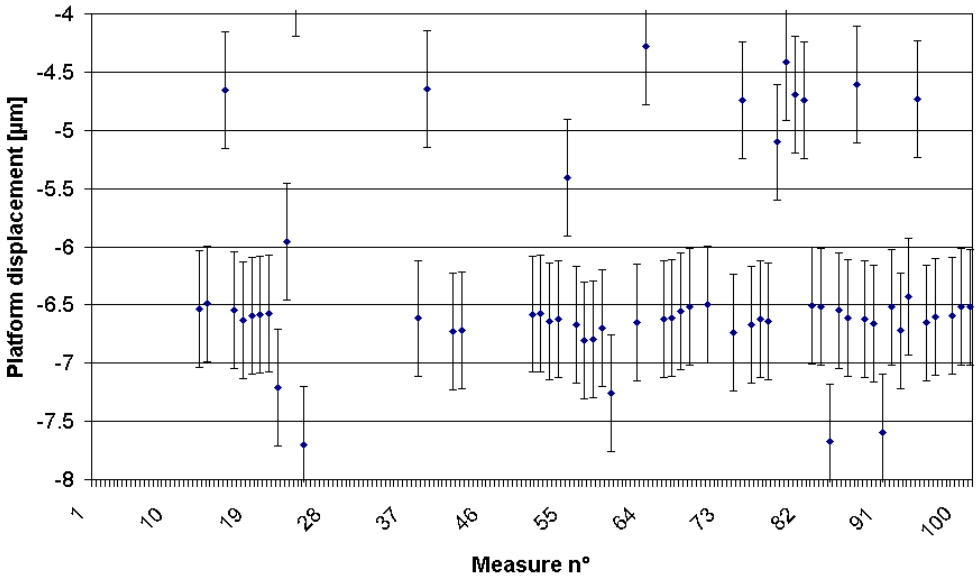

Figure 5.18: *Graph showing the repeatability of the displacements.*

by piloting the Wyko DMEMS white light interferometer with Matlab. A routine was then used to do a pattern recognition analysis of the obtained image and determine the position X, Y and Z of the platform for every voltage pair. Starting from this database, it is possible to know which voltage has to be applied to reach any point of the 2D plane. For the intended application, these information are not needed as a feed-back loop is used to maximize the coupling without need to know the precise position of the device. Nevertheless, it was interesting to perform this kind of analysis for other potential applications such as scanners or displays.

5.2.7 Dynamic measurements

Dynamic measurements were performed on the device. These gave us the possibility to calculate the resonance frequency of the actuator.

To carry out these measurements, the Wyko DMEMS white light interferometer was used. A square signal was applied to the device and a stroboscopic illumination synchronized with the camera was used. By choosing the phase offset between the signal generated and the illumination pulse, it was possible to visualise the device in position along its displacement. A scan every 2 degrees along the 360 degrees of phase was performed to get the full graph of the position of the platform along the voltage step. This measurement can be seen in figure 5.19(a). A square signal of 40 V with a duty cycle of 50 %

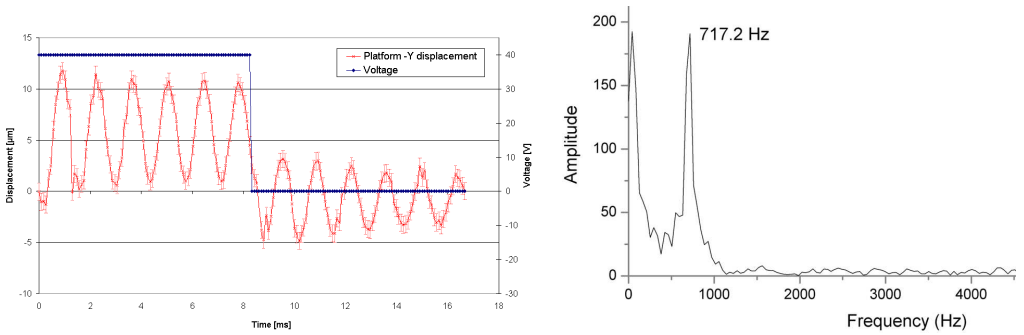

(a) (b)

Figure 5.19: *Measured step response in "-Y" direction (Figure 3.10) of a fabricated actuator. a) Measured displacement of the actuator and voltage applied on the combdrives. b) Fourier transform of the obtained step response showing a resonance peak at 717.2*Hz. *Excellent agreement with the simulated value of 695.03*Hz *(Figure 3.30).*

and a frequency of 60 Hz was applied to the two outer electrodes in order to create a displacement of the platform in the -Y axis. It can be seen that the damping is very low and the device is still vibrating when the voltage is turned on or off. To get a better idea of the damping factor, it would have been necessary to perform the same measurement with a lower actuation frequency. Unfortunately, this was not possible due to synchronization problems of the camera with the illumination at lower frequencies.

The determination of the resonance frequency was then performed by applying a Fourier transform (Figure 5.19(b)) to the step response of the actuator (Figure 5.19(a)). It gives a resonance frequency of 717.2 Hz. This value can be compared to the simulated value shown in figure 3.30 where the resonance frequency was 695.03 Hz. These results are in very good agreement, the error between the measured and the simulated value being about three percent.

5.3 Locking characterization

As explained in chapter 3.1.2, once the device is moved in the desired position, it can be locked in place. Two locking modes were experienced: the temporary locking and the permanent one. These different regimes can be shown in figure 5.20. This graph shows that the permanent locking occurs when a certain current flows between the movable platform and the handle of the chip.

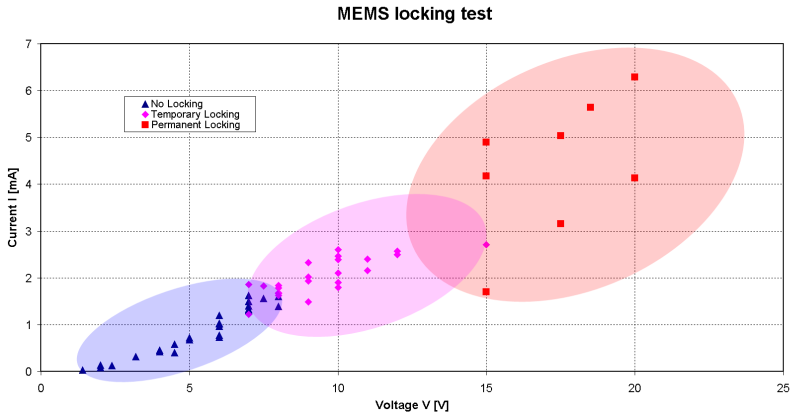

Figure 5.20: *Graph showing the results of locking test. At low current, temporary locking occur and for higher current permanent locking can be seen.*

5.3.1 Temporary locking

As seen in figure 5.20, if the current flowing between the platform and the handle is not large enough, no "bonding" phenomenon occurs. This means that as long as the locking voltage is applied, the platform stays in the same position independently of the voltages applied on the actuators but when the locking voltage is set back to zero, the platform goes back to its equilibrium position.

Concerning this locking regime, a very interesting phenomenon was observed: as an increasing voltage is applied between the movable structures and the handle, the platform moves towards the polarized handle. At a certain voltage, both parts are in contact (Figure 5.21). By comparing this graph with the measured current flowing through the interface, it can be seen that it is possible to have contact without current (Figure 5.21). This means that it is possible to keep the platform in place temporarily but with a very low energy consumption as the current flow is very low. As the voltage is further increased, the current increased consequently up to the permanent locking regime.

5.3.2 Permanent locking

In this case, if the current flowing through the interface is large enough, the surfaces in contact are locally "bonded" and the platform stays in the desired position even after the locking voltages is reset to zero. Various parameters play a role in this phenomenon:

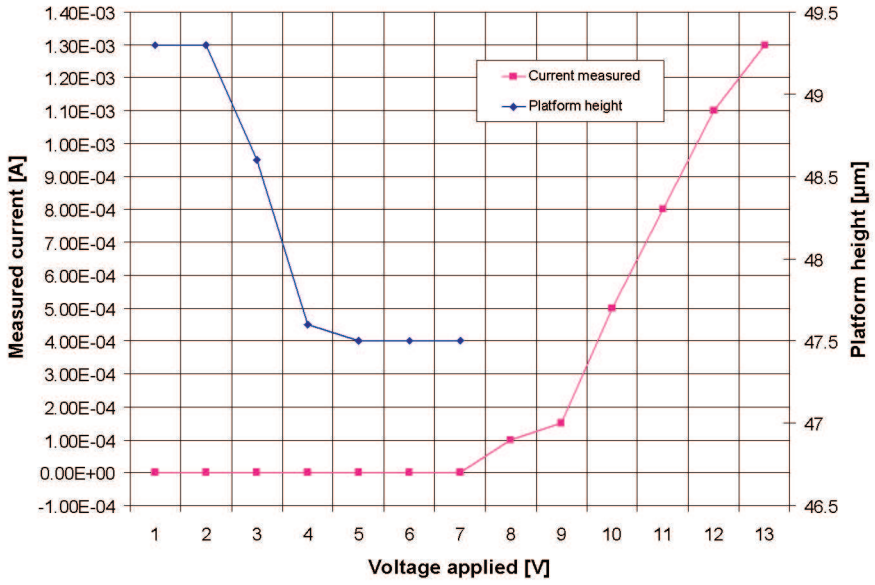

Figure 5.21: *Behavior of the device as a voltage ramp is applied between the movable platform and the handle of the chip. The blue curve shows the height of the platform versus the applied voltage. The red curve shows the measured current flowing through the device.*

- The current flowing between the electrodes.
- The duration of the applied signal.

The relation between the current (and the voltage) and the locking regime can be seen in figure 5.20. Several measurements were carried out with the same chip. Once it was locked, a mechanical release of the structure had to be performed. A prober needle was used to apply a shear force to the platform in order to release it. For large current applied, the platform was so strongly attached that it broke while it was displaced.

The duration of the applied signal is also an important parameter determining the locking regime. For a given current flowing through the interface, it is possible to get either a temporary or a permanent locking depending on the signal length. Figure 5.22 shows this time dependence. For example, if a current of 300 μA flows through the device, it will not be permanently locked for signal duration below five minutes. By increasing the signal length, a permanent locking can be observed. This figure also shows that the larger the current, the shorter the locking signal has to be applied.

To study the long term behavior of the locking, aging tests were completed. Once locked, a couple of chips were placed in a environment chamber creating large temperature variations. After standard aging cycles, all platforms were still locked in the same position than when the locking voltage was applied.

Basic shock tests were also performed on permanently locked devices. Once the platform held in place, chips were disconnected and dropping tests were carried out. After a drop of one meter the device withstood the shock of hitting a hard surface.

5.4 Optical measurements

Initial optical tests were performed with the second version of the actuator to show the feasibility of the concept of optimization of the coupling. Figure 5.23 shows the system tested. It is composed of a MEMS chip glued and wirebonded to a PCB with a quartz lens assembled on top. The device was driven by a simple Labview program to maximize the coupling of the light coming from a red laser into a multimode fiber. These first tests -even though the labview program was not optimized- showed the feasibility of the concept. Of course, as it was performed with visible light, a quartz lens and a multimode fiber, the result is not fully representative but it showed the possibility to steer light and inject it into an optical fiber.

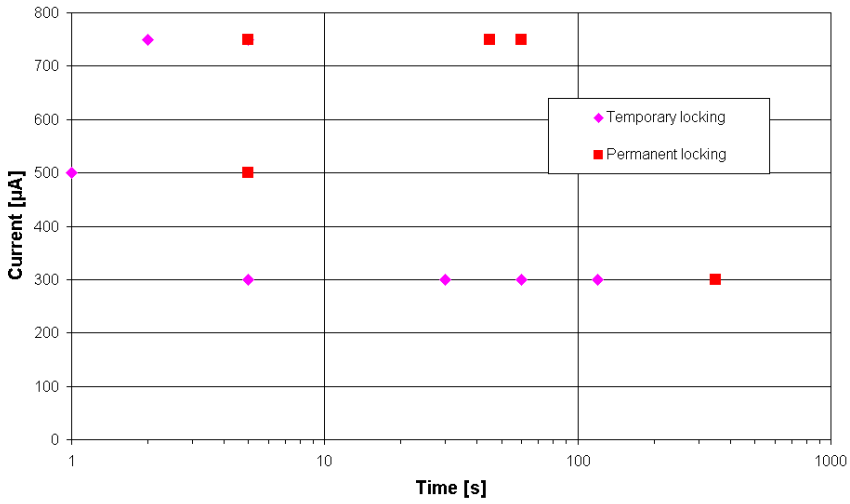

Figure 5.22: *Relation between the locking regime and the duration of the locking signal applied.*

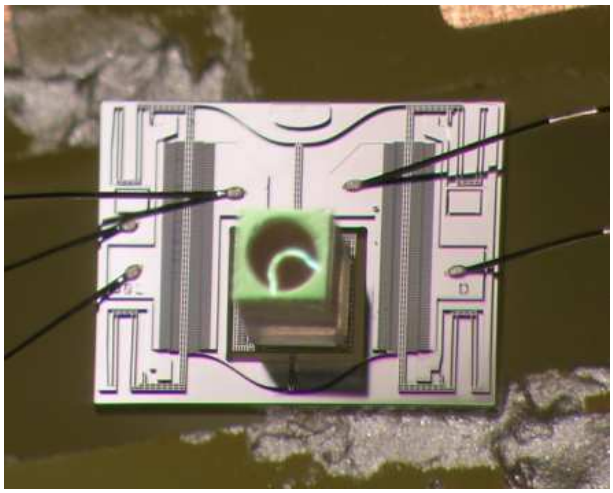

Figure 5.23: *Picture of a chip wirebonded to a PCB with a quartz lens assembled on top.*

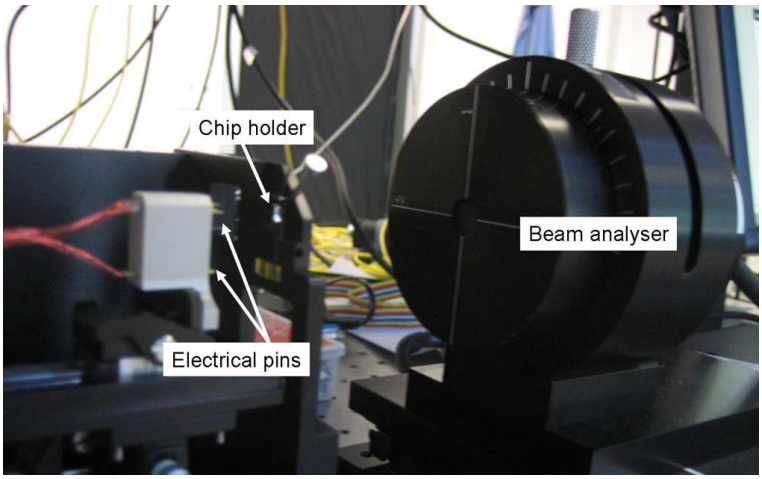

Figure 5.24: *Picture of the optical measurement setup.*

Further optical measurements were performed with the setup shown in figure 5.24. It is composed of a system that holds the assembled system as shown previously on figure 4.12(b) (chip holder), a movable holder containing electrical pins to contact the device and a beam analyzer. The latter is controlled by with a computer and synchronized with an algorithm allowing to calculate the position of the focusing point as well as the width of the beam at this point. An algorithm has to be used for that because this point cannot be measured as it is too close to the device and the mechanical parts of the setup does not allow the parts to come at that distance. The minimal gap between the device and the beam analyzer is of a couple of millimeters.

As the setup was not fully operational only partial characterization of the beam steering could be performed. The goal of these optical measurements was then to perform basic displacement characterization to have the possibility to compare the behavior of the MEMS before and after the packaging process described in section 4.4. For that, initial measurements were performed without applying any signal on the device to look at the shape of the optical beam. Then, the displacement of the light spot versus the driving voltage applied was measured.

5.4.1 Measurements at rest position

Figure 5.25 and 5.26 shows the beam coming from the laser diode assembled on the submount without applying any voltage on the MEMS device. These images show that in one direction (direction X), the beam presents a nice Gaussian shape but in the other direction (direction Y), the obtained beam

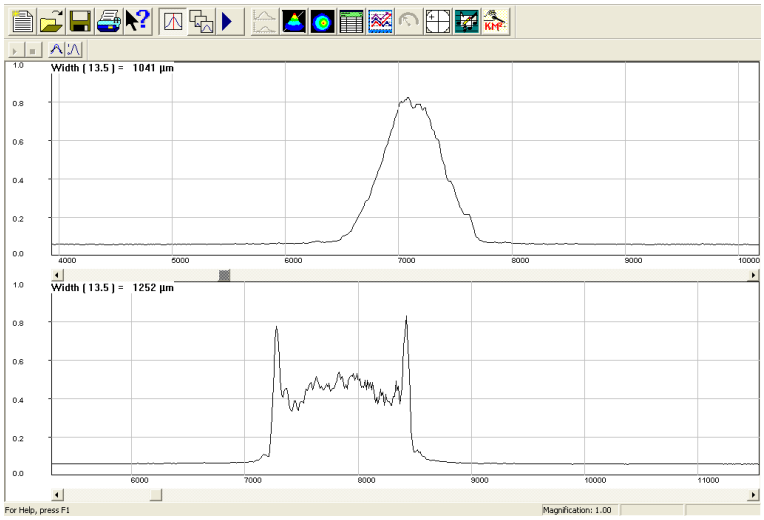

Figure 5.25: *Cut-off of the measured beam along the X and Y axis.*

shape is far from being Gaussian. This is due to the fact that the laser diode has a much larger numerical aperture along Y axis and at the lens level, the beam is wider than the lens. This phenomenon was predicted because the initial lens diameter should have been 600 μm, but the ones used during the assembly had a diameter of "only" 500 μm. With this beam shape, it is possible to determine quite precisely the position of the beam or its displacement, but it is barely impossible to determine its exact focusing point or width.

Table 5.1 shows measurements of the beam at various distances between the chip and the detector. From these, it is possible to measure the initial distance between the detector and the position of the focus as well as the shape and position of the beam while the MEMS chip is at rest. This will be done with a linear approximation of the divergence of the beam.

Working with a Gaussian beam, the focal depth of the lens should be taken into account. The beam opening angle θ cannot be determined in this range with a linear approximation. The depth of focus is twice the Rayleigh range:

$$2z_0 = \frac{2\pi W_0^2}{\lambda} \tag{5.7}$$

In the present case, the focal depth being much smaller than one millimeter, it is possible to use the linear approximation of the beam propagation. A schematic of the system is shown in figure 5.27.

To determine the distance between the focus and the beam analyzer (x,

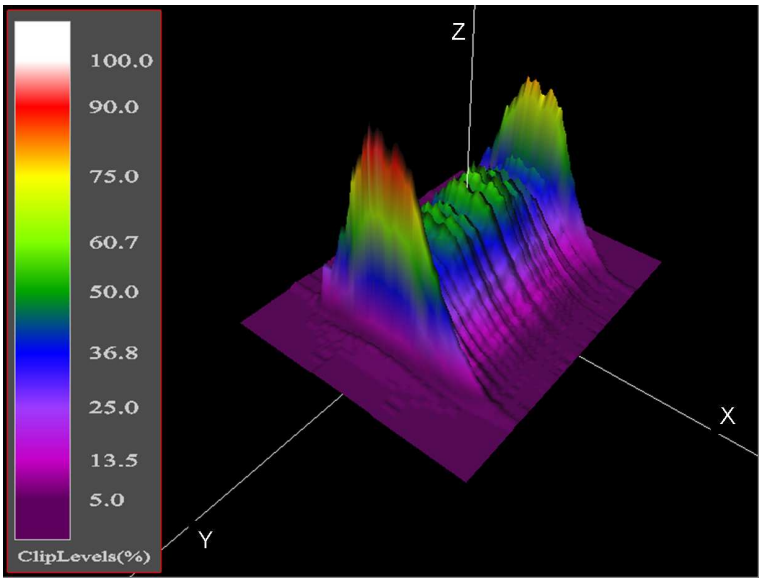

Figure 5.26: *3D image of the measured beam.*

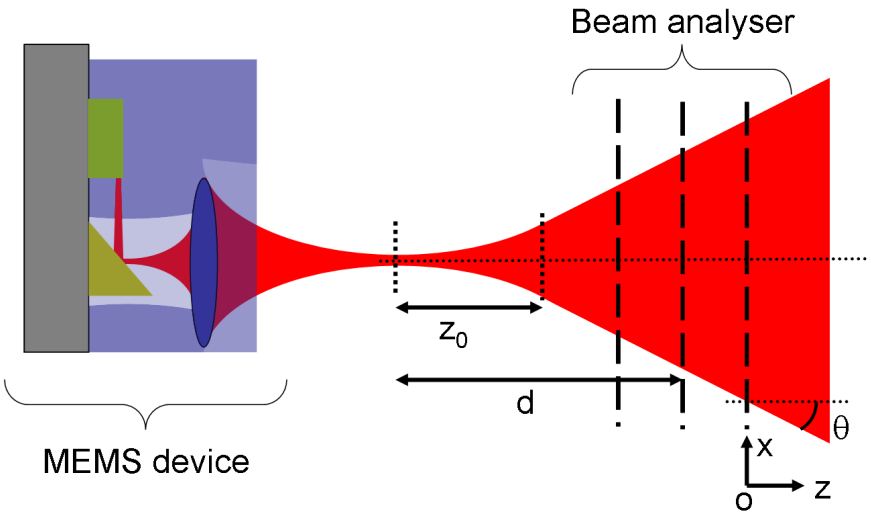

Figure 5.27: *Schematic of the analyzed beam. The measurements are performed far from the depth of focus limit. The origin on the optical axis is set at the furtherer measured point (o).*

Beam analyzer position μm	**Beam X position** μm	**Beam Y position** μm	**Beam X width (13%)** μm	**Beam Y width (13%)** μm
0	7561	7863	4752	5825
-2500	7490	7988	4142	4973
-5000	7352	8115	3378	4130
-7500	7247	8177	2651	3253
-10000	7145	8116	1926	2357
-11000	7106	8085	1645	1998
-12000	7063	8049	1354	1645
-12500	7045	8029	1226	1468

Table 5.1: *Beam size and position depending on the position of the beam analyzer.*

Figure 5.27), the angle θ should be first determined. This value was calculated for each measurement shown in table 5.1. As the beam did not change between the measurements, the obtained value should have been the same but quite different results were obtained. They are recapitulated in table 5.2.

This table shows that the calculation of the angle and the distance between the focus and the detector is not very reliable. By averaging the obtained values, the results are the following:

$$\bar{\theta} = 173.46 \pm 16.6\,\text{mrad} \tag{5.8}$$
$$\cong 10\,\text{degree} \tag{5.9}$$

From this mean value one can calculate the distance between the origin and the focal point:

$$Position\ of\ the\ focus = \frac{Beam\ width/2}{tan(\bar{\theta})} \tag{5.10}$$
$$= 16621\,\mu\text{m} \tag{5.11}$$
$$= 16.6\,\text{mm} \tag{5.12}$$

5.4.2 Measurements with applied voltages

Figure 5.28 shows the measured shape of the beam spot while the MEMS is at rest and the same measurement while a voltage is applied on one electrode of the chip. It can be clearly seen that the beam is displaced of a certain

Beam analyzer position measurement μm	**Beam angle** θ mrad	**Distance x** μm	**Position of the focus** μm
0	168.8	17092	17092
-2500	167	14747	17247
-5000	173.6	11773	16773
-7500	177.3	9076	16576
-10000	177.6	6565	16565
-11000	174.7	5660	16660
-12000	175.1	4646	16646
Meas on tot. dist.	172.5	16711	16711

Table 5.2: *Beam θ angle, d distance and focus position calculated depending on the position of the beam analyzer.*

distance. By applying a Gaussian fit to the measured curve, the center of the beam can be determined. Figure 5.29 and 5.30 shows the displacement of the center of the spot versus applied voltages on one actuator of the MEMS chip. Figure 5.29 shows the displacement of the light beam as a voltage is applied on only one actuator (in this case, actuator B) and figure 5.30 is a combination of the displacement of the beam as voltages are applied on electrodes D (negative voltages) and B (positive voltages).

For these measurements, the beam analyzer was positioned as close as possible to the MEMS device. Its position related to the moving stage origin (shown in figure 5.27) was 12.724 mm. The determination of the distance between the focus and the beam analyzer can be calculated with the value obtained in equation 5.12:

$$d_{\text{measurements}} \cong 3.987\,\text{mm} \tag{5.13}$$

5.5 Comparison with simulations and previous measurements

It is possible to compare the measurements with the simulated values and the measurements performed on a device without assembled lens. By plotting the optical measurements and the simulations results in the same graph, a good agreement of both (normalized) data sets can be observed (Figure 5.31). In this graph, the data had to be normalized to be compared because the

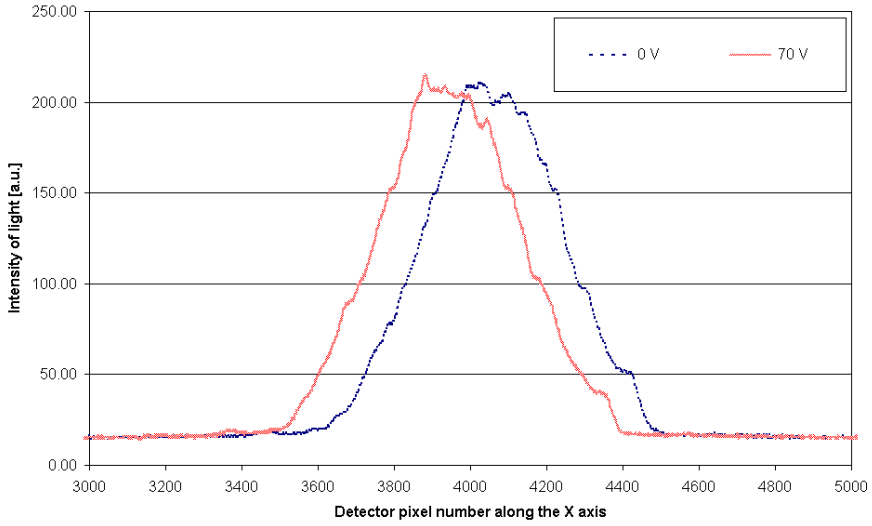

Figure 5.28: *Shape difference between the initial beam and the displaced one while a voltage is applied on electrode B (Figure 3.9).*

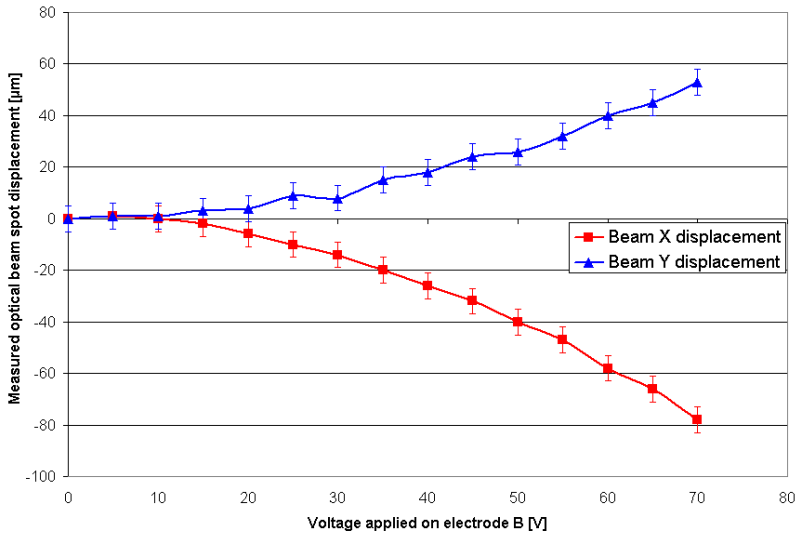

Figure 5.29: *Graphs showing the displacement of the light spot as different voltages are applied on electrode B (Figure 3.9).*

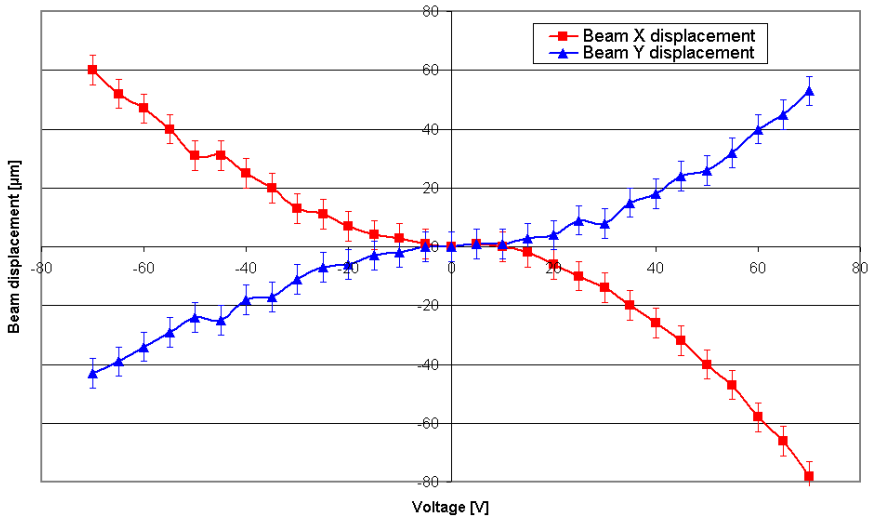

Figure 5.30: *Displacement of the light spot as different voltages are applied on both right actuators (push and pull). Graphically represented positive voltages corresponds to signal applied on electrode B and negative ones corresponds to signal applied on electrode D (Figure 3.9).*

measurement of the displacement of the optically steered beam is much larger than the displacement of the MEMS itself due to the magnification of the lens. It was also inverted because the image of the single lens optical system is inverted in the image plane. It can be seen that all these curves are very close even though the device was not in the same position during the measurement. For the optical measurement, not only a lens was assembled on the platform, but the position of the whole device was not the same. During the MEMS measurements, the latter was positioned in the horizontal position while it was in the vertical one for the optical experiments. This could have caused a difference in the results due to the gravitational force acting on the mass of the assembled lens but figure 5.31 shows that this is not the case and that the device is stable enough. Of course, the measurement setup was stable and it could be interesting to repeat these measurements in other positions and acceleration conditions.

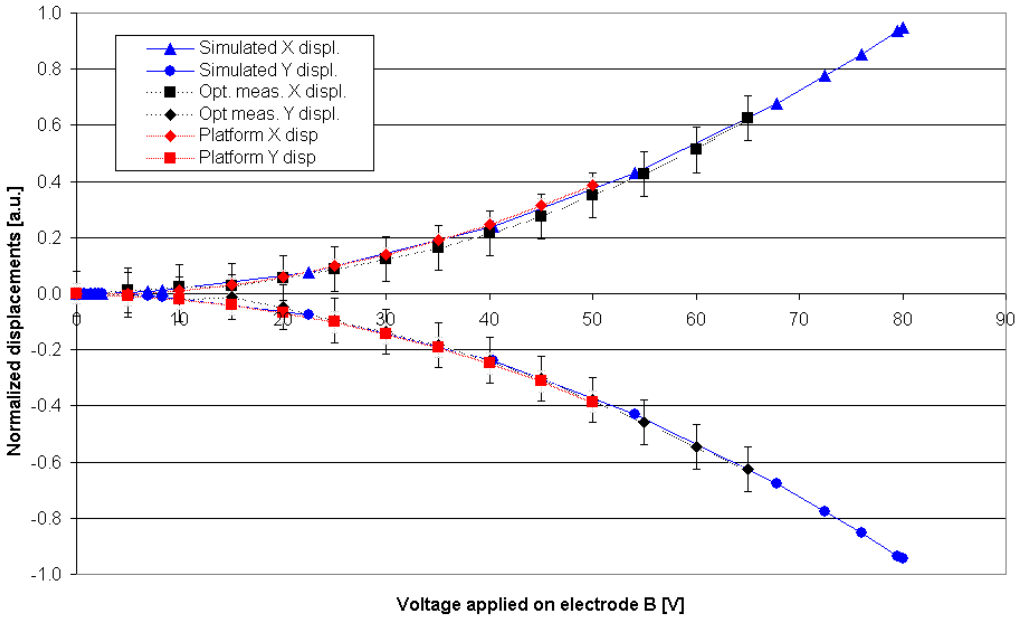

Figure 5.31: *Comparison between the simulated and measured platform displacements and optically measured beam steering (normalized).*

Chapter 6

Conclusion

Conclusion on the fabricated device

A 2D MEMS scanner for fiber coupling applications was developed, simulated and fabricated. A new process combining a double delay mask etching combined with gold metalizations on both sides of the wafer was developed. Characterization measurements such as locking, displacement and resonance frequency were performed on the device before assembly and they agree with the simulated ones. Concerning the resonance frequency, the difference between the measured and the simulated value is less than 3 %.

The MEMS was then assembled with the other elements of the system to obtain a fully packaged optical system containing MEMS, laser diode, microlens, electronic components and glass lid. Optical measurements were performed with such a full system and were compared to the previously simulated and measured characteristics of the MEMS actuator. A range of motion suitable for optical fiber coupling was achieved.

During the project, several improvements were made on the chip level to optimize its interfacing with the "macroscopic world". These main improvements were, but not limited to, the following: the size and shape of the chip, the position of the contact pads and their metalization, the added cavities on top and backside facilitating the assembly of the complete system and the position and shape of the platform on the chip. This was performed with success as it has been possible to assemble and test a complete system. The negative point is that with these modifications, the other components of the chip had to be also slightly modified depending on the process and the configuration of the optical system. Thus, when the chip was almost optimized for one configuration, it had to be re-optimized for the new arrangement. As a consequence, for the last design with the last configuration, the design

was not fully optimized. Nevertheless, it did work quite well but has some negative points:

- Its fragility. Although the system works without and with the assembled lens, the system, once assembled, is quite fragile and does not resists to large shocks or accelerations. For this reason some of the fully assembled device broke during testing due to device handling.
- Its process reliability. Even if most of the process challenges were solved, the process reliability has to be increased, the number of working chips being far from an eventual commercial product.
- The assembly precision. Despite the fact that we could assemble a couple of fully working systems, improvements have to be made in the assembly level. Steering of a light beam was shown but the precise alignment required in the direction parallel to the optical axis was certainly not as good as required. New assembly and characterization tools should be developed to ensure a better quality of the system assembly, especially for the alignment of the chip on the submount.

The major problem encountered to perform the final optical measurements did not come from the chip itself, nor from the lens to glue on top but from the small number of available submounts with diode and electronics assembled. Starting from the six pieces obtained, it was very difficult to get more than the three working systems we had at the end of the assembly process.

Outlook

The major improvements to be done to develop further the system will be on three sides.

First, tools to assemble the MEMS actuator on the submount chip have to be developed. With the assembly setup used for the first prototypes, it is rather impossible to get a reasonable yield and a good precision reproducibility.

Second, the reliability of the process has to be increased, especially during the vapor phase etching step to avoid the metalization to peel-off, phenomenon observed on several chips while taking them out of a "GelPack", for example.

Finally, the shock resistance of the MEMS has to be increased. This can be done with designing slightly thicker beams and springs. Of course, in this case, the actuation voltage needed will increase, but the current required

voltage is much below the limit given in the specs. Tests have to be done to see if in this case, the locking mechanism will work the same way but it should not be a problem regarding the tests performed with the previous version of the MEMS.

Bibliography

[1] A.M. Hynes, H. Ashraf, J.K. Bhardwaj, J. Hopkins I. Johnston, and J.N. Shepherd. Recent advances in silicon etching for mems using the ase process. *Sensors and Actuators*, 74:13–17, 1999.

[2] T. Overstolz, P.A. Clerc, W. Noell, M. Zickar, and N.F. de Rooij. A clean wafer-scale chip release process without dicing based on vapor phase etching. In IEEE, editor, *MEMS 2004*, pages 717–720, Maastricht, 2004.

[3] Ph. Nussbaum, R. Völkel, H.P. Herzig, M. Eisner, and S. Haselbeck. Design, fabrication and testing of microlens arrays for sensors and microsystems. *Pure Appl. Opt.*, 6:617–636, 1997.

[4] C. Lamb and M. Zecchino. *WYKO Surface Profilers Technical Reference Manual*. Veeco Metrology Group, September 1999. Version 2.2.1.

[5] M. Madou. *Fundamentals of Microfabrication*. CRC, 1997.

[6] Wikipedia. Transceiver. http://en.wikipedia.org/wiki/Transceiver.

[7] R. Rubenstein. Regenerators get ready for 40g. *Fibre Systems Europe*, pages 22–23, April 2006.

[8] K.S. Mobarhan, S. Jang, and R. Heyley. Laser diode packaging technology: 980 nm edfa pump lasers for telecommunication applications. Application note, Newport, 1791 Deere Avenue, Irvine, CA 92606, February 2000.

[9] Y.-A. Peter, H.P. Herzig, and S. Bottinelli. Optical fiber switching device with active alignment. Report, University of Neuchâtel, Institute of Microtechnology, rue A.-L. Breguet 2, CH-2000 Neuchâtel, Switzerland, November 2003.

[10] P. Shah. Post weld disturbance analysis in laser diode assemblies. Report, May 2003. http://www.sjsu.edu/faculty/selvaduray/page/ papers/mate234/parenshah.pdf.

[11] Adept Technology, Inc, Livermore, CA. *Adept NanoStage L1P2: High-speed alignment tools for fiber optics*, April 2002.

[12] Govind P. Agrawal. *Fiber-Optic Communication Systems*. Wiley Interscience, 2002.

[13] Z. W. Zhong, S. C. Lim, and A. Asundi. Effects of thermaly induced optical fiber shifts in v-groove arrays for optical mems. *Microelectronics Journal*, 36:109–113, 2005.

[14] M. Hoffmann, S. Dickhut, and E. Voges. Silicon fibre ribbon pigtail with rhombus-shaped fibre and integrated photodiodes. In *MOEMS*, 1999.

[15] P. P. Deimel. Micromachining processes and structures in micro-optics and optoelectronics. *Journal of Micromechanics and Microengineering*, 1:199–222, 1991.

[16] Y. Pétremand, P.-A. Clerc, M. Epitaux, R. Hauffe, W. Noell, and N.F. de Rooij. Optical beam steering using a 2d mems scanner. In Y. Bellouard, Y. Otani, and K. S. Moon, editors, *Optomechatronic Actuators and Manipulation III, Proc. of SPIE*, volume 6715. SPIE, 2007.

[17] M. Murakawa, H. Nosato, and T. Higuchi. Automatic optical fiber alignment system using genetic algorithms. Report, Nat. Institute of Advanced Industrial Science and Technology (AIST), Tsukuba Central, Tsukuba, Ibaraki, Japan, September 2003.

[18] Newport. *Fiber Auto-Alignment System*, September 2002.

[19] EXFO Electro-Optical Engineering Inc. *Photonics Alignment system TWS-1000*, March 2003.

[20] Richard R.A. Syms and D.F. Moore. Optical mems for telecom. *Materials today*, pages 26–35, 2002.

[21] J.W. Osenbach, M.F. Dautartas, I. Pitman, C. Nijander, M. Brady, R.K. Schlenker, T. Brtrie, S.P. Scrak, B.S. Auker, D. Kern, S. Salko, D. Rinaudo, C. Whitcraft, and J.F. Dormer. Low colt/high volume laser modiles using silicon optical bench technology. *Electronic Components and Technology Conference*, pages 581–587, 1998.

[22] Richard R.A. Syms. Scaling laws for mems mirror-rotation optical cross connect switches. *J. of Lightwave Technology*, 20(7):1084–1094, July 2002.

[23] B. Pezeshki, E. Vail, J. Kubicky, G. Yoffe, S. Zou, J. Heanue, P. Epp, S. Rishton, D. Ton, B. Faraji, M. Emmanuel, X. Hong, M. Sherback, V. Agrawal, C. Chipman, and T. Razazan. 20-mw widely tunable laser module using dfb array and mems selection. *IEEE Photonics Technology Letters*, 14(10):1457–1459, October 2002.

[24] M. Epitaux, Y. Pétremand, W. Noell, N. De Rooij, and J.-M. Verdiell. Micro-machined xy stage for fiber optics module alignment. In *Optical Fiber Communications Conference Technical Digest 2005*, volume 4. IEEE, 2005.

[25] Y. Pétremand, W. Noell, M. Epitaux, J.-M. Verdiell, and N.-F. de Rooij. Post assembly alignment system. In *10th International Commercialization of Micro and Nano Systems Conference*, pages 477–481. MANCEF COMS, August 2005.

[26] H. Toshiyoshi, G.-D. J. Su, J. LaCosse, and M. C. Wu. Surface micromachined 2d lens scanner array. In *Optical MEMS Conference*, Sheraton Kauai Resort, Kauai, Hawaii, August 2003. IEEE/LEOS.

[27] H. Toshiyoshi, G.-D. J. Su, J. LaCosse, and M. C. Wu. A surface micromachined optical scanner array using photoresist lens fabricated by a thermal reflow process. *J. of Lightwave Technology*, 21(7):1700–1708, 2003.

[28] K. Takahashi, K. Saruta, M. Mita, H. Fujita, and H. Toshiyoshi. An optical lens scanner with electrostatic comb drive xy-stage. In IEEE/LEOS, editor, *Optical MEMS 2004*, pages 56–57, Takamatsu, Japan, 2004.

[29] C.-H. Kim, H.-M. Jeong, J.-U. Jeon, and Y.-K Kim. Silicon micro xy-stage with a large area shuttle and no-etching holes for spm-based data storage. *Journal of Microelectromechanical Systems*, 12(4):470–478, 2003.

[30] C. Ataman and H. Urey. Modeling and characterization of comb-actuated resonant microscanners. *Journal of Micromechanics and Microengineering*, 16:9–16, 2006.

[31] G.-D. J. Su, H. Toshiyoshi, and M. C. Wu. Surface-micromachined 2-d optical scanners with high-performance single-crystalline silicon micromirrors. *Photonics Technology Letters*, 13(6):606–608, 2001.

[32] H. Toshiyoshi. Design strategy for mems 2d scanning mirrors. Presentation at Optical MEMS 2001, September 2001.

[33] Philip J. Bos. Liquid cristal based optical phased array for steering lasers, 2001.

[34] Dr. Philip J. Bos. Beam steering, 2002.

[35] Boulder Nonlinear Systems, 450 Courtney Way, Lafayette, Colorado. *1x4096 Multi-level/Analog Liquid Crystal Spatial Light Modulator.*, January 2003.

[36] Beam steering using liquid crystals. Technical report, Boulder Nonlinear Systems, 450 Courtney Way Lafayette, Colorado, May 2001.

[37] R. Legtenberg, A. W. Groeneveld, and M. Elwenspoek. Comb-drive actuators for large displacements. *Journal of Micromechanics and Microengineering*, 6:320–329, 1996.

[38] W. Dai, K. Lian, and W. Wang. Design and fabrication of a su-8 based electrostatic microactuator. *Microsystem Technologies*, 13(3-4):271–277, 2007.

[39] H. Toshiyoshi. Iii. microactuators and micromechanism. Optical MEMS Course, 2000.

[40] S.-A. Zhou. On forces in microelectromechanical systems. *Int. J. of Engineering Science*, 41:313–335, 2003.

[41] E. Thielicke and E. Obermeier. Microactuators and their technologies. *Mechatronics*, 10:431–455, 2000.

[42] H.-Y. Shu, S.-W. Lee, and W. Fang. Design and fabrication of multi-degrees-of-freedom single crystal silicon moveable platforms on soi wafer. In *Transducers'05*, pages 737–740, Seoul, June 2005. IEEE.

[43] T. Shigematsu, T. Iseki, M. Okumura, T. Sugawara, and M. K. Kurosawa. Optical beam steering using 2-d surface acoustic wave actuator. In *Transducers'05*, pages 1255–1258, Seoul, June 2005. IEEE.

[44] A. Garnier, T. Bourouina, H. Fujita, T. Hiramoto, E. Orsier, and J.-C. Peuzin. Magnetic actuation of bending and torsional vibrations for 2d optical-scanner application. *Sensors and Actuators A*, 84:156–160, 2000.

[45] J. M. Maloney, D. S. Schreiber, and D. L. DeVoe. Large-force electrothermal linear micromotors. *Journal of Micromechanics and Microengineering*, 14:226–234, 2004.

[46] W.-J. Cheng and D.L. DeVoe. Linear micromotors and spatial micromechanisms based on uv-liga. In *IEEE International MEMS 2005 Conference*, pages 399–402, Miami, 2005. IEEE.

[47] N. Chronis, M. Okandan, M. Baker, and L.P. Lee. A 2-d translational pinhole formed by two orthogonally moving micro-slits. In *Transducers'05*, pages 1022–1025, Seoul, June 2005. IEEE.

[48] G.S.P. Castle. Industrial applications of electrostatics: the past, present and future. *J. of electrostatics*, 51-52:1–7, 2001.

[49] M. Mita, H. Toshiyoshi, and H. Fujita. An electrostatic inertia-driven micro rover. In *MEMS*, pages 395–398, Miami, January 2005. IEEE.

[50] E. Sarajlic, E. Berenschot, H. Fujita, G. Krijnen, and M. Elwenspoek. Bidirectional electrostatic linear shuffle motor with two degrees of freedom. In *MEMS*, pages 391–394, Miami, January 2005. IEEE.

[51] A.-S. Rollier, B. Legrand, D. Collard, and L. Buchaillot. The stability and pull-in voltage of electrostatic parallel-plate actuators in liquid solutions. *Journal of Micromechanics and Microengineering*, 16:794–801, 2006.

[52] F. Chen, H. Xie, and G. K. Fedder. A mems-based monolithic electrostatic microactuator for ultra-low magnetic disk head fly height control. *IEEE Transactions on Magnetics*, 37(04):1915–1918, July 2001.

[53] G. K. Ananthasuresh. Lecture 6 analysis of electrostatically actuated micro devices. Short course, Aug.-Sep. 2003. IISc, Bangalore.

[54] J. I. Seeger and B. E. Boser. Parralel-plate driven oscillatins and resonant pull-in. In *Solid-State Sensor, Actuator and Microsystems Workshop*, pages 313–316, Hilton Head Island, South Carolina, June 2002.

[55] J. Cheng, J. Zhe, and X. Wu. Analytical and finite element model pull-in study of rigid and deformable electrostatic microactuators. *Journal of Micromechanics and Microengineering*, 14:57–68, 2004.

[56] J. I. Seeger and B. E. Boser. Dynamics and control of parallel-plate actuators beyond the electrostatic instability. In *Transducers '99, The 10th International Conference on Solid-State Sensors and Actuators*, pages 474–477, Sendai, Japan, June 1999.

[57] C.-L. Dai, K. Yen, and P.-Z. Chang. Applied electrostatic parallelogram actuators for microwave switches using the standard cmos process. *Journal of Micromechanics and Microengineering*, 11:697–702, 2001.

[58] N. Takeshima, K.J. Gabriel, M. Ozaki, J. Takahashi, H. Horiguchi, and H. Fujita. Electrostatic parallelogram actuator. In *IEEE*, pages 63–66, 1991.

[59] H. N. Kwon, J.-H. Lee, K. Takahashi, and H. Toshiyoshi. Optical characterization of 9 x 9 optical cross connect utilizing silicon lens scanners with spider-leg actuators. In Bishnu Gogoi Hakan Urey, David Dickensheets, editor, *MOEMS Display, Imaging and Miniaturized Microsysteml IV, Proc. of SPIE*, volume 6114, 2006.

[60] V.P. Jaecklin, C. Linder, N.F. de Rooij, and J.M. Moret. Micromechanical comb actuators with low driving voltage. *Journal of Micromechanics and Microengineering*, 2:250–255, 1992.

[61] R. Toda and E.-H. Yang. Development of latching type large vertical-travel microactuator. In *IPAC2005-73390*, pages 1–5, San Francisco, California, July 2005. ASME InterPACK'05.

[62] P.-F. Indermühle, V.P. Jaecklin, J. Brugger, C. Linder, N.F. de Rooij, and M. Binggeli. Afm imaging with an xy-micropositioner with integrated tip. *Sensors and Actuators*, (A 46-47):562–565, 1995.

[63] V. Milanovic, G.A. Matus, and D. T. McCormick. Tip-tilt-piston actuators for high fill-factor micromirror arrays. In *Solid-State Sensor, Actuator and Microsystems Workshop*, pages 232–237, Hilton Head Island, South Carolina, June 2004.

[64] W.A. Moussa, H. Ahmed, W. Badawy, and M. Moussa. Investigating the reliability of electrostatic comb-drive actuators utilized in microfluidic and space systems using finite element analysis. Report, University of Alberta, Dpt of Mechanical Eng., December 2000.

[65] D. L. Odell and J. M. Porter. Microrobot conveyance and propulsion system using comb drive and parallel plate actuators: The scuttlebot.

[66] N. P. Pham, J. N. Burghartz, and P. M. Sarro. Spray coating of photoresist for pattern transfer on high topography surfaces. *Journal of Micromechanics and Microengineering*, 15:691–697, 2005.

[67] S.M. Sze. *Semiconductor Devices*. John Wiley and Sons, 1985.

[68] J.T. Nee. *Hybrid Surface-/Bulk-Micromachining Process for Scanning Micro-Optical Components.* PhD thesis, University of California, Berkeley, 2001.

[69] S. Warren, A. Reitzle, A.Kazimirov, J.C. Ziegler, O. Bunk, L.X. Cao, F.U. Renner, D.M. Kolb, M.J.Bedzyk, and J. Zegenhagen. A structure study of the electroless deposition of au on si(111):h. *Elsevier*, (496):287–298, 2002.

[70] H. Honoma. Plating technology for electronics packaging. *Electrochimica Acta*, 47:75–84, 2001.

[71] A. J. G. Strandjord, S. Popelar, and C. Jauernig. Interconnecting to aluminum- and copper-based semiconductors (electroless-nickel/gold for solder bumping and wire bonding). *Microelectronics Reliability*, 42:265–283, 2002.

[72] C.R. Marxer. *Silicon Micromechanics for applications in fiber optic communication.* PhD thesis, University of Neuchâtel, 1997.

[73] C.R. Marxer. A variable optical attenuator based on silicon micromechanics. *IEEE Photonics Technology Letters*, 11(2):233–235, 1999.

[74] Stanford Nanofabrication Facility. Lift-off process. Webpage, August 2003.

[75] W. Lang. Silicon microstructuring technology. *Material science and engineering*, R 17:1–55, 1996.

[76] U. Lang. Intracellular probe device. Master's thesis, Institut für Mikrostrukturtechnik, Universität Karlsruhe (TH), 1999.

[77] P.J. French. Integration of silicon mems devices: Materials and processing considerations. *Smart Materials Bulletin*, pages 7–13, January 2001.

[78] Y.X. Li, M.R. Wolffenbuttel, P.J. French, M. Laros, P.M. Sarro, and R.F.Wolffenbuttel. Reactive ion etching (rie) techniques for micromachining applications. *Sensors and Actuators*, 41(1-3):317–323, 1994.

[79] L. Mueller, R.T. Howe, and A.P.Pisano. High-aspect-ratio, molded microstructures with electrical isolation and embedded interconnects. *Microsystems Technologies*, 7:47–54, 2001.

[80] K. Richter, M. Orfert, and H. Schührer. Variation of etch profile and surface properties during patterning of silicon substrates. *Surface and Coatings Technology*, 142 -144:797–802, 2001.

[81] E. Sarajlic, E. Berenschot, G. Krijnen, and M. Elwenspoek. Versatile trench isolation technology for the fabrication of microactuators. *Microelectronic Engineering*, 67-68:430–437, 2003.

[82] S.-S. Yun, S.-K. You, and J.-H. Lee. Fabrication of vertical optical plane using drie and koh crystalline etching of (110) si wafer. In *Optical MEMS 2004 Conference*, pages 128–129, Takamatsu, Kagawa, Japan, August 2004. IEEE.

[83] D. Zhang, Z. Li, T. Li, and G. Wu. A novel isolation technology in bulk micromachining using deep reactive ion etching and a polysilicon refill. *J. Micromech. Microeng.*, 11:13–19, 2001.

[84] F. Laermer and A. Schilp. Method of anisotropically etching silicon. US Patent Nr. 5501893, March 26 1996.

[85] J. Bhardwaj, H. Ashraf, and A. McQuarrie. Dry silicon etching for mems. volume Symposium on Microstructures and Microfabricated Systems. Electrochemical Society, Montreal, May 1997.

[86] F. Laermer and A. Urban. Challenges, developments and applications of silicon deep reactive ion etching. *Microelectronic Engineering*, 67-68:349–355, 2003.

[87] GmbH Protron Mikrotechnik. High aspect ratio etching., February 2005.

[88] T.F. Hill. Analysis of drie uniformity for microelectromechanical systems. B.s. report, University of Illinois, 2001.

[89] R. Lengtenberg, H. Jansen, M. de Boer, and M. Elwenspoek. Anisotropic reactive ion etching of silicon using $sf_6/o_2/chf_3$ gaz mixtures. *Electrochemical Society*, 142(6), 1995.

[90] L. Haobing and F. Chollet. Layout design rules for one-step dry release and non-stiction wet release of mems using drie/soi technology. In *Transducers'05*, pages 1384–1387, Seoul, June 2005. IEEE.

[91] J.-Y. Lee, S.-H. Kim, H.-T. Lim, C.-H. Kim, C.-W. Baek, and Y.-K. Kim. Electric spring modeling for a comb actuator deformed by the footing effect in deep reactive ion etching. *Journal of Micromechanics and Microengineering*, 13(13):72–79, 2003.

[92] M. Zickar. *MEMS based Optical Cross Connects for Fiber Optical Communication*. PhD thesis, University of Neuchatel, 2006.

[93] E. Sarajlic, M.J. de Boer, H.V. Jansen, N. Arnal, M. Puech, G Krijnen, and M. Elwenspoek. Bulk micromachining technology for fabrication of two-level mems in standard silicon substrate. In *Transducers'05*, pages 1404–1405, Seoul, June 2005. IEEE.

[94] I. Zubel. Silicon anisotropic etching in alkaline solutions iii: On the possibility of spatial structures forming in the course of si(100) anisotropic etching in koh and koh + ipa solutions. *Sensors and Actuators*, 84:116–125, 2000.

[95] I. Zubel. Silicon anisotropic etching in alkaline solutions ii. on the influence of anisotropy on the smoothness of etched surfaces. *Sensors and Actuators*, A 70:260–268, 1998.

[96] I. Zubel and I. Barycka. Silicon anisotropic etching in alkaline solutions i. the geometric description of figures developed under etching si(100) in various solutions. *Sensors and Actuators*, A 70:250–259, 1998.

[97] K. Yu, D. Lee, U. Krishnamoorthy, N. Park, and O. Solgaard. Micromachined fourier transform spectrometer on silicon optical bench platform. In *Transducers'05*, pages 1250–1254, Seoul, June 2005. IEEE.

[98] D. Hah, C.-A. Choi, C.-K. Kim, and C.-H. Jun. A self-aligned vertical comb-drive actuator on an soi wafer for a 2d scanning micromirror. *J. of Micromechanics and Microengineering*, 14:1148–1156, 2004.

[99] J. Bühler, F.-P. Steiner, and H. Baltes. Silicon dioxide sacrificial layer etching in surface micromachining. *J. Micromech. Microeng.*, 7:R1–R13, 1997.

[100] S. Frédérico, C. Hilbert, R. Fritschi, P. Flückiger, P. Renaud, and A.M. Ionescu. Silicon sacrificial layer dry etching (sslde) for free-standing rf

mems architectures. Report, Swiss Federal Institute of Technology Lausanne, EPFL, CH-1015 Lausanne, 2002.

[101] A. Witvrouw, B. Du Bois, P. De Moor, A. Verbist, C. Van Hoof, H. Bender, and K. Baert. A comparizon between wet hf etching and vapor hf etching for sacrificial oxide removal. Technical report, IMEC, Belgium, August 2000.

[102] J. Anguita and F. Briones. HF/ H_2O vapor etching of SiO_2 sacrificial layer for large-area surface-micromachined membranes. *Sensors and Actuators*, A 64:247–251, 1998.

[103] W. I. Jang, C. A. Choi, M. L. Lee, C. H. Jun, and Y. T. Kim. Fabricaton of mems devices by using anhydrous hf gas-phase etching with alcoholic vapor. *Journal of Micromechanics and Microengineering*, 12:297–306, 2002.

[104] O. Solgaard and K.S.J. Pister. Optical mems in communication and sensing. Course overview, June 2003.

[105] H. Toshiyoshi. Mems graphic library, April 1999.

[106] O. Manzardo, H. P. Herzig, C. R. Marxer, and N. F. de Rooij. Miniaturized time-scanning fourier transform spectrometer based on silicon technology. *Optics Letters*, 24(23):1705–1707, 1999.

[107] K. R. Cochran, L. Fan, and D. L. DeVoe. Moving reflector rype micro optical switch for high-power transfer in a mims-based safety and arming system. *Journal of Micromechanics and Microengineering*, 14:138–146, 2004.

[108] S. Ide, K. Mori, T. Akashi, Y. Sakai, T. Yamabana, Y. Ishii, O. Tsuboi, and M. Kawai. High-speed 80x80 mems optical switch module with voa., November 2003.

[109] O. Manzardo, R. Michaely, F. Schaedelin, W. Noell, T. Overstolz, N. deRooij, and H. P. Herzig. Miniature lamellar grating interferometer based on silicon technology. *Optics Letters*, 29(13):1437–1439, July 2004.

[110] M. Finot, M. McDonald, A. Daiber, W.B. Chapman, D. Li, M. Epitaux, E. Zbinden, J. Bennett, W.J. Kozlovsky, and J.-M. Verdiell. Automated optical packaging technology for 10gb/s transceivers and its application to a low-cost full c-band tunable transmitter. *Intel Technology Jounal*, 8:101–114, 2004.

[111] R. Billington. Effective area of optical fibres - definition and measurement techniques. Technical report, Centre for Optical and Environmental Metrology, 1999.

[112] Fujita and Toshiyoshi. *Handbook of Microlithography, Micromachining, and Microfabrication Volume 2: MICROMACHINING AND MICROFABRICATION*. SPIE.

[113] S. Sinzinger and J. Jahns. *Microoptics*. 1999.

[114] J.R. Wendt, T.W. Kygowski, G.A. Vawter, O. Blum, W.C. Sweatt, M.E. Warren, and D. Reyes. Fabrication of diffractive optical elements for an integrated compact optical microelectromechanical system laser scanner. *J. Vac. Sci. Technol. B*, 18(6):3608–3611, Nov/Dec 2000.

[115] C.-L. Dai, H.-L. Chen, C.-Y. Lee, and P.-Z. Chang. Fabrication of diffractive optical elements using the cmos process. *Journal of Micromechanics and Microengineering*, 12:21–25, 2002.

[116] Ph. Nussbaum and H.P. Herzig. Low numerical aperture refractive microlenses in fused silica. *Optical Engineering*, 40(7):1412–1414, July 2001.

[117] Optical properties of silicon. Internal report, Virginia Semiconductor, Inc., 1501 Powhatan Street, Fredericksburg, Va 22401, 2004.

[118] A. Schilling, R. Merz, C. Ossmann, and H.P. Herzig. Surface profiles of reflow microlenses under the influence of surface tension and gravity. *Optical Engineering*, 39(8):2171–2176, 2000.

[119] A. Jain and H. Xie. A tunable microlens scanner with large-vertical-displacement actuation. In *MEMS*, pages 92–95, Miami, January 2005. IEEE.

[120] M. Severi and P. Mottier. Etching selectivity control during resist pattern transfer into silica for the fabrication of microlenses with reduced spherical aberration. *Optical Engineering*, 38(1):146–150, 1999.

[121] D. A. Fletcher, K.B. Crozier, K. W. Guarini, S. C. Minne, G. S. Kino, C. F. Quate, and K. E. Goodson. Microfabricated silicon solid immersion lens. *Journal of Microelectromechanical Systems*, 10(3):450–459, 2001.

[122] R. Völkel, H.P. Herzig, P. Nussbaum, and R. Dändliker. Microlens array imaging system for photolithography. *Optical Engineering*, 35(11):3323–3330, November 1996.

[123] K.J. Garcia. Calculating component coupling coefficients. *Laser Focus World*, August 2000.

[124] R. Gale Wilson. Numerical aperture limits on efficient ball lens coupling of laser diodes to single-mode fibers with defocus to balance spherical aberration. Technical memorandum, NASA Langley Research Center, Hampton, VA, November 1994.

[125] H. Yang, C.-K. Chao, C.-P. Lin, and S.-C. Shen. Micro-ball lens array modeling and fabrication using thermal reflow in two polymer layers. *J. of Micromech. Microeng.*, 14:277–282, 2004.

[126] B.E.A. Saleh and M.C. Teich. *Fundamentals of Photonics*. Wiley Interscience, 1991.

[127] B.E.A. Saleh and M.C. Teich. *Fundamentals of Photonics*. In [126], 1991. page 282.

[128] P. C. Montgomery, D. Montaner, O. Manzardo, M. Flury, and H. P. Herzig. The metrology of a miniature ft spectrometer moems device using white light scanning interference microscopy. *Thin Solid Films*, 450:79–83, 2004.

[129] Paul Montgomery, Denis Montaner, O. Manzardo, and H.P. Herzig. Lateral error reduction in the 3d characterization of deep moems devices using white light interference microscopy. In *Symposium: "Optical Micro- and Nanometrology in Manufacturing Technology" (EPE109)*, 2004.

[130] N. Tas, T. Sonnenberg, H. Jansen, R. Lengtenberg, and M. Eswenspoek. Stiction en surface micromachining. *J. Micromech. Microeng.*, 6:385–397, 1996.

[131] N. Dechev. Lecture 21: Stiction in mems. Course, March 2006.

[132] T. Yu, R. Ranganathan, N. Johnson, N. Yadav, R. Gale, and T. Dallas. In situ characterization of induced stiction in a mems. *Journal of Microelectromechanical Systems*, 16(2):355–364, April 2007.

[133] J. M. Bustillo, R. T. Howe, and R. S. Muller. Surface micromachining for microelectromechanical systems. In IEEE, editor, *Proceedings of the IEEE*, volume 86, pages 1552–1574, August 1998.

[134] C. H. Mastrangelo. Adhesion-related failure mechanisms in micromechanical devices. *Tribology Letters*.

[135] R. S. Fearing. Survey of sticking effects for micro parts handling. Report.

[136] A. Plössl and G. Kräuter. Wafer direct bonding: tailoring adhesion between brittle materials. *Materials Science and Engineering*, R25:1–88, 1999.

[137] Y. Pétremand, P.-A. Clerc, M. Epitaux, A. Imhof, W. Noell, J.-M. Verdiell, and N.F. de Rooij. Novel 2d mems based optical beamsteerer. In IEEE/LEOS, editor, *Optical MEMS 2004*, pages 58–59, Takamatsu, Japan, 2004.

[138] M. Epitaux, Y. Pétremand, W. Noell, N. De Rooij, and J.-M. Verdiell. Silicon optical benches for next generation optical packaging: Going vertical or horizontal? In *IEEE 2005 Electronic Components and Technology Conference*, volume 2, pages 1339–1342. IEEE, 2005.

[139] W. Karthe and R. Müller. *INTEGRIERTE OPTIK*. 1991.

[140] Y. Pétremand. Mopos annual report 2005. Annual report, IMT, February 2005.

[141] J. Salmi and J. Salonen. Solder bump flip chip bonding for pixel detector hybridization. Workshop, CERN, Geneva, June 2003.

[142] T. Tschan. Deciding between flip chip and wire bonding. Technical report, ESEC, Switzerland, September 2002.

[143] W. Huang and G. Lu. Analysis of lateral instability of in-plane comb drive mems actuators based on a two-dimensional model. *Sensors and Actuators A*, A 113:78–85, 2004.

Acknowledgments

I would like to acknowledge everyone who helped me during the period of my PhD and all my studies.

The MOPOS Team

This project was not only mine but a collaboration with many people who helped me or gave me ideas or solutions for the different problems I encountered.

First, I would like to thank Prof. Nico de Rooij for giving me the opportunity to perform my PhD in the SAMLAB (Sensors, Actuators and Microsystems LABoratory) and Dr. Wilfried Noell, who guided me as the leader of the SAMLAB's Optical MEMS group. He learned me many things in various domains starting from well-structured presentations and reports to matlab programming or how to perform good simulations.

From the beginning of the project, we always had constructive discussions with the project leader at Intel: Marc Epitaux. Although he gave us a lot of work by adding new problems to the existing one by changing the configuration of the device or asking for new features to add to the MEMS, he did a very good job by creating the packaging system elaborated for the MOPOS module. On Intel side, I also would like to thank Marc Finot and Mark McDonald for valuable discussions and for helping me to perform optical measurements in California.

During the project, we also collaborate with other companies and other people. I will cite Ralf Hauffe from Hymite GmbH and Ken Weible, Martin Eisner and Reinhard Völkel from Süss Microoptics. On the academic side of the project, I would also like to thank Herbert Keppner and Francisco Dias for the laser micromachining tests and the different students who participated at different level to the project: Andreas Imhof, Andrei Dorogan, Ayhan Cati, Andrei Rukhlenko and David Schmied.

The SAMLAB Group

For sure, I would not have been able to perform this work without the support of the whole SAMLAB staff; Clairon and Rémy for DRIE, Gianni and Stéphane for oxidations, Sabina, Nicole and Giovanni for layer depositions, Eduardo for RIE, Edith for every small cleanroom problems, Sylviane for wire bonding, José for technical maintenance, Karine for administrative questions and Sylvain for the organization of the lab. As the SAMLAB life is not limited to the cleanroom, I will also thank all the other students, collaborators and researchers of the group: Alexandra, Quên, Milena, Mireille, Neetha, Sylvia and Laure in the feminine part and Peter, Michael, Roland, Urs, Patrick, Luca, Sebastian, Winston, Giovanni, Thomas, Nicolas, Severin, Olivier, Andreas, Laurent, Stephan, Yannick, Massoud, Daniel, Teru, Jérôme, Kaspar, Raphaël, Dara, Felix, Omar, Friedjof, Don, Danick, Gregor, Philippe and Vincent (I'll pay a beer to anyone I forgot...). At different level, I always had nice and interesting discussions on various subject starting from the weather, our respective projects or our taste about beer. Of course, I will not forget the guy who share my office, the guy we call when we have a computer problem (fortunately not often!), Claudio.

Everyone Else

Of course, work is not everything in life and I would not have been able to write this thesis without external activities. I would like to thank all my sports maids, people who accompanied me during one or several of my numerous sportive activities: Mathieu, Boris, Etienne, David, Jean-Marc, Sylvia and Denise (and more) for unforgettable bike, ski or snowboard rides, my comrades of the CEP for sharing many sportive activities as well as all the team maids of the numerous teams I took part during this period. I will not cite everyone, otherwise, I would also have to thank the tens of thousands of people who shared my life during races or large events... All these people and activities helped me to (trying to) keep a healthy mind in a healthy body!

I will also thank all my former teachers who learned me many interesting and boring things during my whole education. These years were really unforgettable.

Finally, last but not least, I would like to thank Christelle, who shared so many things with me during all my PhD studies (quite some time!) and my parents who always gave me the choice to do what I wanted in my life and supported me during my long learning period.

Acronyms

Abbreviation	**Signification**
CVD	Chemical Vapour Deposition
DRIE	Deep Reactive Ion Etching
EDX	Energy-Dispersive X-ray spectroscopy
FIB	Focus Ion Beam
GBIC	GigaBit Interface Converter
IMT	Institute of MicroTechnology
LOR	Lift-Off Resist
LPCVD	Low Pressure CVD
MEMS	Micro Electro Mechanical Systems
MOEMS	Micro Opto Electro Mechanical Systems
MOPOS	Micro Optical POsitioning System
PECVD	Plasma-Enhanced CVD
RIE	reactive Ion Etching
RF	Radio Frequency
SAMLAB	Sensors, Actuators and Microsystems LABoratory
SOI	Silicon On Insulator
SMF	Single Mode Fiber
TEM	Transmission Electron Microscope
TCVR	Transceiver
XAUI	X Attachment Unit Interface

Physical constants

Constant name	**Value**
Young's modulus of silicon	$E = 160\,\mathrm{GPa}$
Permittivity of free space	$\epsilon_0 = 8.854 \times 10^{-12}\,\mathrm{A \cdot s/V \cdot m}$
Density of silicon	$D_{\mathrm{Si}} = 2.33\,\mathrm{g/cm^3}$
Density of boron	$D_{\mathrm{Boron}} = 2.46\,\mathrm{g/cm^3}$
Atomic weight of boron	$M_{\mathrm{Boron}} = 10.811\,\mathrm{amu}$
Avogadro number	$N_{\mathrm{Avogadro}} = 6.022 \times 10^{23}\,\mathrm{mol^{-1}}$
Wavelength for optical telecommunications	$\lambda_{\mathrm{telecom}} = 1330$ to $1550\,\mathrm{nm}$

Publications

List of publications and conferences

Related to this thesis

Y. Pétremand, P.-A. Clerc, M. Epitaux, A. Imhof, W. Noell, J.-M. Verdiell and N.F. de Rooij. *Novel 2D MEMS Based Optical Beamsteerer.* 2004 IEEE/LEOS International Conference on Optical MEMS, pages 58-59, Takamatsu, Japan, 2004.

Y. Pétremand, P.-A. Clerc, W. Noell, M. Epitaux, J.-M. Verdiell and N.F. de Rooij. *Novel 2D MEMS Based Optical Beamsteerer.* MicroNanoFabrication Annual Review Meeting 2005, Ecole Polytechnique Fédérale de Lausanne, Lausanne, May 2005.

Y. Pétremand, W. Noell, M. Epitaux, J.-M. Verdiell and N.F. de Rooij. *Post Assembly Alignment System.* In 10th International Comercialization of Micro and Nano Systems Conference, pages 477-481. MANCEF COMS, August 2005.

M. Epitaux, Y. Pétremand, W. Noell, N. de Rooij and J.-M. Verdiell. *Micro-machined XY stage for fiber optics module alignment.* In Optical Fiber Commmunications Conference Technical Digest 2005, volume 4. IEEE, 2005.

M. Epitaux, Y. Pétremand, W. Noell, N. de Rooij and J.-M. Verdiell. *Silicon optical benches for next generation optical packaging: Going vertical or horizontal?* In IEEE 2005 Electronic Components and Technology Conference, volume 2, pages 1339-1342. IEEE 2005.

Y. Pétremand, P.-A. Clerc, M. Epitaux, R. Hauffe, W. Noell and N.F. de Rooij. *Optical beam steering using a 2D MEMS scanner.* In Proceedings of ISOT07, Lausanne, September 2007.

Y. Pétremand, M. Epitaux, R. Hauffe, W. Noell, N. F. de Rooij. *Beam steering system using a 2D MEMS scanner.* In Proceedings of IEEE-LEOS 07, Orlando, Florida, September 2007.

M. Eptiaux, W. Noell, Y. Pétremand, N. F. de Rooij. *Movable lens beam steerer.* US Patent Nr. US2007297041, December 27 2007.

M. Eptiaux, W. Noell, Y. Pétremand, N. F. de Rooij. *Electromechanical drives adapted to provide two degrees of mobility.* Patent Nr. WO2005109621, November 11 2005.

Others

O. Manzardo, Y. Petremand, H.P. Herzig, W. Noell and N.F. de Rooij. *Micro-fabricated system for wavelengths monitoring.* 2002 IEEE/LEOS International Conference on Optical MEMS (Cat. No.02EX610) 23-4 2002

O. Manzardo, Y. Petremand, H.-P. Herzig, W. Noell, N.F. de Rooij. *Micro-fabricated spectral analysers.* Proceedings Vol. 4829, 19th Congress of the International Commission for Optics: Optics for the Quality of Life, Giancarlo C. Righini; Anna Consortini, Editors, pp.841-843, November 2003

Y. Pétremand, W. Noell and N.F. de Rooij. *Microfabricated 2D scanner based on linear actuation.* MicroNanoFabrication Annual Review Meeting 2006, Ecole Polytechnique Fédérale de Lausanne, Lausanne, May 2006.

C. Ataman, Y. Petremand, W. Noell, H. Ürey, M. Epitaux, N.F. de Rooij. *A 2D MEMS stage for optical applications.* Proceedings Vol. 6186, MEMS, MOEMS, and Micromachining II, Hakan Ürey; Ayman El-Fatatry, Editors, 618603, April 2006

Y. Pétremand, C. Ataman, W. Noell, N. de Rooij, H. Urey. *NEMO 2D Platform*. General Scientific Network of Excellence in MicroOptics meeting 2006, Karlsruhe

Y. Pétremand, N. Golay, W. Noell and N.F. de Rooij. *Dynamic MEMS measurement using a WYKO interferometer*. MicroNanoFabrication Annual Review Meeting 2007, Ecole Polytechnique Fédérale de Lausanne, Lausanne, May 2007.